Dissertation

Q-factor manipulation of AFM cantilevers with integrated piezoelectric transducers for operation under vacuum

zur Erlangung des akademischen Grades

des Doktors der technischen Wissenschaften (Dr.techn.)

der Fakultät für Elektrotechnik und Informationstechnik

am Institut für Sensor- und Aktuatorsysteme E366

der Technischen Universität Wien

Dipl.-Ing. Martin Fischeneder

Matrikelnummer: 0127178

Wien, 2023

Verteidigung: Wien, 16.06.2023

Vorsitz: Assoc.Prof.Dr. Wolfgang Kemmetmüller

                       Technische Universität Wien, Österreich

Betreuer: Univ.-Prof. Dr.rer.nat. Ulrich Schmid

                       Technische Universität Wien, Österreich

Gutachter: Univ.-Prof. Mag.rer.nat. Dr.rer.nat. Alexander Bergmann

                       Technische Universität Graz, Österreich

                       Univ.-Prof. Dr.sc. Silvan Schmid

                       Technische Universität Wien, Österreich

Acknowledgments

I would like to express my deepest appreciation to my doctoral supervisior Prof. Ulrich Schmid for his tireless support and for the opportunity to work in his research group at the Institute of Sensors and Actuator Systems at the Vienna University of Technology. I'm extremely grateful to the postdoctoral researchers Michael Schneider and Achim Bittner, for their support and for sharing their expertise.

I am also grateful for the support from my students Martin Oposich, Daniel Duller, David Bugl, David Graf, Krisztian Dubek and Markus Kratochwill. Further, I would like to thank my colleges Elisabeth Wistrela, Markus Leitgeb, Georg Pfusterschmid and Manuel Gillinger for their professional and private support during my work at the institute. I am thankful to Sophia Ewert, Franz Prewein, Martina Nuhsbaumer, Patrick Meyer, Michael Buchholz and Andreas Astleitner for their technical, administrative and moral support.

Additionally, I would like to acknowledge the financial support from the ZIT Vienna "Call from Science to Products 2013" ID.: 1044801.

I am also thankful for my parents Anton and Aloisia whose constant love and support keep me motivated.

Furthermore, this endeavour would not have been possible without the support from my wife Katharina and my children Benedikt and Jakob. Many thanks for keeping me on track.

Abstract

Scientific studies of physical objects can be done by analysing the surface properties of the underlying objects with the atomic force microscopy (AFM) and the scanning electrode microscopy (SEM). The oscillating MEMS (micro electromechanical systems) AFM cantilever scans the sample surface to acquire the surface related properties *i.e.* micro-structure, roughness, magnetic fields and surface potential. The aperture delivers fantastic images on flat surfaces, but on rough surfaces the depth of field is quite low. On the other hand, the SEM guides an electron beam to the sample surface and the reflected electrodes are detected to acquire the surface information. The SEM excels the AFM in the quality of high depth of field images.

To enhance the performance of microscopy systems, the integration of AFM cantilevers into a SEM vacuum environment is a promising approach. To enable high speed measurements with highest lateral resolution, a tuneable Q-factor may be a key feature. Therefore, a piezoelectric aluminium nitride (AlN) layer placed on the cantilever manipulates the resonantly operated AFM cantilever.

To avoid any static torsion or deflection, the AFM cantilever has to be straight. To achieve this, the film stress of the AlN thin film has to be controlled during the fabrication of a cantilever, where a reactive sputter process through aluminium and nitrogen deposits the layer. The deposition process heats up the substrate and therefore the wafer bow causes variations of the thermal connection between wafer and sample holder. This goes along with undefined film stress of the AlN layer. In order to minimize the derivation of film stress, the reduction of substrate temperature and the enhancement of thermal connection between substrate and substrate holder is targeted. Therefore, a novel clamped substrate holder is designed which offers a great heat flow from the substrate to the ambient equipment and provides an equal heat distribution. Through clamping of the wafer during the fabrication process, any movement of the waver is prohibited. A long-term study was made to verify the improvement of the clamped sample holder. Therefore, AlN layers with thicknesses of 0.5 µm, 1.0 µm and 2.0 µm were deposited on silicon wafers. Through clamping the wafer, the deposition temperature at 0.5 µm thickness is lower than 100 °C. The measurement of the deposited films yields to a compressive layer stress and a reduction of scattering compared to a standard wafer holder. The piezoelectric coefficient has an average value of -7 pC/N. The leakage current characteristic was specified as Pool-Frenkel.

To achieve the aim of Q-factor manipulation, the oscillation introduced by a macroscopic piezoelectric actuator, the tapping piezo, is manipulated by an additional mechanical stimulus through the AlN thin film. The phase shifted electrical stimulus of the thin film, which is electrically integrated in a Wheatstone bridge configuration, allows an electrically determined and optically verified Q-factor reduction of 1.9 in vacuum.

Quite contrary to the latter solution, the replacement of the tapping piezo through an active actuated cantilever is introduced. The piezoelectric layer is stimulated with an adjustable proportional feedback which manipulates the oscillation amplitude of the cantilever. The feedback itself is calculated from the compensated current through the piezoelectric layer. At ambient pressure, a reduction of the Q-factor of a factor 1.6 is possible. At vacuum, in fact it was designed for this purpose, the reduction of a factor 3.55 is achieved. A realistic assessment with a simulated microstructure reaches a reduction of the response time by a factor of 3.8, which is close to the response time, which was measured in ambient pressure.

These findings clearly demonstrate the potential of the active Q-factor manipulation by super-positioning or by excitation manipulation by an active feedback circuit. Beside the adjustability of the Q-factor in vacuum and the possibility of miniaturisation (integration of sensor chip into the cantilever), it is possible to integrate a high-speed sensor unit into a SEM, which widens the options for surface analysis methods.

Kurzfassung

Wissenschaftliche Untersuchungen von Objektoberflächen werden mit Hilfe von Rasterkraftmikroskopie (AFM) sowie von Elektronenstrahlmikroskopie (SEM) durchgeführt. Das AFM tastet die Oberfläche mit einem oszillierenden MEMS (micro electromechanical systems) Cantilever ab. Es kann zum Beispiel die Makrostruktur, die Oberflächenrauigkeit, das magnetische Feld und das elektrische Potential erfasst werden. Das Mikroskop liefert sehr gute Bilder bei flachen Oberflächen, aber bei rauen Oberflächen ist die Tiefenschärfe sehr niedrig. Im Gegensatz dazu wird bei einem SEM ein Elektronenstrahl auf die Oberfläche gelenkt und durch die reflektierten Elektronen kann die Oberflächeninformation erfasst werden. Das aufgenommene SEM Bild besitzt eine deutlich höhere Tiefenschärfe als die Bilder vom AFM.

Zur Verbesserung der Leistungsfähigkeit beider Mikroskopsysteme, wird ein AFM Cantilever in die Vakuumkammer des SEM verbaut. Eine schnellere Messung mit hoher lateraler Auflösung kann durch die Anpassung des Q-Faktors an die Oberfläche erreicht werden. Um die Schwingungen des Cantilevers verändern zu können, wird eine Aluminiumnitritschicht (AlN) auf den Cantilever aufgebracht.

Damit sich der Cantilever durch diese Schicht nicht verdreht oder durchbiegt, muss der Filmstress bei dem reaktiven Abscheideprozess von Aluminium und Nitrit zu Aluminiumnitrit kontrolliert werden. Dieser Abscheideprozess heizt das Substrat auf und verursacht eine Verbiegung des Wafers aufgrund undefinierter Wärmeanbindung an das Gehäuse. Zur Verringerung der Abscheidetemperatur und der Schwankungen des Filmstresses, wurde ein neuer Probenhalter entworfen, der den Wärmetransport verbessert und eine gleichmäßigere Wärmeverteilung erzielt. Durch die Klemmung des Wafers während des Abscheideprozesses werden eine Wölbung sowie jegliche laterale Bewegung des Wafers verhindert. Eine Langzeitstudie mit 0,5 µm, 1,0 µm und 2,0 µm AlN Schichtendicken zeigt, dass alle abgeschiedenen AlN Schichten einen negativen Schichtstress und eine Verringerung der Schwankung des Schichtstresses im Vergleich zum Standardwaferhalter aufweisen. Bei der Schichtdicke von 0,5 µm bleibt die Abscheidetemperatur unter 100 °C. Die abgeschiedenen Schichten haben eine durchschnittliche piezoelektrische Konstante von -7 pC/N. Die elektrische Strommessungen an den AlN Schichten zeigen ein Pool-Frenkel Verhalten.

Die Manipulation des Q-Faktors wird durch Überlagerung von zwei Schwingungen erreicht. Der Cantilever wird von einem makroskopischen Tapping Piezo angeregt und durch eine mikroskopische Schwingung von der piezoelektrischen Schicht am Cantilever überlagert. Die Schicht ist elektrisch in eine Wheatstone Brücke eingebunden und wird durch ein frequenzabhängiges und phasenverschobenes Signal angeregt. Diese Manipulation reduziert den elektrisch und optisch gemessenen Q-Faktor in Vakuum um den Faktor 1,9.

Im Gegensatz zur Überlagerung von Schwingungen, kann durch Wegfall des Tapping Piezos, die Manipulation der Anregung den Q-Faktor reduziert werden. Die piezoelektrische Schicht erzeugt die Schwingung am Cantilever die durch eine anpassbare, proportionale Rückkopplung gesteuert werden kann. Die Rückkopplung wird aus dem kompensierten Strom, der durch die piezoelektrische Schicht fließt, erzeugt. In Luft wird der Q-Faktor um einen Faktor 1,6 verringert und in Vakuum wird eine Reduktion des Q-Faktors um einen Faktor von 3,55 erreicht. Die Reduktion des Q-Faktors bewirkt eine Reduktion der Antwortzeit auf einen Höhensprung um einen Faktor von 3,8.

Diese Ergebnisse zeigen das große Potential der aktiven Q-Faktormanipulation. Neben der Anpassung des Q-Faktors liefern diese Ansätze die Möglichkeit für die Verkleinerung der Apparatur in der Vakuumkammer. Durch die Integration der Erfassung der Schwingung ist es möglich, ein Hochgeschwindigkeitsmesssystem in das SEM zu integrieren und so weitere Möglichkeiten für die Oberflächenanalyse zu schaffen.

Table of content

1 Introduction and motivation

Scientists always try to push knowledge beyond the obvious and try to find explanations for complex relations. If an object is touched with our hands, the bulk properties like temperature, weight and strength are experienced. By getting in contact with the surface with our fingers, a sudden haptic feedback is given. Due to the macroscopic dimensions of our fingers, the impressions of the surface are only macroscopic. For a deeper understanding of surfaces and for a further optimization of surfaces for different applications, the micro- and nanoscale surface properties are crucial. Such interfaces play a major role in high-technology applications like in plastic-, pharma-, coating-, chemistry- and semiconductors industry, just to name a few. To capture these interfaces, one needs a capable microscope technology.

When one looks at a surface with his eyes, which corresponds to a magnification of 1, structures down to a sub-millimetre range are recognizable. Magnifying glasses can improve the resolution and improve the magnification to approximately 5 – 10 [1]. In the seventeenth century, a combined lens apparatus called microscope was able to reach a magnification of several hundred times [2]. Thereby bacteria and cells at the micron-scale can be observed. The development continued in the eighteenth century. At the end of the nineteenth century, the optical microscopes reached sub-micrometre resolution by adding more lenses. Nowadays, optical methods record images with reflected or transmitted light and with digital sensors for image processing. Image processing makes an automatic evaluation of microstructures with geometrical evaluation or particle and phase analysis simpler and quicker.

A game changer entered the scene at the end of the nineteenth and the beginning of the twentieth century. The discovery of the electron by Thomson, the introduction of special relativity theory by Einstein as well as quantum mechanics paved the way for a new measurement technique. Thanks to Plank, Bohr, de Broglie, Heisenberg, Schrödinger and Dirac, quantum mechanics have been further developed. Through the description of wave-particle dualism, Ernst Ruska was able to present the first electron microscope in 1931. It had a disappointing 17 times magnification [3], yet only two years later, in 1933, Ruska was able to reach a resolution of 50 nm which corresponds to a magnification of 12 000 [4]. Despite this achievement, scientific interest declined strongly because the electron beam burned each sample to cinder [2].

At the same time, Marton [5] succeeded in avoiding burning the samples, which resulted in the first commercial instrument by Siemens and Halske in 1939. After the Second World War, electron microscopy developed very quickly through its use in biology, chemistry, physics and material science.

The resolution constantly improved from remarkable 1 nm for a transmission electron microscope (TEM) in 1956 [6] to 0.1 nm in the 1990s. On the contrary, the presence of spherical and chromatic aberration (*i.e.* electromagnetic radiation of different energies converge at different focal planes) limited further improvement in lateral resolution [2]. At the end of the 1990s, the blurring of the images caused by lens aberrations of an electron microscopy counteracted with spherical aberration correction and proper alignment, so that a resolution of sub 0.1 nm was feasible. In addition, the signal-to-noise ratio was improved [7], which is now retrieved in state of the art electron microscopes.

Back in the 1950s, a new microscope family was introduced, which has two operational elements - a sharp tip and a feedback loop - in common. For these microscopes, the sharp tip is mandatory to guarantee a high lateral resolution. The feedback loop is keeping the interaction between sample and tip constant for a highly accurate measurement in the z-direction. In the 1980s, the scanning tunnelling microscope (STM) was invented, where the tunnelling current between the metallic tip and the sample is kept constant by adjusting the vertical position of the tip in a closed-loop configuration and thus keeping the distance constant. Until the invention of the atomic force microscopy (AFM) in 1986, which

enables even the characterization of electrically non-conductive samples, it was only possible to measure electro-conductive samples [8]. The first AFM used the contact mode, which holds the static deflection of the tip constant, while the z-stage is changed depending on sample topography. A year later, the tapping mode for the AFM was introduced by Martin *et al.* [9]. The oscillation amplitude and frequency of the AFM cantilever is kept constant, while the height of the cantilever above the sample is controlled. The equipment uses two feedback loops: the fast feedback, which characterizes the material properties by logging the pulling force of the tip and the slow feedback loop, which monitors the surface topography by keeping the sample-probe spacing constant [9]. To record the oscillation amplitude, a helium-neon (HeNe, 632nm, visible red) laser beam was focused towards the cantilever and the reflected beam was brought to interference with the original beam. Doing so, the corresponding interference patterns allow to measure any force acting on the cantilever with highest accuracy. Due to the flexibility of the method, magnetic properties, electrostatic charges and surface potential differences could also be recorded. At that time, however, only a few research groups could handle the complexity of the setup and that is why only a few scientific works were published exploiting this measurement technique [10].

The mid-1990s recorded a rapid growth of applications. The possibility of using commercially available, reliable AFMs with a modulated frequency laser [11], low noise position detector and a micro-fabricated cantilever enabled the exploration of DNAs [12], proteins [13] and polymer surfaces [14, 15] with nanoscale resolution, just to mention some typical applications. The implementation of phase-shift imaging while the topology is recorded offers a significant improvement in resolution for compositional variations with no reduction in scanning speed or resolution [16]. Through the reduction of the geometrical length of the cantilever, a reduction in thermal noise and an increase in scan speed are achieved [17]. Additionally, amplitude modulation of AFM probes opens up new application possibilities like nanopatterning and nanolithography [18-20].

In the 2000s, the development of AFMs is inhibited by the lack of theory in amplitude reduction, higher harmonics and the reconstruction of force from the subject. At this time, a large number of publications addressed these topics, like Garcia *et al.* [21], Rodriguez *et al.* [22] and Stark *et al.* [23]. Moreover, further instrumental development results in an AFM with a 12.5 Hz frame rate for biological samples [24] and a multi-frequency approach to enhance spatial resolution [25].

Since then, the focus of experiments lays on the simultaneous detection of multi-harmonics of the tip oscillation. For example, bimodal approaches have been used to image isolated antibodies in air and in liquids [26]. Another approach utilizes torsional harmonics in the cantilever in combination with an off-centred tip, which allows time-resolved tapping-force curves [27, 28]. Current efforts in improving the overall AFM performance can be divided into two sub-areas. First, the dynamics of the cantilever in liquids, the asymmetry of the oscillation, the damping and added mass effect are addressed [29]. Second, the stimulation in various multi-frequency regimes is studied [30].

Beside the rapid development, state of the art AFMs are still limited to local scan areas with a single scan image area of several 100 μm^2. Through a slow measurement speed compared to SEM, overview measurements larger than 100 μm^2 are unfeasible in a reasonable time. An AFM delivers a three-dimensional sample image, which depends on the type of cantilever and its tip geometry. When using specific cantilevers, an AFM can measure surface properties, such as magnetic fields (MFM), surface potential (SKPM), surface temperature (SThM), friction (SFM) and many other surface physical properties on the nanoscale [2].

In contrast, a SEM can image a sample area in the range of square millimetres with tremendous depth of field images, but unlike to an AFM, only with a two-dimensional projection. The large scanning area of a SEM can help to find the area of interest for a detail analysis with an AFM [31]. For SEM the samples must be conductive. A distinction between the materials itself is only possible through the material

contrast of the backscatter electrodes signal. Combining the SEM and AFM into one equipment could be beneficial for the improvement of measurement location accuracy but also shortens the scanning time and provides measurement automation.

When operating an AFM cantilever in vacuum, the fluidic damping of the atmosphere can be neglected [32] and as a result, the Q-factor of the cantilever and hence the corresponding time constant [33] to adapt the oscillation behaviour after an external stimulus increase [32]. As a consequence, the response time of the oscillation amplitude to surface steps is longer, thus prolonging the measurement time [34, 35]. The Q-factor and resonance frequency are specified by the geometric dimensions and the material of the cantilever [36]. By changing the cantilever material or dimension, the Q-factor can be reduced, but cannot be adapted during AFM measurements to specific requirements.

To overcome this drawback, the realization of an electronically adjustable Q-factor is targeted to improve the performance of resonantly operated AFM cantilevers. Through the adjustability, the Q-factor can be adapted during the measurement. A common method for active modification of the Q-factor is the implementation of a feedback on the tapping piezo, based on the optical beam deflection [37]. The imaging dynamics are improved by adjusting the Q-factor during the scan through an enhanced Q-factor during the attractive regime and a decreased Q-factor during the repulsive regime of the cantilever tip [38]. The optical beam set-up of an AFM needs manual intervention because the beam has to be adjusted after every exchange of the cantilever. By removing the optical sensor in the feedback loop, the cantilever deflection measurement is replaced by a cantilever tip velocity measurement. The size of the equipment is reduced by removing the optical path and therefore the manual intervention is no longer necessary. When implementing this approach, the charge of the piezoelectric layer is measured and a positive position feedback (PPF) controller with active shunt control is placed in the feedback loop. Doing so, a reduction of the Q-factor caused by the high frequency noise of the differentiation of the displacement signal is avoided [39]. The use of the electrical cantilever velocity signal for a feedback loop necessitates the compensation of parasitic effects and the cancelation of the actuation signal, as reported in [40]. The use of an actively actuated piezoelectric layer allows to excite and simultaneously to monitor the cantilever oscillation [41]. A frequency-dependent change of the excitation voltage lowers the Q-factor [42] by decreasing the excitation voltage at the resonance frequency [43, 44].

An AFM is based on a micromachined cantilever, which represents a success story within the MEMS (micro electro-mechanical systems) field. In the last decades, a huge number of silicon-based MEMS sensors and actuators were developed and commercialized. This success is based on the broad range of different application scenarios, where MEMS devices can be most beneficially used, like the detection of chemical [36, 45, 46] or physical quantities [47-50]. Typical examples of these applications are gyroscopes, MEMS microphones, mass- or viscosity sensors with cantilevers [51-54], SAW (surface acoustic wave) [55] or BAW (bulk acoustic wave) [56], just to highlight a few selected examples.

Despite their individual and application-specific design, a significant part of approaches make use of either membranes or cantilevers as functional building blocks by applying electro-magnetic, electro-thermal [57, 58], capacitive or piezoelectric elements for excitation [59].

When integrating piezoelectric transducers [60], a typical design consists of an aluminium nitride layer (AlN) which is deposited on silicon (Si). In a next step, the latter support layer plus the piezoelectric element are released from the substrate [61, 62]. Despite the moderate piezoelectric coefficient [63, 64] AlN is often preferred over zinc oxide (ZnO) or lead zirconate titanate (PZT) as functional material because it is compatible with standard complementary metal-oxide-semiconductor (CMOS) microfabrication processes [65] and it offers a high temperature stability [56, 66]. Most promising application scenarios for cantilever or membrane-type micro-machined AlN devices are for example

density and viscosity sensors of liquids [43, 67, 68], high frequency filters [69, 70], MEMS scanning mirrors [71], microphone [72] or vibrational energy harvesters [73, 74].

After having introduced the operation principles and the most important advantages of SEM and AFM, it would be highly desirable to combine all these benefits in one system. Companies like Hitachi offer tools (Correlative AFM and SEM Imaging) for correlated measurements with both techniques. Their approach uses an accurate sample holder, which can be shared between the SEM and AFM. This concept avoids the operation of the AFM in ultra-high vacuum, which slows down the scanning speed of the AFM drastically. But, two individual rather expensive pieces of equipment must be acquired to harvest the data from the sample. An obvious solution would be to install a modified AFM scanner in the vacuum chamber of an SEM. For this purpose, the scanner must be adapted to compensate the lack of ambient air damping with an alternative damping method. The installation requires the replacement of the optical readout of the AFM cantilever deflection with an approach that is more compact and does not require manual user interaction. This can be attained by integrating a sensing layer on the cantilever, which is demonstrated by Adams *et al.* [75]. Compared to the optical read-out enabling a lateral measurement accuracy of 0.6 Å, an increased sensitivity of 0.3 Å is reported. The scanning speed can be increased with smaller cantilevers, which provides a higher resonance frequency with similar Q-factors and an additional external tapping amplifier. Adams *et al.* [76] demonstrate a five times larger closed-loop bandwidth with optical readout and with minor manipulations on an commercial AFM equipment.

A promising approach was shown by Mahdavi *et al.* [77, 78], where cantilevers with a two layer stack of AlN are reported. One transducer element is for stimulating the cantilever oscillation and the other is for measuring the oscillation amplitude. Such applications suffer from thermally or frequency induced leakage currents through the piezoelectric layer. It is highly recommended to compensate the temperature effects of the piezoelectric layer. One approach is to place a second, identical non-released transducer element on the same chip, thus balancing such parasitic effects with an electric circuit. A second approach of compensation uses two identical sensor areas placed on the cantilever. Both are moving, but through an electrical amplification circuit, the measurement signal is extracted [40, 79]. A different approach of an electrical readout is demonstrated by Rupert *et al.* [80, 81], where the oscillation is recorded via a bridge configuration and operational amplifier circuit. Even more, Lau *et al.* [82] verified a proposed multimodal control schema, with separately modulated, low band-width baseband controller and demodulated path for each mode. A similar PPF approach is shown from Karvinen *et al.* [83].

Based on the state of the art given in the literature, the following research question can be formulated: Is it possible to affect the oscillation amplitude, through a frequency dependent actuation of an additional piezoelectric layer which is integrated on a MEMS cantilever, to manipulate the Q-factor electronically? Is this approach also possible under vacuum condition, to achieve competitive measurement speeds like in air?

The Q-factor manipulation of a MEMS cantilever is subjected to physical limitations and constraints. For the analytic calculation and simulation of the oscillation of the cantilever the length to thickness ratio has to be maintained. To comply with the linear material parameters and mathematical models, high stress concentrations on the fixed support like an excessive deflection of the cantilever has to be avoided. The functional layers of the cantilever have to be fabricated with minimum layer thicknesses and the lateral clearances between the layers have to be maintained to avoid short circuits between the layers. In order to integrate the component into an electronic control system, electrical limits like maximal driving current, charge/discharge currents, supply cable length and the sampling frequency and bandwidth must be fulfilled.

Keeping the limitations in mind, the objective of this thesis is to evaluate the potential of active Q-factor tuning with piezoelectric transducers integrated on a MEMS cantilever. Therefore, the focus is on two possible approaches.

First, a superposition approach in chapter 6.1 (Measurement system: Frequency generator (FGEN) and oscilloscope (DSO)) is evaluated. In contrast to other technically demanding techniques, the implementation uses standard lab-equipment, like a frequency generator and an oscilloscope. Thus, the straightforward transfer to a microprocessor-controlled unit is feasible. It could be realized with a low-cost electronic circuit which can be placed close to the cantilever and which is optimized for minimum signal losses. Two sources of vibration are used to achieve the superposition effect on the oscillation amplitude. The macroscopic tapping piezo stimulates the entire cantilever. The microscopic piezoelectric thin film actuator is stimulated with a frequency-dependent, variable phase shift stimulation, thus should manipulate the oscillation amplitude of the cantilever.

Second, a closed-loop feedback circuit manipulates the Q-factor, where a lock-in amplifier adjusts the excitation signal of the cantilever. Therefore, a signal processing circuit in chapter 6.3 (Measurement System: Mixer and Lock-In) is designed, assembled and placed into a vacuum chamber. The cantilever oscillation is observed by the electrical signal from the piezoelectric layer and by the laser Doppler vibrometer (LDV) via an optical access to the vacuum chamber. By adjusting the active feedback levels, the Q-factors are determined through matching the theoretical models of the series resonant circuit and the Lorentz curve with the recorded frequency spectra. Additionally, the impact of the feedback loop on the response time of the step response approach is investigated.

The cantilever and the sample surface interact at the free end of the cantilever where the tip is placed. The oscillation parameters of the cantilever are affected by the surface forces (i.e. frequency, amplitude and phase) during the measurement procedure. Notwithstanding the scientific survey of surface interaction being an exciting scientific challenge, it is not the focus of this thesis.

For this investigation, a new fabrication process is developed. Based on existing process flows, a process with a lower temperature than 140 °C for AlN deposition has been found. Future applications show the importance of this investigation where cantilevers with beam thickness of only a few 100 nm are considered. If those cantilevers are equipped with a piezoelectric layer, the measurement accuracy is affected by the additional layer compared to the original device [84-86].

The magnetron sputtering process of the AlN layer has to be addressed, because it heats up at the sample through the particle bombardment [87]. The generated heat leads to a bending of the wafer due to the difference in thermal expansion (CTE) of substrate and deposited thin film. During the deposition process this results in a continuously changing thermal connection between the unclamped wafer and the substrate holder. This effect leads to an undefined substrate temperature and hence to a high variation of the biaxial film stress. As shown in chapter 4.2 (Clamped substrate holder), sputter deposited AlN thin films have a strong dependence on substrate temperature which has a high impact on the electro-mechanical parameters like piezoelectric coefficient d_{33} and leakage current characteristics discussed in chapter 4.3 (Characterisation of the AlN layers).

In this thesis, the influences of defined temperature conditions on the mechanical properties, on the wet etching capability and on the electro-mechanical properties of low temperature deposited AlN layers are investigated.

This should simplify the fabrication process, reduce the process duration and increase the yield of fabricated cantilevers. By simplifying the manufacturing process, more effort can be allocated towards future development of the control system. The results of the proposed solutions will significantly contribute to the improvement of AFM systems in vacuum through adaptive adjustment of the Q-factor. By using the cantilever as actuator and sensor at the same time, the size of the scanner can be

reduced dramatically, because the optical detector is no longer required. This opens a large flexibility of the application, even in vacuum. The flexibility can be used to integrate a microcontroller to manipulate the Q-factor, or alternatively, the microcontroller could be directly embedded into the silicon of the cantilever.

Further development of the cantilever can make an important contribution for the combination of AFM and SEM. It can help to use well-established techniques for advanced future analyses for complex surfaces, which enables an extensive characterization of surfaces by measuring a large variety of topography and material-related parameters.

2 Methods and instrumentation

For a better understanding, a compact historical review on piezoelectricity and its fundamental physics as well as a short overview on standard piezoelectric materials, its key properties and main application fields are given. Next, the focus shifts to the sputter deposition process of AlN and its fabrication, as this study specifically selects AlN as the preferred functional layer material in MEMS devices. Finally, the standard equipment which is needed for thin film characterization and MEMS device fabrication is discussed.

2.1 Piezoelectricity

Beginning with a historical overview of its discovery and subsequent investigations into its electromechanical performance, a comparison is made among typical piezoelectric materials. Ultimately, the material of choice for the MEMS cantilever application is selected.

2.1.1 Historical outline and the electromechanical phenomena

In the mid-18th century, Carl Linnaeus and Franz Aepinus made the first fundamental studies on the occurrence of electric fields at Tourmaline crystals when exposed to temperature changes. It took some time before Antoine César Becquerel made the first measurements of the pyroelectric behaviour in 1828. In 1878 William Thomson published the first theory on pyroelectricity.

Later on, in 1880, with the knowledge of pyroelectricity and the associated requirements for the crystal structures, the brothers Pierre and Jacques Curie succeeded in describing the piezoelectric effect of a Tourmaline crystal. By applying force to the crystal, an electrical charge appears on the quartz surface, which also occurs at topaz, cane sugar and Rochelle salt (sodium potassium L(+)-tartrate tetrahydrate, $KNaC_4H_4O_6 \cdot 4H_2O$)

One year later, in 1881, Gabriel Lippmann mathematically deduced the reciprocal piezoelectric effect from the fundamental principles of thermodynamics and the Curie brothers confirmed his calculation. Around 1890, Gregorio Ricci-Curbastro developed the description of the anisotropic properties of the crystals by applying tensor calculations. In 1898, Woldemar Voigt introduced the current meaning of a tensor and in 1910 the Teubner Verlag published this work in "Lehrbuch der Kristallographie". The first application of piezoelectricity, the "Curie's electrometer", was used by Maria Sklodowska-Curie to study radioactivity. Further on, in 1920, Joseph Valasek [88] introduced the ferroelectricity of Rochelle Salt ($KNaC_4H_4O_6 \cdot 4H_2O$), which has an electrical charge hysteresis on electrical field change.

Based on these findings, the electromechanical phenomena can be categorized into three different material types: piezo-, pyro- and ferroelectric materials. By applying mechanical stress, an electrical charge occurs within certain solid materials. This main group is called piezoelectric materials, where silicon dioxide (SiO_2), gallium phosphate ($GaPO_4$), aluminium phosphate ($AlPO_4$) and AlN are well-known representatives, as illustrated in Fig. 2.1 (a) [89]. A subgroup of piezoelectric materials is also pyroelectric, like lithium borate ($Li_2B_4O_7$). These materials respond with the generation of electric charges when facing temperature changes. Barium titanate ($BaTiO_3$), lead titanate ($PbTiO_3$) and lead zirconate titanate (PZT, $Pb[Zr_xTi_{1-x}]O_3$ ($0 \leq x \leq 1$)) are typical ferroelectric materials and belong to a subgroup of pyroelectric materials, which have a polarisation hysteresis in response to an electrical field change.
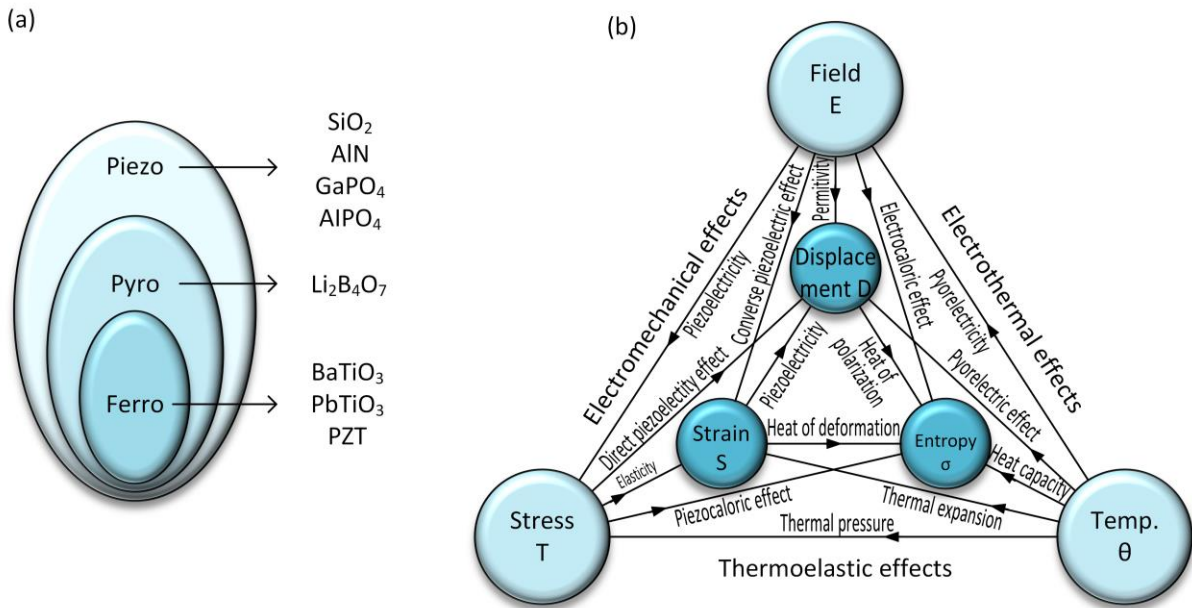
Fig. 2.1: (a) The hierarchy of electromechanical phenomena [90, 91] in materials and (b) the Heckmanns diagram of coupled field phenomena.

The Heckmann diagram, given in Fig. 2.1 (b), shows the correlation between electrical, mechanical and thermal phenomena [89, 92-94]. If the electromechanical effect is considered in detail, it describes a direct conversion from mechanical to electrical energy and *vice versa*. This relation can be divided into linear effects, like piezo- and pyroelectricity, and nonlinear effects, like ferroelectricity and electrostriction.

In general, 21 out of 32 known crystallographic classes feature a polar axis, which is required for electromechanical coupling. 20 of them feature the piezoelectric effect. The local charge distribution in a piezoelectric crystal without an applied external force [95] is schematically shown in Fig. 2.2 (a). If an external force is applied on the surface of the crystal and the crystal is *e.g.* compressed, the original charge distribution is dislocated and as a direct consequence, surface charges are generated on the crystal surface, which appear as a voltage as shown in Fig. 2.2 (b). When an external voltage is applied, the so-called reciprocal piezoelectric effect leads to a locally changed charge distribution and this results in a crystal deformation or crystal expansion, which is shown in Fig. 2.2 (c).
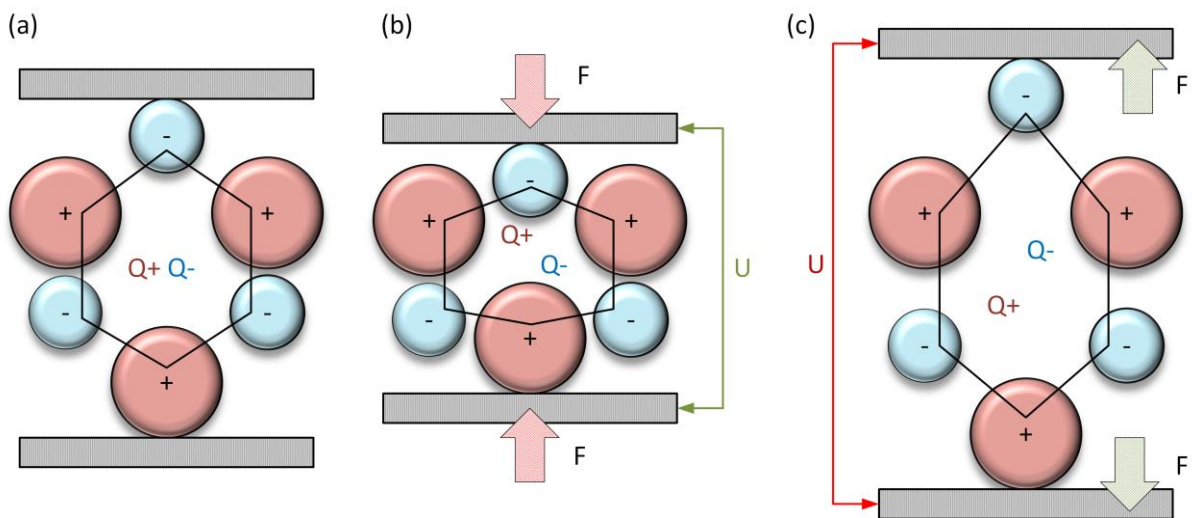

Fig. 2.2: (a) Schematic of the local charge distribution in the crystal without any mechanical load. (b) A compression force generates charges at the crystal surface. (c) A voltage applied at piezoelectric crystal base unit leads to a mechanical deformation of the crystal.

8

2.1.2   The piezoelectric effect

The mathematical description of the piezoelectric effect in the linear elastic regime [96, 97], is based on the electromechanical coupling between the mechanical and the electrical quantities, as it is shown in equation (2.1), (2.2), (2.3) and (2.4) [93, 98, 99]. The simplified forms of the electromagnetic equations are used here. The magnetic effects are negligible compared to the electric effects, due to their five orders of magnitude lower phase velocities. The superscript "E" and "S, T" indicates that the constants are measured at constant electrical field and strain, stress. Through symmetry considerations of $s_{ijkl} = s_{jikl} = s_{ijlk} = s_{klij}$, $d_{ijk} = d_{ikj}$ and $\varepsilon_{ij} = \varepsilon_{ji}$ the independent coefficients are reduced to 21 elastic, 18 piezoelectric and 6 dielectric permittivity constants, respectively. By introducing the displacement vector u, where $u_{ij} = \frac{\partial u_i}{\partial x_j}$, the distortion tensor $S = \frac{1}{2}(u_{ij} + u_{ji})$ can be linearized. Using the Voigt notation, which represents a symmetric tensor by reducing its order (11→1, 22→2, 33→3, 23→4, 13→5, 12→6), the variables μ and v are summed from 1 to 6 and *i, k* are summed from 1 to 3. This allows the equations to be written as given in (2.1) and (2.3). The latter equations can be transformed to (2.2) and (2.4) [93] by using the Einstein notation. The state of the crystal lattice is denoted by the vector of the electrical field *E* and the electric displacement *D*. The second order tensors characterize the mechanical strain *S* and the mechanical stress *T*. The constants of the coupling are *c*, which is the elastic stiffness, e is the piezoelectric constant, ε is the permittivity, *s* is the elastic compliance and *d* is the piezoelectric coefficient.

$$D_i = e_{i\nu}S_\nu + \varepsilon_{ik}^S E_k \qquad (2.1) \qquad\qquad D_i = d_{i\nu}T_\nu + \varepsilon_{ik}^T E_k \qquad (2.2)$$

$$T_\mu = c_{\mu\nu}^E S_\nu - e_{k\mu}E_k \qquad (2.3) \qquad\qquad S_\mu = s_{\mu\nu}^E T_\nu + d_{k\mu}E_k \qquad (2.4)$$

If equation (2.2) and (2.4) are considered for piezoelectric applications, two important coefficients can be determined. The first coefficient is the transversal piezoelectric coefficient d_{31} (2.5), in which the mechanical strain is perpendicular to the applied electric field strength. The second coefficient is the longitudinal piezoelectric coefficient d_{33} (2.6), in which the mechanical strain acts parallel to the applied electric field strength. The off-diagonal elements are neglected in this consideration due to their magnitude.

Transversal piezoelectric coefficient d_{31} $\qquad\qquad S_1 = s_{11}^E T_1 + d_{31}E_3 \qquad (2.5)$

Longitudinal piezoelectric coefficient d_{33} $\qquad\qquad S_3 = s_{33}^E T_3 + d_{33}E_3 \qquad (2.6)$

Generally spoken, the normal components d_{31}, d_{32} and d_{33} are most relevant for the operation of piezoelectric sensors and micro- or nanoscaled actuators. As shown in Fig. 2.3, the first subscript refers to the electrical field direction and the second subscript indicates the direction of the mechanical response.
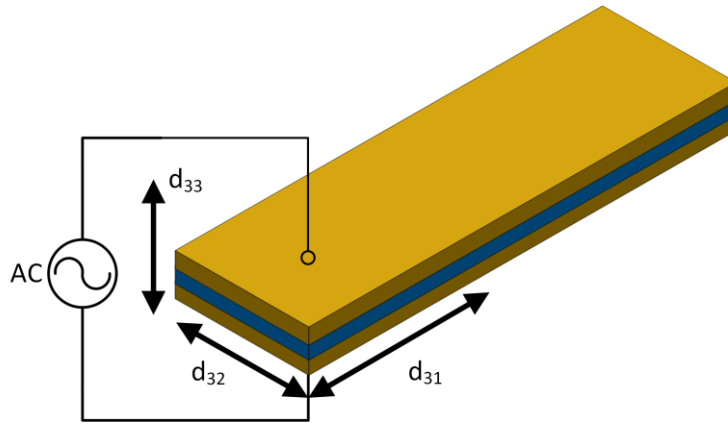
Fig. 2.3: The image shows the direction of the piezoelectric coefficients d_{31}, d_{32} and d_{33}.

2.1.3 Standard piezoelectric materials

When a piezoelectric material is selected for an application, it is generally selected in terms of the piezoelectric coefficients. In Tab. 2.1 three important piezoelectric materials for MEMS are compared.

T = 300 K	PZT	ZnO	AlN
Crystal structure	Perovskite	Wurtzite	Wurtzite
E_g [eV]	-	3 … 3.2	6.02 … 6.28
ε_r	407 … 5440	8.5	8.5 … 10.2
d_{31} [$10^{-12} \frac{C}{N}$]	-57.8 … -315	-5.12	-2.6 … -2.1
d_{33} [$10^{-12} \frac{C}{N}$]	60 … 640	12 … 17	2.75 … 5.4

Tab. 2.1: Comparison of key parameters of standard piezoelectric material for MEMS [47, 89, 100-103].

To exploit the applied voltage for the deflection of a cantilever best, a large d_{33} value is targeted. However, other aspects such as process integration effort and low contamination levels are required to reach this goal. Despite the large d_{33} value of PZT [89] compared to zinc oxide (ZnO) [47] or AlN [101], it has major drawbacks in terms of process integration for silicon MEMS. Its high fabrication temperature of around 1000 °C at the sintering process [65] leads to contamination with oxygen or carbon. It also leads to surface cracks or delamination of the fabricated layer. Further, the fabrication requires a highly temperature stable bottom electrode to connect the layer electrically. Compared to ZnO or PZT, AlN is preferred as functional material, since AlN is compatible with standard complementary metal-oxide-semiconductor (CMOS) microfabrication processes [65] and offers a high temperature stability [56, 66].

Considering the integration into MEMS [36, 104], many device architectures have in common that they are based on either membranes or cantilevers as main building blocks. A piezoelectric excited millimetre-sized cantilever sensor is used as an example for the detection of chemical quantities. To detect *E.coli* bacteria, a cantilever is coated with a nutrient layer, where the bacteria grows while the change of the resonance frequency is observed [105]. Another example is shown at [106], were the antibiotics vancomycin binding with a change of the cantilever deflection is examined.

To measure physical quantities, for example mass, acceleration, pressure and force, a piezoelectric layer stimulates a vibrating structure. In order to measure acceleration, a piezoelectric layer is used to excite the cantilever, while a proof mass is placed at the free end. With this setup, a wide range of resolution and maximum acceleration can be detected when choosing a specific device design [47]. A differential pressure sensor for a range from -20 Pa to +20 Pa with an applied piezoelectric AlN layer is demonstrated in Ref. [48]. Forces can also be measured with a thin film bulk acoustic wave resonator (FBAR). Depending on the applied force of up to 4 mN a proportional frequency shift is detected [49]. Moreover, when making use of the influence of liquid on an immersed cantilever, which is excited from an AlN piezoelectric layer, the determination of viscosity is possible [50].

2.1.4   Aluminium nitride (AlN)

In the case of piezo-electrically excited silicon MEMS devices, sputter deposited AlN is often the material of choice [62, 104]. The thermal expansion coefficient is $4.5x10^{-6}\frac{1}{K}$, what results in a low temperature-induced stress level between AlN and Si ($2.6x10^{-6}\frac{1}{K}$). Compared to other piezoelectric materials, AlN has the highest surface acoustic wave velocity of $11.4x10^{3}\frac{m}{s}$ [107]. At room temperature, the AlN crystal has a large band gap of 6.2 eV [108]. As aluminium nitride is transparent in the wavelength range of 0.5-3.0 µm, it is suitable as filter material in optical or optoelectronic devices in the infrared (IR)-range [109]. Even in polycrystalline state, AlN offers a remarkable temperature stability up to 1000°C in non-oxidising gas atmosphere, as demonstrated by post-deposition annealings [56, 66].

AlN has a wurtzite crystal structure, which is presented in Fig. 2.4. A slightly larger bond of Al and N along the so-called c-axis in contrast to the a-axis leads to a charge displacement and hence, to an intrinsic dipole moment. Therefore, the piezoelectric effect occurs due to the III-V binding of Al and N. To ensure the highest values in piezoelectric coefficients, the c-axis orientation must be implemented with tailored sputter deposition parameters. In addition, the surface properties of the substrate, on which the AlN layer is deposited, has a great influence on the layer growth. A reliable pre-conditioning of the surface is achieved by applying an inverse sputter etching (ISE) resulting in enhanced film properties such as the piezoelectric coefficients [110].
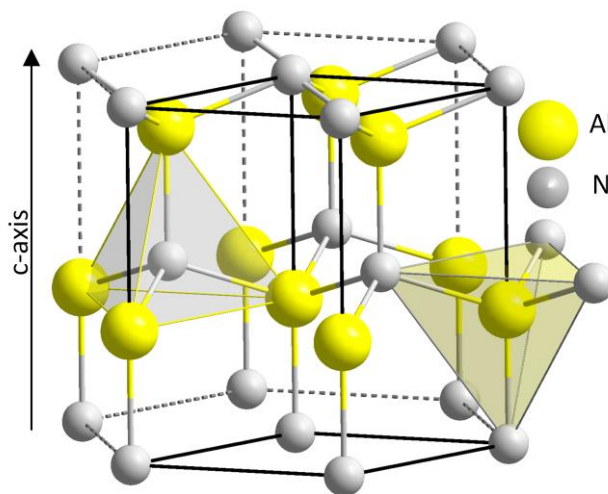

Fig. 2.4: AlN crystallographic structure of AlN (wurtzite) with coordination polyhedral [111]. The Al atoms are coloured in yellow, the N atoms in grey.

The use of thin films of AlN as an actuator or sensor element is based on the electrical excitation or electrical response when the thin film is mechanically loaded. A large d_{33} value indicate a large d_{31} value [112, 113], which is particularly important for exciting and detecting oscillations of cantilevers in AFMs. A reasonable value for the d_{33} is 5 pC/N [63, 104, 114].

2.2   Fabrication process of AlN MEMS cantilevers

With vapour deposition processes piezoelectric thin layers for MEMS devices are realized. These processes are classified into physical and chemical deposition techniques. Examples within the physical vapour deposition (PVD) domain are DC and AC sputter deposition, molecular beam epitaxy (MBE), e-beam evaporation and pulsed laser deposition (PLD). Examples for the chemical vapour deposition (CVD) are plasma enhanced CVD (PECVD) and low-pressure CVD (LPCVD). The piezoelectric and metallic layers on the cantilever are formed by two PVD processes, namely by sputtering and by e-beam and thermal evaporation processes.

2.2.1   PVD (Physical vapour deposition)

Sputter process

Sputtering is the standard process for AlN thin film deposition [47, 115-117]. By applying voltage in a parallel plate capacitor configuration, the process gas within the vacuum chamber which is typically argon gets ionized at a back pressure of a few µbar. The ions are accelerated by the electric field and hit a plate made of the material to be deposited (target). Atoms are knocked out of the target by the transferred energy. Due to the local field distribution in the vacuum chamber, these atoms are accelerated from the target to the substrate, whereby they lose part of their kinetic energy through scattering with the process gas. The scatter also leads to the fact that the direction of the particles pre-defined by the electric field is broken up so that they impinge on the substrate in a wider-angle distribution. This means sputtering has a much better edge coverage than evaporation deposition. Due to the low selectivity during high-energy ion bombardment, pre-alloyed material systems can be synthesized as thin films close to the chemical composition of the target. A disadvantage of sputter deposition compared to other vapour deposition processes is the higher process pressure, which can lead to gaseous inclusions in the layers. By using a magnetron above the target, the degree of ionization of the plasma can be increased, since the electrons are forced into spiral trajectories by a magnetic field and thus their average mean time in the plasma is increased. This leads to a higher sputtering rate. A schematic representation of a sputtering system is shown in Fig. 2.5.
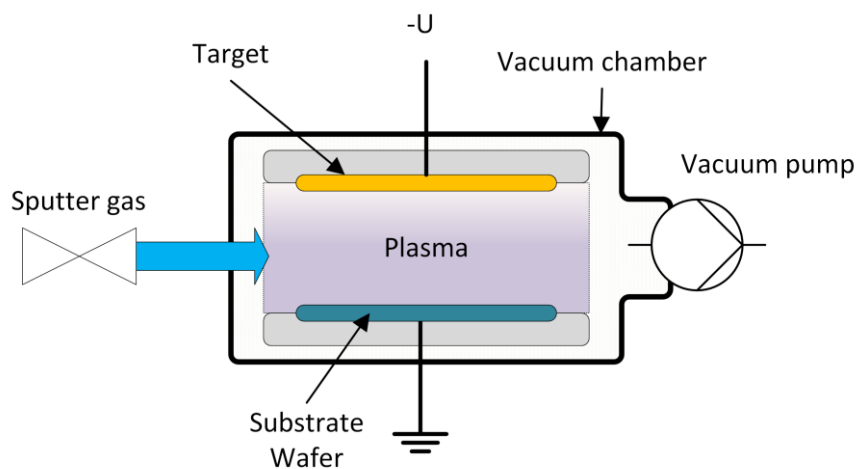

Fig. 2.5: Schematic of a sputter system indicating important components.

Reactive sputtering process

Aluminium nitride thin films can be made by reactive sputtering technology. The target consists of pure aluminium, while the second reactant nitrogen is made available as admixture to the process gas. The reaction to AlN takes place directly on the substrate surface.

Sputter etching

Although this process is not a deposition process, it is closely related to sputtering, for this reason it is listed here. By reversing the bias voltage, the gas ions (*e.g.* Ar$^+$) are accelerated in the direction of the substrate, which leads to material removal. The etching is a pure physical process since there is no chemical reaction with the substrate. The gas ions are forced by the electric field geometry in the preferred direction normal to the substrate surface, which results in an anisotropic etching profile. Sputter etching (also ISE for inverse sputter etching) is mostly used as a preparation step for the subsequent deposition of thin films in order to clean or pre-conditioning the substrate surface.

AlN deposition with Mo substrate holder

One goal of this work is to increase the reliability of the manufacturing process of piezoelectric AlN coated MEMS cantilevers. Therefore, an industry type DC-magnetron-sputter-equipment from VonArdenne LS730S is used. To start, the sample wafer is placed on a molybdenum (Mo) sample holder (Fig. 2.6) inside the deposition vacuum chamber. At a back pressure of P = 2 µbar, pure nitrogen gas N$_2$ is introduced in the chamber with a flow rate of 50 sccm. The 620 µm and 1 µm thick AlN layers are deposited with a DC power of P_{sp} = 800 W from a 6" Al target, which is fixed at a distance of 65 mm from the substrate. Basic process steps and the corresponding process parameters already have been reported in [43, 110, 118-122], while specific parameters introduced for device fabrication are discussed in the next chapter.

Fig. 2.6: Photo of a standard molybdenum (Mo) sample holder as provided by VonArdenne.

E-beam and thermal evaporation processes

Evaporation processes are used to produce the electrical layers on the cantilever. The material which will be applied is thermally transferred into the vapour phase and then condenses on the cold substrate. Gas inclusions in the layers are avoided by a high vacuum of $< 10^{-6}$ mbar. This achieves a high mean free path of the atoms in the vapour phase as well as a linear movement. The resulting poor edge coverage is advantageous for the lift-off structuring, because of the deposition free edges, where the lift-off solvent attacks sacrificial layer. The boat, filled with the desired deposition material, can be heated both by resistance heating and by an electron beam. The electron beam evaporation enables an evaporation of materials with very high melting points. The local melting of the electron beam results in a lower degree of contamination of the deposition layer than the deposition with the resistance heated boat [123].

2.2.2 Cantilever fabrication process with Ti-hard-mask

To improve the reliability and, consequently, the yield in device fabrication compared to the reference process as described in Ref. [124] due to a reduced number of process steps titanium (Ti) as sacrificial layer is introduced for AlN thin film patterning. The complete schematic process flow of the AlN cantilever fabrication process is shown in Fig. 2.7. All the following process step numbers refer to the manufacturing process as shown in the figure.
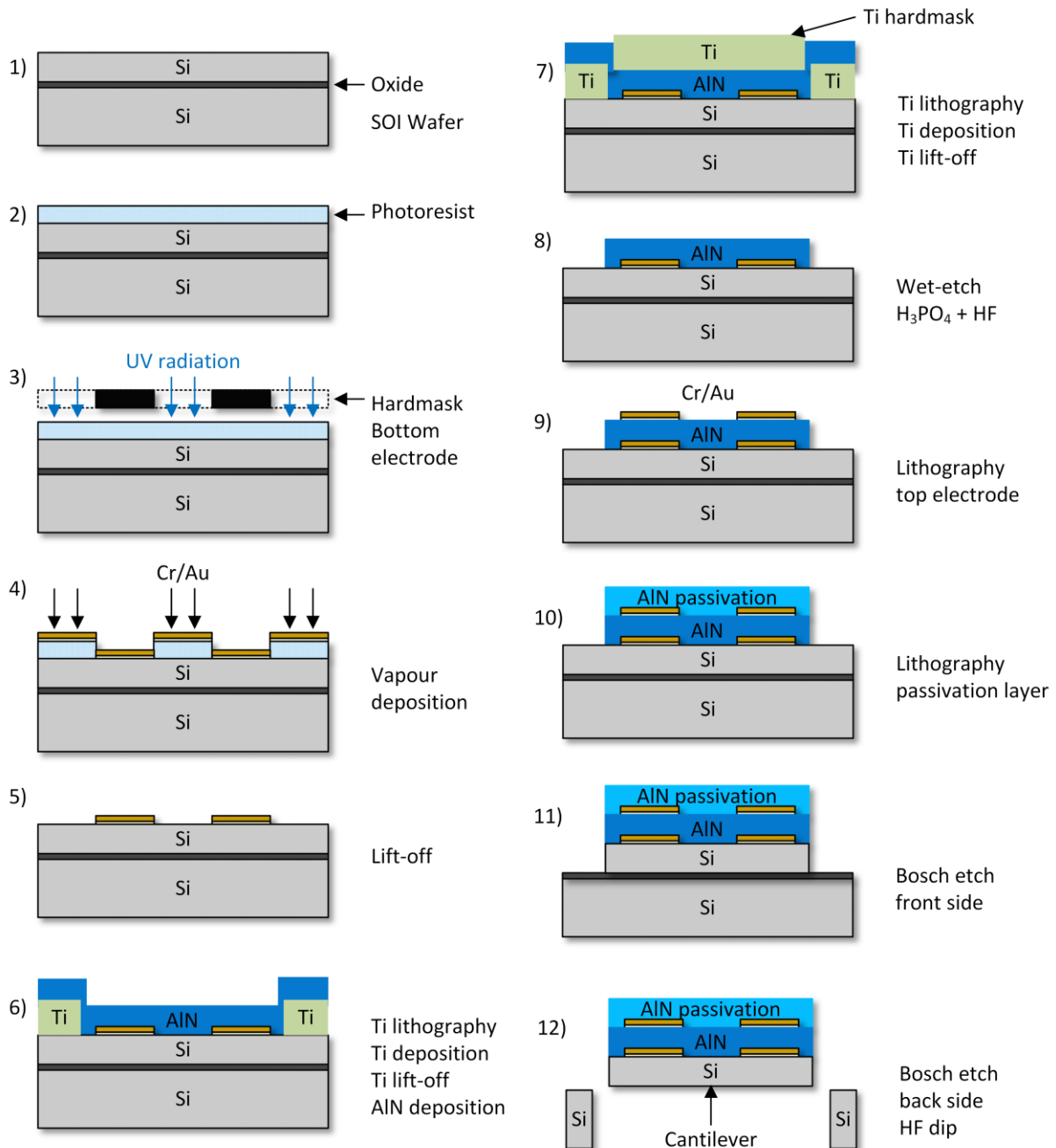
Fig. 2.7: Schematic flow chart of cantilever fabrication process with Ti as sacrificial layer. (1) Blank SOI wafer. (2 – 5) Lithography and metallic thin film deposition for bottom electrodes. (6 – 8) Lithography, deposition and lift-off of the Ti sacrificial layer to pattern the piezoelectric AlN layer. (9 – 12) Process steps for top electrode realization, AlN passivation and the release of the device from the bulk Si.

To start, a silicon-on-insulator (SOI) wafer is used (1). A thin layer of stress compensating oxynitride, composed of a thermal silicon oxide (SiO$_2$) and a stoichiometric silicon nitride (Si$_3$N$_4$) layer, serves as an electric insulation layer, which is omitted from the process flow for simplicity reasons. The bottom

14

electrode is fabricated by a lithography step (2-3) with subsequent deposition of a bi-layer of chromium and gold (Cr-Au) (4). Thereafter, a lift-off process defines the bottom electrode (5). To realize piezoelectric elements, a Ti-hard-mask is used to form the AlN structure and AlN is reactively sputter-deposited all over the wafer surface (6). The second Ti-hard-mask is realized with another lithography step with a subsequent Ti-deposition and lift-off process, respectively (7). To excavate the AlN layer, the surface is treated with phosphoric acid H_3PO_4 and hydrofluoric acid HF (8). Like the bottom electrode, the top electrode is produced by a combination of photolithography, deposition and lift-off step (9). To ensure the durability of the electrodes and protect them from the environment, the electrode surface is covered with an additional AlN layer (10). Its fabrication is similar to the fabrication of the Ti-hard-mask and the following wet chemical process step which is presented in steps 6-8. Finally, the device is defined by a front side deep reactive ion etch (DRIE), see step (11) followed by a backside DRIE release etch (12). The final device, which is schematically shown in Fig. 2.8, consists of the bottom and top electrode and of the active device layer. After sawing, the dies are glued into a standard DIP24 package (Minitron). The gold pads of the device are electrically bonded with gold wires to the housing pins.
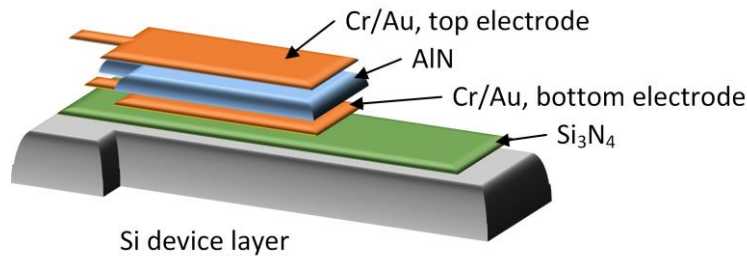
Fig. 2.8: Schematic illustrating the structure of the MEMS cantilever with integrated AlN transducer elements.

2.2.3   Process parameters of cantilever fabrication with Ti-hard-mask

Here, the basic process of lithography, deposition and lift-off of various materials is described [121]. The parameters shown are the basis for the further fabrication process development in this thesis.

Lithography

First, the organic photosensitive image-reversal resist from Microchemicals (AZ5214E) is spin coated on a wafer surface with a rotation speed of 3000 rpm. After a pre-backing step with a duration of 5 min at 107 °C, the wafer is exposed to UV light for 4 s to transfer the mask layer. A heat treatment with a duration of 5 min on a hot-plate at 107°C prepares the wafer for the image reversal step. Next, the entire wafer area is flood exposed with UV light for 30 s and subsequently, a heat treatment of 2 min at 120 °C follows.

Sputter deposition

A standard Mo sample holder as provided by the manufacturer of the sputter equipment carries the wafer in the vacuum chamber, where a magnetron sputter process with an Al target is used to deposit the piezoelectric AlN layer. The deposition is performed at 800 W plasma power, at a back pressure of 2 µbar and a N_2 gas flow of 50 sccm, respectively.

The metallic electrodes (Au, Cr) are deposited at 100 W and the sacrificial layer (Ti) is deposited at 900 W and with 60 sccm argon (Ar) at 3 µbar.

Lift-off

In the lift-off process the solvents acetone and isopropanol are used to dissolve the organic sacrificial layer until the overlying layer is detached. The necessary negative edges can be generated by using an

image reversal resist. The resist will be used as sacrificial layer and should not be completely covered by the layer deposited on top. To achieve this, an anisotropic deposition process is important.

Basically, the Ti-hard-mask process works similar. Titanium is used as the sacrificial layer in contrast to organic resin. In preparation for the lift-off, the wafer is placed for 5 min into a H_3PO_4 bath at 75 °C, where the AlN is etched. The remaining residues are simultaneous removed with the Ti-hard-mask (sacrificial layer) by a 20 s immersion into a 40% HF solution.

2.3   Thin film characterization

This section lists the equipment for analysing the deposited AlN layers. Each method is introduced in a compact way explaining the basic working principle and how the method is used in this work.

2.3.1   Atomic force microscopy (AFM)

The AFM is a high-resolution technique that generates images from a physical surface scan. It scans the sample surface topography with a tip which is placed at the free end of a cantilever. The tip interacts with the surface and affects the cantilever movement. This is captured by the optical readout. The cantilever is excited by a tapping piezo with a frequency near its resonance frequency. The AFM application can range from metallic surfaces to biological samples, while the sample environment can range from vacuum to liquids. The material and the shape of both, the tip and the cantilever, depend on the application. Fig. 2.9 illustrates an exemplary application of the non-contact operation mode, the so-called tapping mode. Apart from that, an AFM can also be operated in contact mode. The major advantages of AFMs are the detection of the topography information, where 3D imaging of microstructures and roughness measurements are possible [37]. Even more, by carefully selecting suitable tips and cantilevers, for example magnetic surfaces (Magnetic Force Microscopy – MFM), surface potential (Surface Potential Microscopy – SPoM) or tunnelling current (Scanning Tunnelling Microscopy – STM) can be characterized at the nanoscale. Especially in this work, all fabricated samples are scanned with a NCHV-A cantilever inserted into a commercially available AFM from Bruker (Dimension Edge) [125]. The equipment has a maximum scanning area of 90 µm by 90 µm and a Z-range of 10 µm with a noise level of 0.2 nm in the Z-direction. The cantilever has a length of 117 µm, a width of 33 µm, a thickness of 3.5 µm (all are nominal values) and a resonance frequency of 320 kHz. The tip has a height of 10 to 15 µm and a radius of about 8 nm [126].
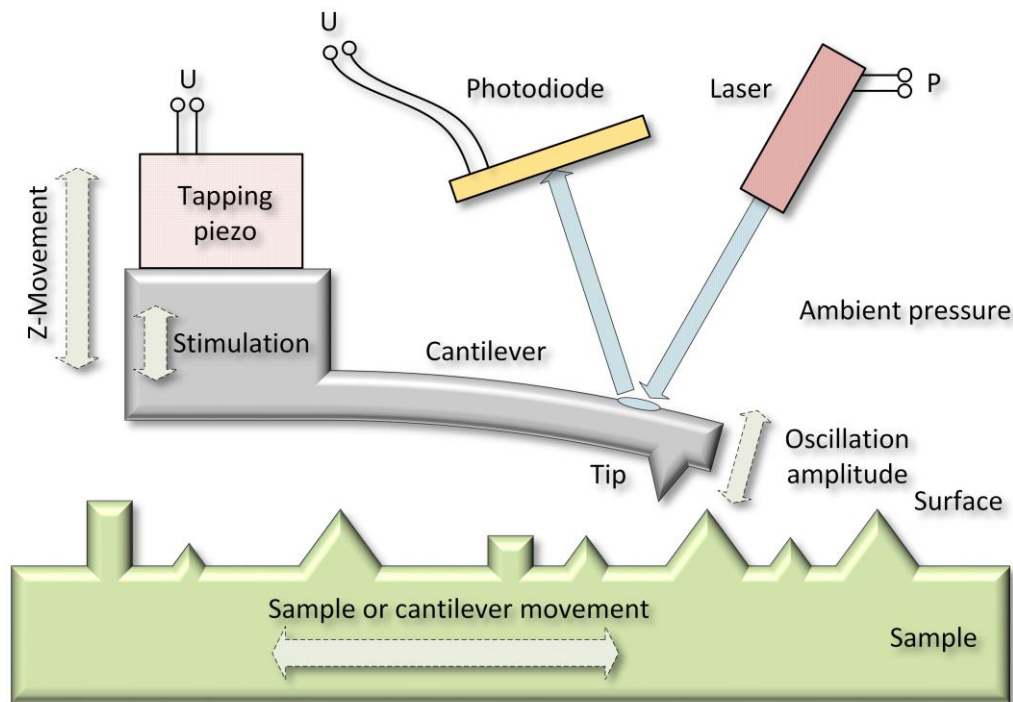
Fig. 2.9: Schematic drawing of an AFM operated in air in tapping mode with optical read-out.

2.3.2 Scanning electron microscopy (SEM)

The SEM operates in vacuum environment, where a focused electron-beam is accelerated and directed onto the sample surface. An electron detector records the emitted electrons from that surface upon the interaction of the electron beam with the surface. Typically, the secondary electrons are picked up in order to extract information of surface topography and chemical composition. The local response is improved when using multiple detector arrays. To obtain an image of the surface, it is scanned by the electron beam and the individual scan strips are shown assembled on the screen. Fig. 2.10 shows a simplified schematic drawing of a scanning electron microscopy with the electron-beam emission, the beam forming (condenser-lenses, apertures), the XY alignment and the detectors. The surface image is generated from *e.g.* the backscatter electron detector or the secondary electron detector or from a combination of both detector signals. Additionally, an energy-dispersive X-ray spectroscopy (EDX) is used to analyse the material composition surface-near. To minimize beam dispersion, the beam has to be guided under ultra-high vacuum (UHV) conditions to reduce scattering, thus ensuring a sufficient mean free path for the electrons. The fast-captured and high-resolution images are an outstanding advantage of the SEM technique and the method is available for many applications ranging from *e.g.* soft biological (with metallic coating) to hard materials such as silicon samples [127]. In this work, the SEM from Hitachi SU8030 [128] is used to investigate the topography and the morphology of etched surfaces. The secondary electron image resolution of the SEM is about 1 nm and the magnification is up to 800 k. The scan area has a maximum of 150 mm in diameter and the scan speed has two options: while it has 6.25 or 7.5 frames per second at fast scan, the slow scan speed varies from 80 to 1 seconds per frame for a full screen resolution of 1280 by 960 pixels. The specimen chamber is evacuated to a pressure of approx. 10^{-4} Pa.

When preparing the samples, especially isolators, a certain conductivity has to be guaranteed to dissipate the electrons away from the surface. Therefore, the samples are glued on the sample holder with copper tape. Even with this measure, charging effects still occur when analysing the surface. To keep the latter impact as low as possible, the position of the scan area is moved before the image is captured.
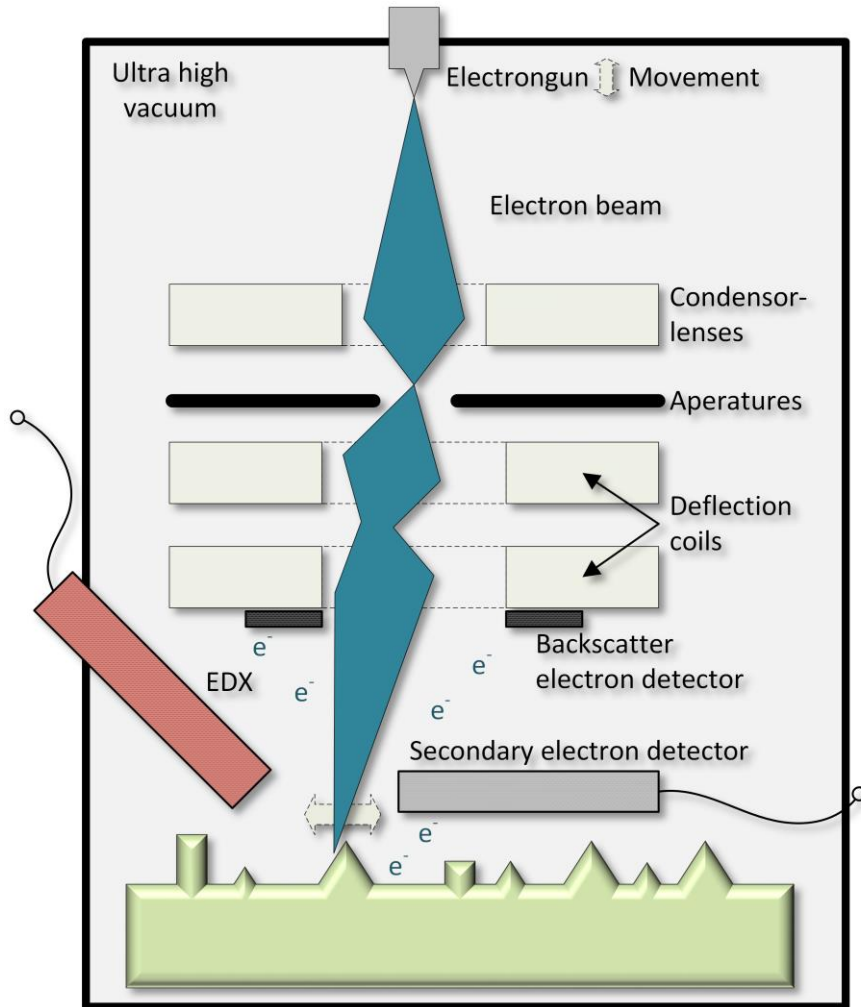
Fig. 2.10: Schematic of a SEM highlighting important components for beam guidance and exemplary detectors i.e.: backscatter electron detector, secondary electron detector and EDX.

2.3.3   Laser Doppler vibrometer (LDV)

A LDV enables contactless displacement and velocity measurements. A laser beam is emitted to a vibrating surface and the reflection of a laser beam is recorded to characterize the vibration of MEMS and nanoelectromechanical systems (NEMS). The principle is shown in Fig. 2.11.
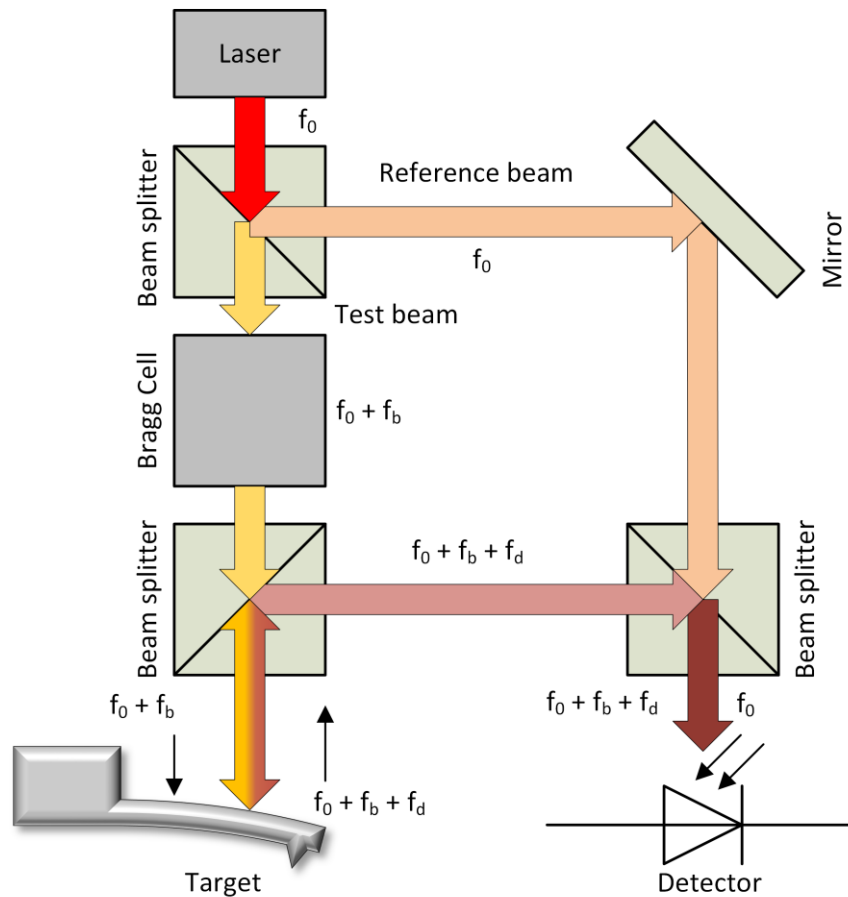
Fig. 2.11: Schematic set-up of a laser Doppler vibrometer.

A laser source emits a laser beam with a frequency of f_0, which is divided into a reference and a test beam via a beam splitter. The test beam is directed through the Bragg cell, which adds a frequency shift f_b to the emitted laser beam. This beam is guided directly onto the target. The motion of the cantilever adds a Doppler shift f_d to the reflected beam, which is backscattered to the LDV. This beam is then collected and guided through two beam splitters. The second one combines the reference beam with the beam from the surface and guides it to the detector. This beam contains the information of the frequency-, amplitude- and phase- difference. The processing unit demodulates the superposition of both beams and derives the speed of the measurement point. To record the mode shape of a cantilever beam, the laser beam scans over the surface. Due to the non-contact measurement approach, it does not have any influence on the cantilever oscillation. In this work, a MSV-400 and a MSV-500 both purchased from Polytec are utilized to analyse the frequency spectrum of the first out-of-plane mode of the cantilevers with integrated piezoelectric transducers. The light source emits a visible red laser beam, which has a wavelength of 633 nm. With the right choice of decoder, which depends on the application, displacement measurements up to 20 MHz are possible.

Vacuum chamber

To investigate the impact of different back pressure levels on the oscillating cantilever, a vacuum chamber was designed. Furthermore, the chamber is equipped with support holes to house the shaker piezo PCB, which is used for the experimental superposition measurement set-up (see in the results chapter with the title "Measurement System: Frequency generator (FGEN) and oscilloscope (DSO)"), amplifier and stimulation circuits.

A Pfeiffer vacuum turbo pump makes the adjustable vacuum down to 8 mbar at the vacuum chamber, which is needed to neglect the damping effect of air on the oscillating amplitude of the vibrating

cantilevers [32]. Fig. 2.12 (a) shows the CAD image of the vacuum chamber and Fig. 2.12 (b) shows the 3D view of the chamber with the openings for the feedthroughs (BNC, SUB-D, USB and the optical port). Fig. 2.12 (c) shows the arrangement with LDV and the vacuum chamber for cantilever speed measurements.
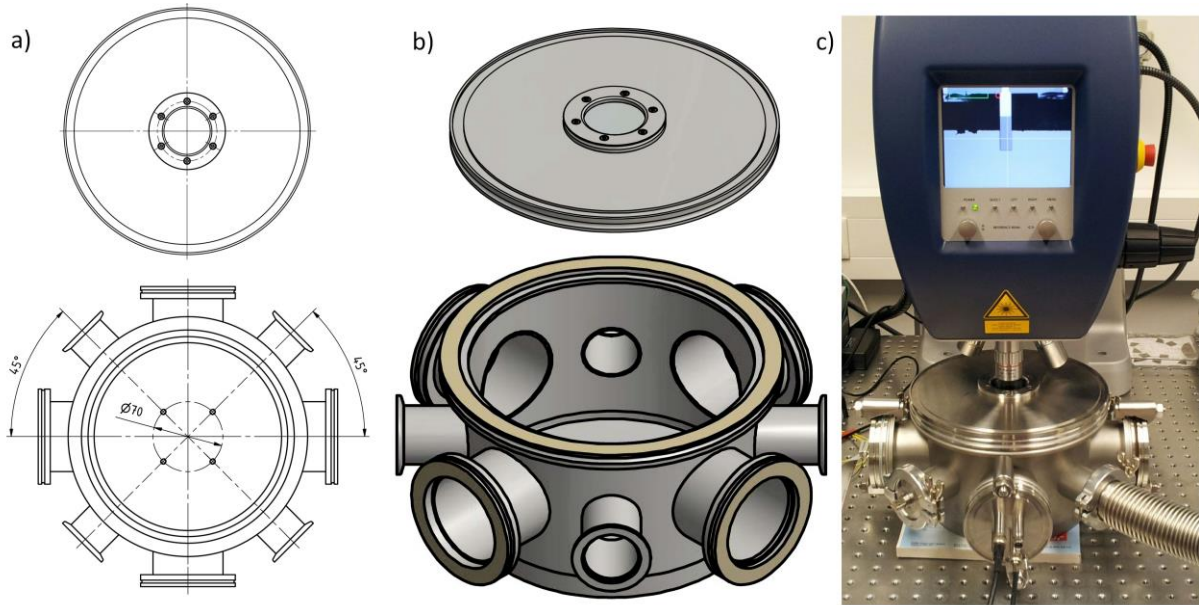
Fig. 2.12: a) shows the schematic view for vacuum chamber and lid with an optical feedthrough, b) shows the 3D image of vacuum chamber and lid and c) shows the measurement setup with the LDV.

2.3.4   X-ray diffraction (XRD)

An XRD is a non-destructive analytical method, which provides crystallographic information of materials by observing the diffracted X-ray beam. The X-ray beam is directed towards the sample surface and penetrates into the crystal structure. Due to the delay difference of neighbouring crystallographic planes, interference patterns due to the constructive and destructive interaction of different beam components are generated. The constructive interference follows Bragg equation $2d_{lat}sin(\vartheta) = n\lambda$, which depends on an integer multiple *n* of the wavelength λ, the angle of incidence ϑ and the latter distance d_{lat}. The correlation is shown in Fig. 2.13. During the measurement procedure, the sample is fixed horizontally and the X-ray source and the detector moves with a fixed angle of ϑ [129].
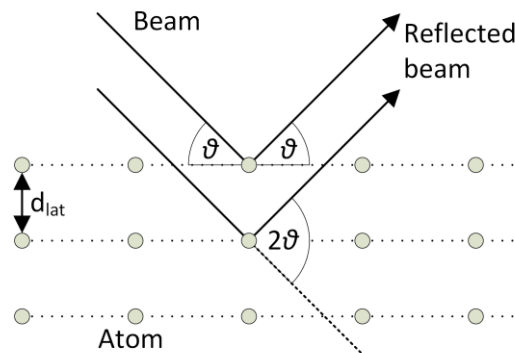
Fig. 2.13: Schematic of the diffraction interaction of X-ray beams at a crystalline lattice.

For this work, a PANalytical X'Pert PRO from Malvern Panalytical determines the Bragg-Brentano (θ/2θ) reflection spectrum of AlN thin films, which are deposited on Si wafers. The

copper (Cu) tube of the XRD operates at 40 kV and at 40 mA ($CuK_{\alpha1}$, $CuK_{\alpha2}$). The equipment is capable of divergence slits ranging from 1/2° to 1/32°.

2.3.5 Pyrometer temperature measurement

To be able to assess the dependence of the sputter deposition temperature, the temperature of the sample is measured continuously during thin films deposition. While the sputter deposition process is ongoing, the particle bombardment heats up the sample surface, and in consequence, the sample holder. Common to all sputter-deposition processes, the synthetization of AlN thin films strongly depends on the temperature of the sample surface, as changes of the temperature will influence the electrical and mechanical material parameters (*i.e.* leakage current, film stress). To control this important process parameter, the sample temperature is measured with a DIAS Pyrospot DGE 10N pyrometer [130], which is pointed at the backside of the sample holder. The pyrometer offers a temperature range from 100 °C to 850 °C at a spectral range from 2.0 µm to 2.6 µm.

2.3.6 Leakage current measurements

Previous studies of the conduction mechanism of AlN show dominant Pool-Frenkel behaviour (PF). The exponential behaviour [131] of the leakage current density *J* is expressed as a function of *E* and *T* given the following equations:

$$J(E, T) \propto E * e^{\frac{-E_A}{kT}} \tag{2.7}$$

$$E_A(E) = q\left(\phi_B - \sqrt{\frac{qE}{\pi \varepsilon_0 \varepsilon_r}} \right) \tag{2.8}$$

The symbols are the elementary charge q, the barrier height ϕ_B, the relative permittivity ε_r, the electric constant ε_0, the Boltzmann constant k and the associated activation energy $E_A(E)$ [132]. A reasonable value for ε_r for sputter deposited AlN thin films is 10, which has been determined in previous investigations layers deposited with the same equipment [120].

Here, the leakage current measurement is done with the Agilent source measurement unit B2911A. It is capable to measure currents down to 10 fA at a minimum supply voltage of 100 nV. The electrodes of the sample are connected to the source measurement unit via needles in a Süss PM 8 probe station. The probe station is equipped with a chuck from ATT A300 which allows to heat the sample up to 300 °C. To prevent any unwanted temperature, vibration or light-induced effects, the probe station is located in an air-conditioned room, placed on an air damped table and the room is dimmed during the measurement cycles. The main components of the measurement setup and the sample are marked in Fig. 2.14 (a). Considering that the charging of the AlN thin film is a dynamic process, the leakage current measurement averages 10 current values with a cycle time of 250 ms after the decay of the initial charge current. Fig. 2.14 (b) shows a typical current characteristic where after 5 τ the current can be regarded as stable over time. The measurement procedure comprises of a voltage sweep from -20 V to 20 V in 80 steps and back, performed twice, as shown in Fig. 2.14 (c). A MatLab script automatically measures the leakage current and controls the temperature of the wafer chuck. The sample temperature varied between 25 °C and 300 °C in air. Due to hysteresis effects at lower temperatures, the evaluation of the barrier height was restricted to temperatures ≥ 100 °C [133, 134].
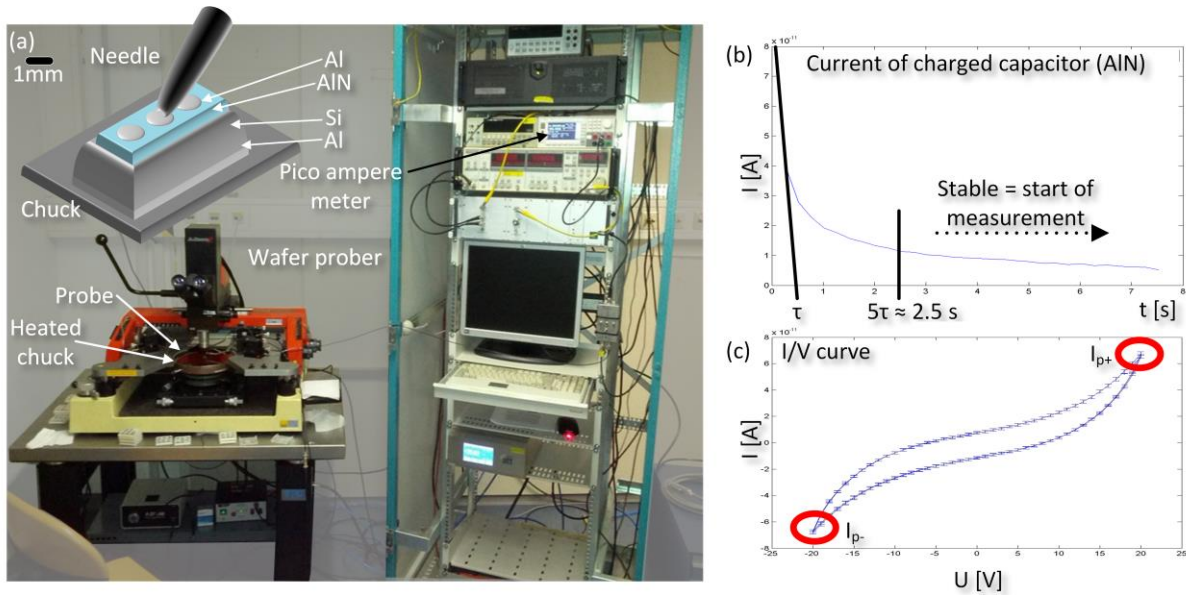
Fig. 2.14: Photographs of the leakage current measurement equipment including a schematic of the test samples (a), a representative example of the charging curve (b) and the corresponding I/V curve (c).

2.3.7 Piezoelectric coefficient measurements

The piezoelectric coefficient d_{33} is measured with a commercially available piezometer, PM300 from Piezotest. The equipment is shown in Fig. 2.15 (a). The measurement principle is based on the Berlincourt method [135] which measures the parameter at a low frequency compared to the resonance frequency. As it is shown in Fig. 2.15 (b), the sample is clamped between two electrodes and an oscillating force F vertical to the piezoelectric thin film surface is applied. The piezometer compares the resulting electrical signal with an internal reference and determines the d_{33}. It has a tolerance of ±0.01 pC/N at the used "very low range" of 0 to 10 pC/N. The measurements are done with an oscillation frequency of 110 Hz.

Fig. 2.15: The image shows the piezometer PM300 with an exemplary sample clamping.

2.3.8 Wafer bow measurements (film stress)

The film stress σ (Pa) measurements are carried out with a contactless wafer geometry gauge from E+H Metrology MX 203-6-33 (Fig. 2.16 (a)). The 4" measurement set-up consists of 33 parallel arranged capacitive sensors which are embedded into heavy plates. It has a resolution of 50 nm. The wafer bow of the test wafer is measured before and after the deposition. The average stress of the deposited thin

layer can be calculated from the wafer bow difference, as the bending of the wafer depends on the sign of the stress of deposited layer. A tensile layer stress, where the stress value is positive, leads to a convex wafer bending Fig. 2.16 (b) and a compressive stress, where the stress value is negative, leads to a concave wafer bending Fig. 2.16 (c).
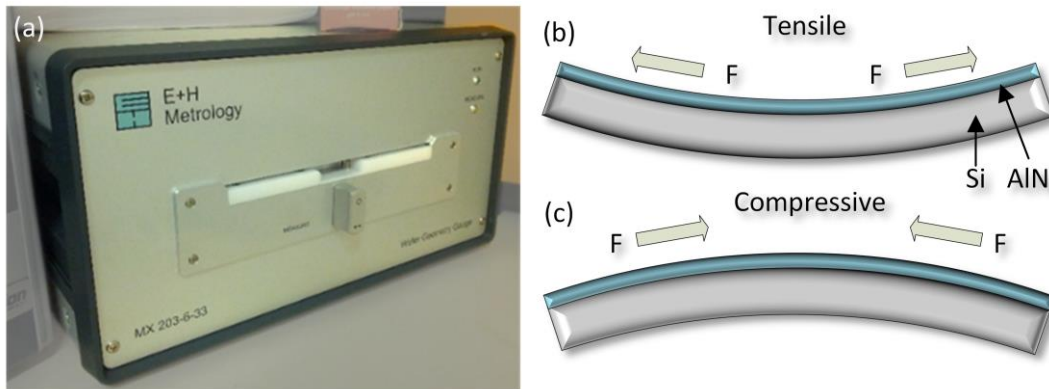
Fig. 2.16: The photograph shows the measurement equipment from E+H Metrology. A convex wafer results from a (b) tensile layer stress and a (c) compressive layer stress obtains a concave wafer of a deposited layer on the silicon surface.

2.3.9   AlN etch residuals analysis

Stable and controlled reactive deposition parameters result in repeatable, ideally dense and homogenous AlN layers [118, 136, 137]. The deposited thin layers, which act as oscillation stimulation for AFM cantilevers, require a low film stress to prevent any static deflection. The effect of deposition temperature on the film stress and further the impact on the etching behaviour of AlN is determined. Doing so, the fabricated samples are exposed to an Aluminium-etch solution (1-5% HNO_3, 65-75% H_3PO_4, 5-10% CH_3COOH) from MicroChemicals. The samples are immersed for a defined time (20 s to 1800 s) and temperature (85 °C). The expected etching results are described in the literature [136, 137]. To investigate the impact of layer stress on the etching behaviour, SEM images are taken of the etched AlN layer to determine the amount and lateral sizes of residues after etching.

With a graphic software tool called ImageJ, Fig. 2.17 (a), the resulting micrographs from SEM measurements were post-processed. Doing so, the opportunity is given to analyse the particle density from images taken from all kind of microscopes and hence, it gives the opportunity to study the etch performance of AlN layers as a function of different etch parameters. Fig. 2.17 (b) shows a representative of an etched AlN film. An overlay function with "Find Maxima" and "Threshold ("Huang dark")" identifies areas with AlN residues. In detail, "Find Maxima" locates the brightest spot of the residues and accumulated residues will be separated, as illustrated in Fig. 2.17 (c). The "Threshold" function subsequently isolates the residues from the substrate due to the different grey tone. To get the area of the residues, the function "Analyze Particles" of ImageJ counts all residues within the image and provides a list of residue sizes of the image.

The post-processed images of that particle analysis are shown in Fig. 2.17 (d). In the right part of each micrograph the original picture is shown, whereas in the left half the detected residues are visualized by green lines.
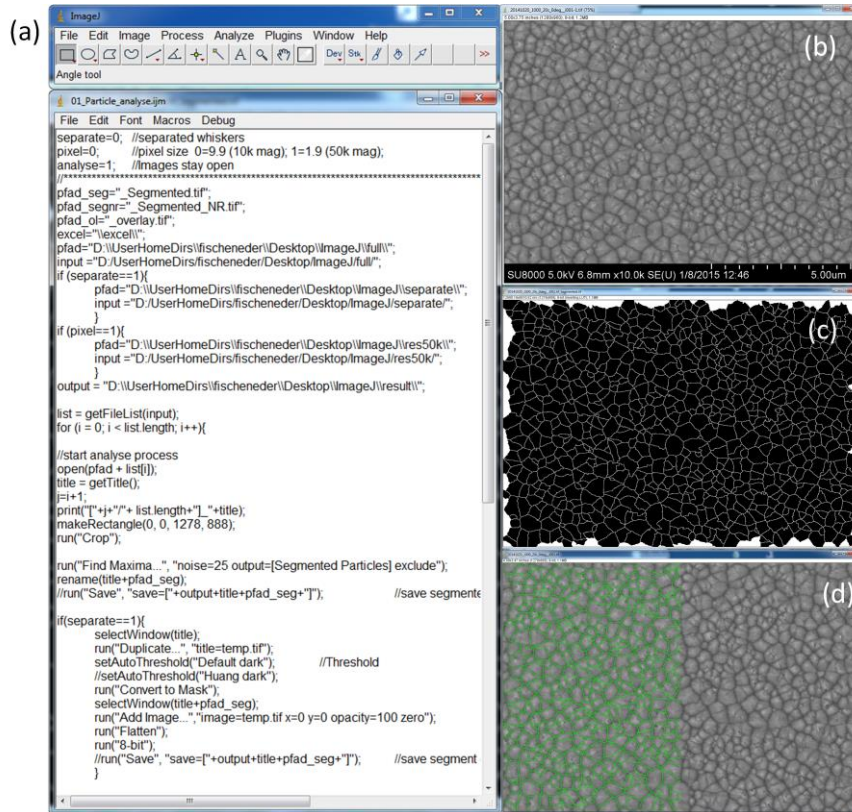
Fig. 2.17: The figure shows (a) ImageJ with main window and script sample, where (b) shows the SEM image of etched AlN surface sample, (c) shows the segmented view of the AlN surface sample for particle analysis and (d) shows original image on the right and the detected residues visualized on the left.

3 Simulation of MEMS cantilevers

The oscillation characteristics of resonantly excited piezoelectric MEMS are described by the mechanical differential equations (Euler-Bernoulli). In addition, the finite element simulation (FEM) helps to describe the mechanical interaction of a piezoelectric layer with the corresponding electrical layers and the influence of the anchor region, representing the connection point between the cantilever and the silicon frame. The superposition of both mechanical excitation routes provided by the macroscopic, piezoelectric shaker and the on-chip integrated, piezoelectric thin film transducer, as well as the influence of a phase shift between both stimuli are examined. The outcome is used for the geometrical cantilever design. Apart from the geometrical and material pre-definitions, the theoretical prediction of three different cantilever operation modes are presented in this chapter: the simulation of pure mechanically driven oscillation, of a piezoelectrically stimulated oscillation and the superposition of both. Furthermore, the impact of geometrical dimensions of the integrated, piezoelectric layer on the cantilever oscillation and its influence on the Q-factor of the resonantly operated MEMS cantilevers are considered.

3.1 Resonant operated MEMS cantilevers

Basically, the oscillation direction of resonant operated MEMS cantilever distinguishes into in-plane, out-of-plane and torsional modes, respectively. Typically, the first out-of-plane-mode is used for AFM applications. It has the highest oscillation amplitude which is beneficial for measurements in tapping mode [37, 101]. By assigning material parameters to the model, the determination of the Q-factor of an out-of-plane oscillation is possible. The chapter concludes by presenting an electrical equivalent circuit that enables a straightforward prediction of the cantilever frequency behaviour.

3.1.1 Mechanical oscillation of MEMS cantilevers

A damped harmonic oscillator is described by the ordinary time-dependent differential equation of second order (3.1), where t is the time, $x(t)$ the input-, $y(t)$ the output variables, α_i and β_i are constants.

$$y''(t) + \alpha_1 y'(t) + \alpha_0 y(t) = \beta_0 x(t) \tag{3.1}$$

$$s = \sigma + j\omega \qquad s^2 Y(s) + \alpha_1 s Y(s) + \alpha_0 Y(s) = \beta_0 X(s) \tag{3.2}$$

$$H(s) = \frac{Y(s)}{X(s)} \qquad H(s) = \frac{\beta_0}{s^2 + \alpha_1 s + \alpha_0} \tag{3.3}$$

With the help of the Laplace transformation and by excluding the boundary condition, the equation (3.1) can be transformed into the s-domain (3.2), where s is a complex frequency domain parameter, σ and ω are real numbers. By rearrangement, (3.3) shows the transfer function of a resonant operating system, where $X(s)$ and $Y(s)$ are the Laplace transforms of the input and the output.

3.1.2 The quality factor (Q-factor) of resonantly operated MEMS cantilevers

The general findings in (3.3) are applied to the resonant operation of MEMS cantilevers, where the coefficients α_1 and α_0 are replaced by a resonance angular frequency ω_0 and Q by the damping coefficient γ. The coefficient γ can be expressed by ω_0 and the damping ratio ζ. ζ is inverse proportional to the quality factor Q (3.4). By replacing α_1 and α_0 in (3.3) with the variables introduced in (3.4), the transfer-function of a damped harmonic oscillator can be rewritten to (3.5) [26, 34, 43, 44].

$$\alpha_0 = \omega_0^2 \qquad\qquad \alpha_1 = 2\gamma$$

$$\gamma = \omega_0 \zeta \tag{3.4}$$

$$\zeta = \frac{1}{2Q}$$

$$H(s) = \frac{\beta_0}{s^2 + 2\gamma s + \omega_0^2} = \frac{\beta_0}{s^2 + \frac{\omega_0}{Q}s + \omega_0^2} \tag{3.5}$$

To determine the damping of the oscillation of a harmonic oscillator, the solution of the characteristic equation (3.6) results in (3.7). The equations (3.8), (3.9) and (3.10) [121, 138, 139] show the oscillation conditions, which depend on the damping coefficient γ.

$$s^2 + 2\gamma s + \omega_0^2 = 0 \tag{3.6}$$

$$s_{1,2} = -\gamma \pm \sqrt{\gamma^2 - \omega_0^2} \tag{3.7}$$

Oscillation occur
$$\gamma^2 - \omega_0^2 = \frac{1}{(2Q)^2} - 1 > 0 \rightarrow$$
$$\gamma > \omega_0 \rightarrow Q > 0.5 \tag{3.8}$$

Critical damping
$$\gamma = \omega_0 \rightarrow Q = 0.5 \tag{3.9}$$

Unable to oscillate
$$\gamma < \omega_0 \rightarrow Q < 0.5 \tag{3.10}$$

3.1.3 Determining the Q-factor of resonantly operated MEMS cantilevers

Determining the Q-factor with energy loss method

Beside the analytical determination, the physical interpretation of the Q-factor specifies the energy loss per oscillation cycle (3.11). The division of the resonance frequency f_0 by the bandwidth B, f_H being the upper and f_L the lower -3 dB (0.707) frequency of the oscillation amplitude, determines the Q-factor (3.12). When analysing an oscillating system in more detail, multiple i individual Q_i-factors can be associated with different energy loss mechanisms, so that the overall Q-factor of an oscillating system can be expressed by summing up these single Q-factors according to (3.13).

$$Q = 2\pi \frac{\text{stored energy}}{\text{dissipated energy}} = 2\pi \frac{E_{kin}}{E_{loss}} \tag{3.11}$$

$$Q = \frac{f_0}{B}$$
$$B = f_H - f_L \tag{3.12}$$

$$\frac{1}{Q} = \frac{1}{Q_1} + \frac{1}{Q_2} + \frac{1}{Q_3} + \frac{1}{Q_4} + \cdots = \sum_i \frac{1}{Q_i} \tag{3.13}$$

Determining the Q-factor with the Butterworth-Van Dyke model

Besides the -3dB approach to determine the Q-factor, this important device parameter can be calculated with the Butterworth-Van Dyke model, where the electrical output characteristics of MEMS resonators are analysed with an equivalent RLC circuit. Thereby the dynamic properties of resonantly operated cantilevers are covered (Fig. 3.1). The parallel capacity C_P defines the parasitic losses of the disk capacity of the AlN layer, and the parallel resistance R_P is dominated by that of the AlN layer. The series resonant circuit of R, L and C represents the mechanical resonance of the cantilever. The analogy between the mechanical and electrical description and the coupling through the piezoelectric MEMS justify their exchangeable applicability.
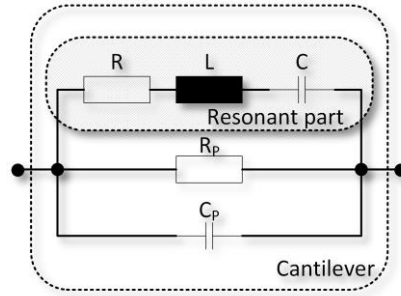
Fig. 3.1: Butterworth-Van-Dyke equivalent circuit of a cantilever operated in resonance.

First, the impedance spectrum determines in resonance the electrical values (C_P, R_P, R, L and C) of the piezoelectric layer. Then, these measured values are fitted with the model parameters. In the left part of (3.14) the impedance of the resonant part is expressed, whereas on the right side, the formula is separated into a real and an imaginary part. Equation (3.15) represents the inverse expression of the impedance, the admittance of the resonance- and the parasitic-part. A rearrangement of the admittance (3.16), leads to (3.17) [140], where the real- and imaginary-part of the admittance is denoted.

$$\underline{Z} = R + j\omega L + \frac{1}{j\omega C} = R + j\left(\frac{\omega^2 LC - 1}{\omega C}\right) \tag{3.14}$$

$$\underline{Y_m} = \frac{\omega C}{\omega CR + j(\omega^2 LC - 1)} \tag{3.15}$$

$$\underline{Y_C} = j\omega C_P \text{ and } \underline{Y_R} = \frac{1}{R_P}$$

$$\underline{Y} = \underline{Y_m} + \underline{Y_C} + \underline{Y_R} \rightarrow \underline{Y}(\omega) = G(\omega) + jB(\omega) \tag{3.16}$$

$$G(\omega) = \frac{1}{R_P} + \frac{\omega^2 C^2 R}{\omega^4 C^2 L^2 + \omega^2(C^2 R^2 - 2CL) + 1} \tag{3.17}$$

$$B(\omega) = \omega C_P + \frac{\omega C(\omega^2 CL - 1)}{\omega^4 C^2 L^2 + \omega^2(C^2 R^2 - 2CL) + 1}$$

The reformulation of (3.17) and the coefficient comparison with (3.5) finally results in the resonance frequency (3.18). The Q-factor (3.19) can be deduced by the same method [26, 34, 43, 44].

$$f_0 = f_{max(G(f))} = \frac{1}{2\pi\sqrt{LC}} \qquad (3.18)$$

$$Q = \frac{1}{R}\sqrt{\frac{L}{C}} \qquad (3.19)$$

Determining the Q-factor with the step response method

The Q-factor indicates how well the oscillation amplitude of an AFM-cantilever follows a surface step or any changes in surface topology. The change of the oscillation amplitude comprises the information of the reaction time and this in turn, relays on the Q-factor. Due to the analogy of mechanical and electrical oscillation description, the determination of the Q-factor can be either optically or electrically. Avoiding the complicated optical measurement path, the electrical measurement of the Q-factor through the piezoelectric layer is used to determine the Q-factor. An electrical readout circuit measures the voltage at the piezoelectric layer, which is placed on a cantilever. The envelope voltage U_E of the oscillation of a falling step function is defined by an exponential function, where the oscillation amplitude is U_0, the response time is τ and the angular frequency is ω (3.20). τ is defined by the time when the ratio $\frac{U_E}{U_0}$ reaches the value e^{-1}. After transforming the equation (3.20) an expression for the Q-factor (3.21) from a time-domain-step-response is found.

$$U_E = U_0 e^{-\frac{\omega}{2Q}\tau} \rightarrow \frac{U_E}{U_0} = e^{-\frac{\omega}{2Q}\tau} = e^{-1} \qquad (3.20)$$

$$Q = \pi f_0 \tau \qquad (3.21)$$

Determining the Q-factor with a Lorentz function

To determine the Q-factor with a Lorentz function, the impedance spectrum of a piezoelectric layer, placed on a cantilever, is approximated by a Lorentz function [50], as given below (3.22).

$$f(b, f) = \frac{b_1}{\sqrt{\left(1 - \left(\frac{f}{b_3}\right)^2\right)^2 + \left(\left(\frac{1}{b_2}\right)\left(\frac{f}{b_3}\right)\right)^2}} \qquad (3.22)$$

The approximation is done with a nonlinear fit (nlinfit, Matlab®), where f is the frequency, b_1 is the amplitude, b_2 is the Q-factor and b_3 is the resonance frequency.

3.2   Simulation input parameters

With the finite element simulation software tool COMSOL®, the oscillation amplitudes of the resonant operated cantilevers are determined. In the following chapter the description of the cantilever layout, the used materials, the physics, the boundary condition and the resulting simulation mesh are shown. In addition, the impact of the electrically stimulated AlN layer on the cantilever oscillation amplitude is discussed below.

3.2.1   Layout

In Fig. 3.2 the layout of the simulated cantilever is schematically shown. The beam consists of highly doped silicon as bottom electrode with a various length of l_{Si}, of a piezoelectric AlN layer with a various length of l_{AlN} and finally of a conductive gold (Au) layer as top electrode which has the same length as

l_{AlN}. The Si basis cantilever has a thickness of h_{Si}, the AlN layer has a thickness of h_{AlN} and the Au top electrode has a thickness of h_{Au}.
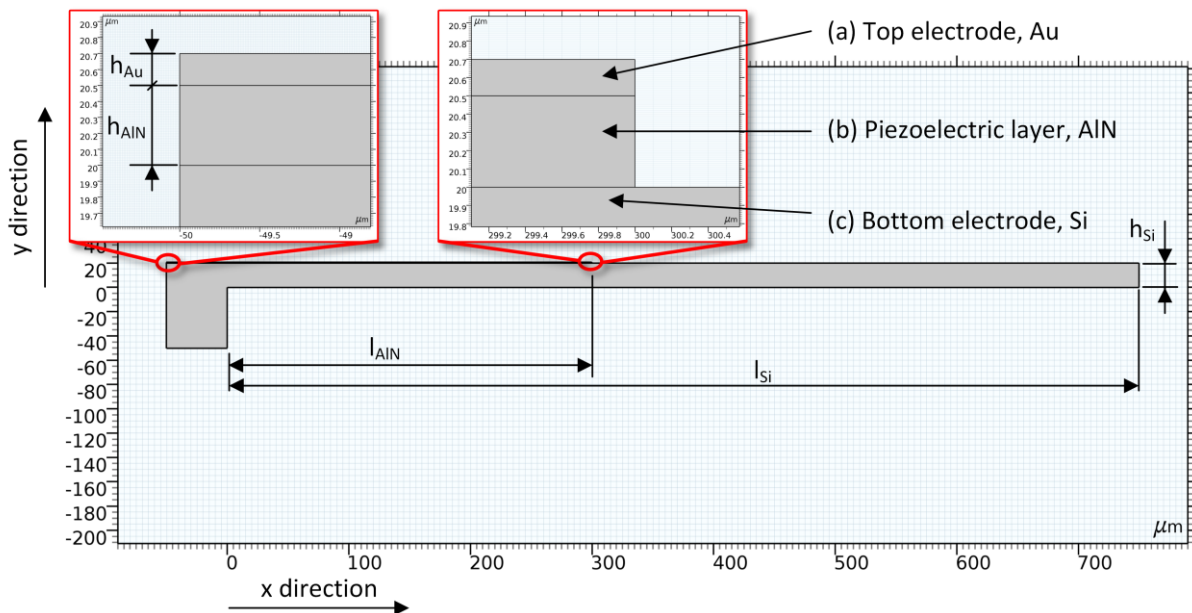
Fig. 3.2: The schematic shows the dimensions of the simulated cantilevers consisting of different layers in cross-sectional view. The length of the cantilever l_{Si} and the length of AlN l_{AlN} are marked in the drawing and the cut-outs show the material stack with the corresponding thicknesses.

3.2.2 Materials

The simulations use the included material bibliotheca of COMSOL®, which provides the individual material properties. Additionally, to the internal material database of COMSOL®, the noted parameters at Tab. 3.1 are added.

Label	Value [dim]	Description
f_start	40[kHz]	Start frequency
f_stop	60[kHz]	Stop frequency
f_step	1[Hz]	Frequency step
l_{Si}	750[um]	Cantilever length
h_{Si}	20[µm]	Cantilever thickness
w_{Si}	80[µm]	Cantilever width
l_{AlN}	50[um]	AlN layer length
h_{AlN}	500[nm]	AlN height
h_{Au}	250[nm]	Top electrode thickness
shkrL	50[µm]	Bulk Si length
T	293.15[K]	Ambient temperature
Vin	10[V]	AlN supply voltage
v0	10[nm]	Shaker displacement amplitude
structural_loss_factor	2.08E-04	Loss factor
cond_Si	200[mS/m]	Si conductivity
cond_AlN	1.5915[pS/m]	AlN conductivity
Rpassive	1e6[ohm]	Electric circuit resistance
Qcontrol_phase	0	Phase shift of electrical circuit

Tab. 3.1: COMSOL® parameter table for cantilever simulation.

The energy losses within the material are summarized in the "structural_loss_factor", which summarizes the thermoelastic damping Q_{TED} (3.23), the clamping losses Q_{clamp} (3.24) and the surface losses $Q_{surface}$ (3.25) to one parameter. In (3.23), the C_p is the specific heat capacity, E is the beam modulus of elasticity, α is the linear thermal expansion coefficient, T_o is the equilibrium temperature, κ_{th} is the thermal conductivity and h_{Si} is the thickness of the beam. Additionally, in (3.24) l_{Si} is the beam length, w_{Si} the beam width, and in (3.25) h_{Si} denotes the characterized thickness of the surface layer and E_{ds} is a constant, which is related to the surface-stress.

Thermoelastic damping [141], formula (7)

$$Q_{TED} = \frac{\rho_b C_p}{E \alpha^2 T_o} \frac{1 + (\omega_1 \tau_Z)^2}{\omega_1 \tau_Z}$$

$$\tau_Z = \frac{\rho_b C_p h_{Si}^2}{\pi^2 \kappa_{th}}$$

(3.23)

Clamping losses [142], formula (17)

$$Q_{clamp} = \frac{l_{Si}^5}{0.3 \cdot w_{Si} \cdot h_{Si}^4}$$

<div align="right">(3.24)</div>

Surface losses [143], formula (47) and onwards

$$Q_{surface} = \frac{w_{Si} \cdot h_{Si} \cdot E}{2 \cdot (w_{Si} + 3h_{Si}) \cdot h_{Si} \cdot E_{ds}}$$

<div align="right">(3.25)</div>

$h_{Si} \cdot E_{ds} = 0.81$ for a single crystalline silicon cantilever

3.2.3 Implementation of physical models

The implemented physical models and pre-defined nomenclature of COMSOL® are used. This is denoted in the text by the use of quotation marks.

Electrical circuit (cir)

The bottom- and the top electrode of the cantilever is connected to a simulated electrical circuit. The circuit is connected via the "External I vs. U" terminal with the AlN layer, which is connected to the top electrode. In chapter 3.3.2 (Predefined displacement as external excitation) a "Resistor" is connected to the top electrode where the cantilever is only excited mechanically. In chapter 3.3.3 (Electrical stimulation of piezoelectric MEMS cantilevers) a "Voltage Source" is selected to excite the oscillation. To simulate the Q-control in 3.3.4 (Q control, damping of resonant MEMS cantilevers) the active layer is driven and measured by a "Resistor Voltage source".

Electrostatics (es)

The electrostatic physics is applied to the AlN layer, which includes the "Charge Conservation, Piezoelectric" and the "Electric Displacement" $D = \varepsilon_0 \varepsilon_{rs} E + P_{AlN}$. ε_0 is the vacuum permittivity, ε_{rs} is the relative permittivity, E is the presence electric field and P the polarization density. The simulation of the AlN layer initially starts with 0 V as "Initial Values" of the "Electric potential" and with "Zero Charge" $n \cdot D = 0$ at all edges.

Electric currents (ec)

The "Current Conversion" based on $\nabla \cdot J = Q_{J,V}$ and transforming electrical charge to current density *J* applies to all three domains, namely the "Top electrode", the "AlN" and the "Bottom electrode". The domains have an "Initial Value" of the "Electric potential" of 0 V. The "Terminal" connects the "Top electrode" with the electrical circuit (cir) via a "Circuit" terminal type. The "Ground" of this terminal connects the "Bottom electrode" to a defined ground voltage level. All other edges of the cantilever are electrically insulated.

Solid mechanics (solid)

The mechanical "Damping" of oscillation of the cantilever is modelled as a "Linear Elastic Material", which applies to the "Top electrode" and "Bottom electrode" domain. In addition, the AlN layer is defined as "Piezoelectric Material" where the decay of the oscillation is attained with the "Mechanical Damping". The damping of all domains is described by an isotropic loss factor (called structural_loss_factor, Tab. 3.1). The edges are either "Fixed Constraint", or "Prescribed Displacement" (Fig. 3.3). All other edges are defined as free moving edges. The "Initial Values" of "Displacement field" is 0 m and the "Structural velocity field" is 0 m/s. This means that in the beginning of the simulation the entire structure stands still

Multiphysics-piezoelectric effect (pze1)

The Multiphysics-Piezoelectric effect enables and defines the coupling of "Solid Mechanics" and "Electrostatics".

3.2.4 Mesh

The finite element solving time of the MEMS cantilever is reduced by using a high local mesh resolution at the corners and a low mesh resolution in the residual areas, respectively. The mesh resolution setting for every domain is shown at Tab. 3.2.

Area	Calibrate for	Predefined element size	Type	Detail
(a) Top electrode	Semiconductor	Normal	Triangular	Distribution: Fixed numbers of elements: 5
(b) AlN	Semiconductor	Normal	Triangular	Distribution: Fixed numbers of elements: 5
(c) Si bulk	Semiconductor	Normal	Quad	

Tab. 3.2: Mesh element size settings for top electrode, AlN and Si bulk.

Fig. 3.3 shows the cantilever configuration with the corresponding generated meshing of the top electrode, the piezoelectric layer and the bottom electrode. The figure implies the location of the fixed constraint and the predefined displacement as external excitation input (called Mode 1).
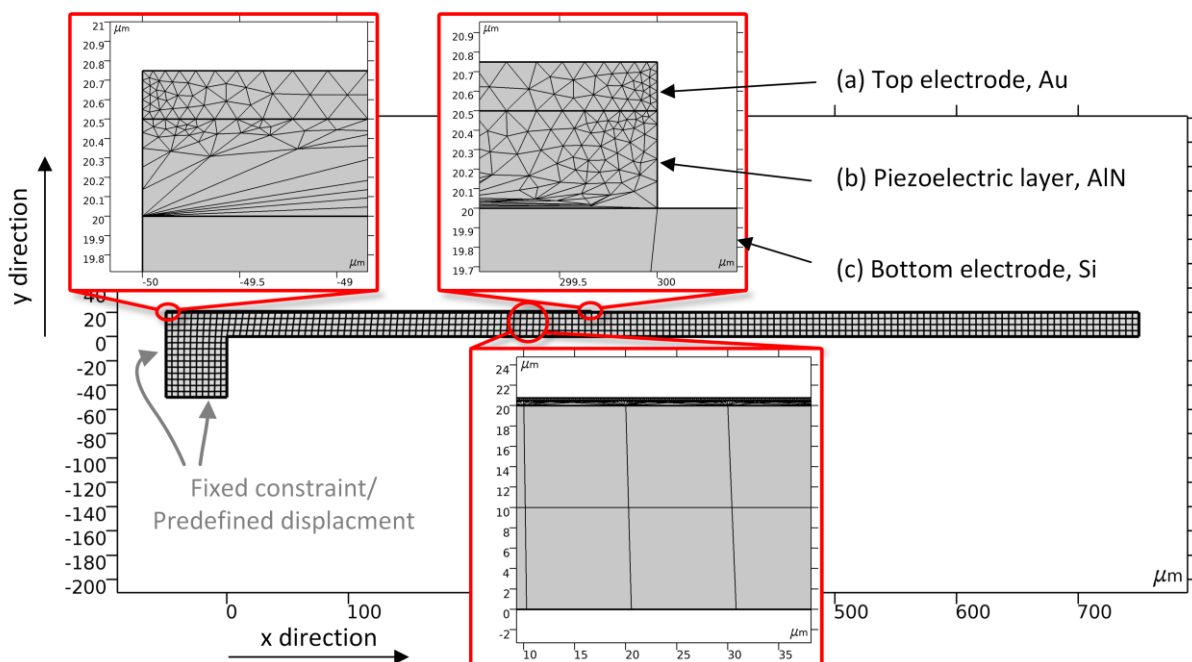
Fig. 3.3: The generated mesh at the cantilever, piezoelectric layer and top electrode.

3.3 Cantilever operation modes and results

The simulation of cantilever actuation is divided into three types of operation (3 Modes). To start, the Eigenfrequency analysis gives a straightforward overview of the resonance frequency spectrum. With this knowledge, the simulation of the operation modes is started. The first operation mode simulates an external shaker, which provides as an oscillation stimulation with a predefined displacement in y-direction (Mode 1). The cantilever oscillation is measured as a displacement at the free moving end of

the cantilever. The second operation mode uses an external, oscillating voltage source for the stimulation of the piezoelectric layer (Mode 2). Consequently, the third operation mode, which is the combination of both operation modes mentioned before, allows the manipulation of the basic cantilever oscillation amplitude by the integrated AlN transducer element (Mode 3).

3.3.1 Eigenfrequency of resonant operating MEMS cantilevers

The Eigenfrequency solution gives a detailed information of the resonance frequency spectrum depending on the cantilever length, cantilever thickness and piezoelectric layer length. To verify the simulation results, the reshaped Euler-Bernoulli beam equation (3.26), with $\lambda_1 = 1.87510$ for the first resonance frequency, the material constant Young's modulus $\varepsilon_C = 170\,\text{GPa}$ and density $\rho_C = 2.3 \cdot 10^3 \frac{\text{kg}}{\text{m}^3}$ of silicon, is used to compare the calculated resonance frequencies with those gained from FEM simulations (see Tab. 3.3).

$$f_R = \lambda_1^2 \frac{h_{Si}}{l_{Si}^2} \frac{\sqrt{\frac{\varepsilon_C}{\rho_C}}}{2\pi}$$

(3.26)

For reasons of simplicity, the AlN layer was neglected within the analytical calculations. The comparison of both approaches shows a derivation of lower than 5%. This confirms the accuracy of the FEM simulation results.

l_{Si} Cantilever length [µm]	Calculated resonance frequency [kHz]	Simulated resonance frequency [kHz]			
		0 µm	50 µm	100 µm	200 µm
500	110.4	105.69	108.24	110.24	112.57
750	49.1	47.70	48.51	49.23	50.28
1000	27.6	27.03	27.39	27.71	28.25

Tab. 3.3: Comparison of the simulation results and the analytic calculation of cantilever resonance frequency and the influence of the piezoelectric layer length to resonance frequency with a Si device thickness of 20 µm.

To meet the maximum frequency of the electrical circuit, namely the amplifiers and the connection cables, the limit is set to the maximum frequency of 120 kHz.

3.3.2 Predefined displacement as external excitation (Mode 1)

When knowing a given resonance frequency, the influence of a layer on the Si cantilever is examined in a next step. Therefore, a mechanical excitation induces a displacement at the marked edges in Fig. 3.3. It acts like a piezoelectric actuator and induces a so-called "Predefined Displacement" of 10 nm in y-direction. For simplicity reason, this operation is called Mode 1. The considered frequency spectrum ranges from 26 kHz to 113 kHz, where the simulations show the resonance of the cantilevers with a length of 500 µm, 750 µm and 1000 µm. The maximum amplitude of the tip is shown in Fig. 3.4.
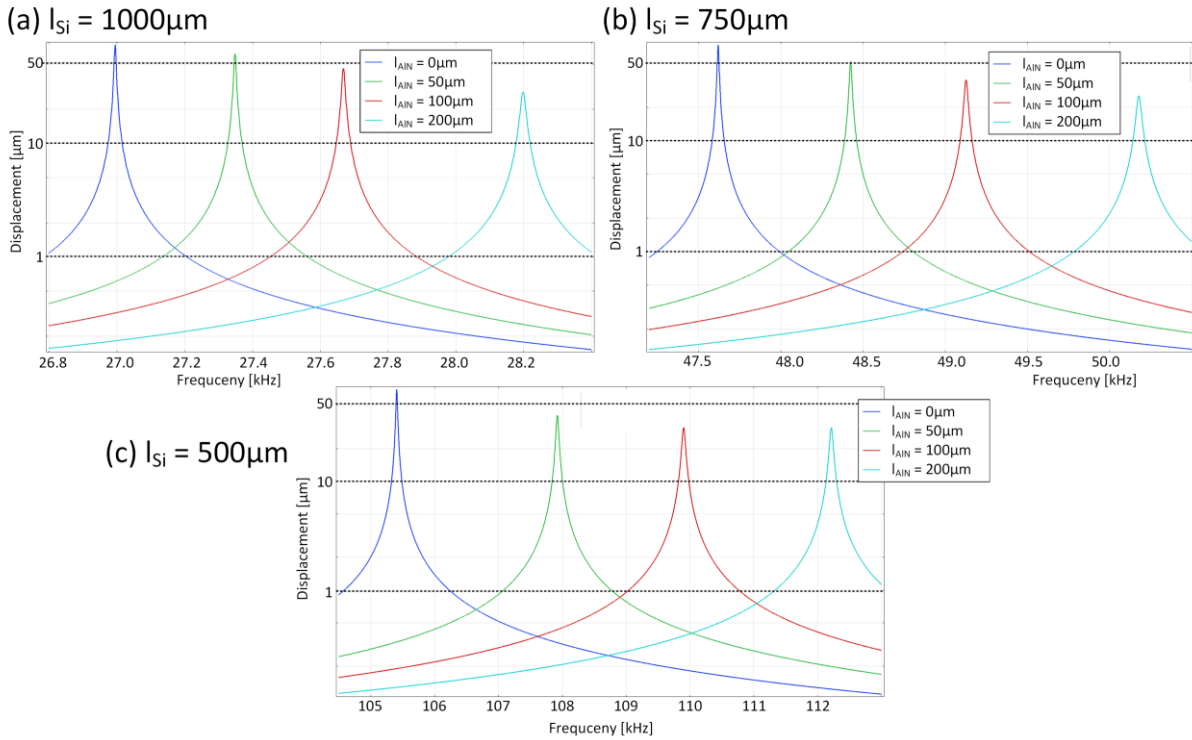
Fig. 3.4. Frequency spectrum of cantilever deflection resulting from a pre-defined shaker displacement for different cantilever lengths of (a) 1000 µm, (b) 750 µm and (c) 500 µm as a function of the AlN layer length l_{AlN}.

When investigating the results in Fig. 3.4 (a-c), the cantilever displacement spectra show a minor influence of the length of the deposited layer and electrode. Only the cantilever without the AlN layer attracts attention due to the larger oscillation amplitude. This can be explained by the mode shape of the first resonance frequency, where the surface stress is evenly distributed along the cantilever axis.

3.3.3   Electrical stimulation of piezoelectric MEMS cantilevers (Mode 2)

Another possibility to stimulate in a piezoelectric cantilever a mechanical oscillation is to supply an electrical stimulus to the top and bottom electrode, here it is called Mode 2. The electrical stimulation results in cantilever deflection values dependent on the frequency, as shown in (Fig. 3.5).
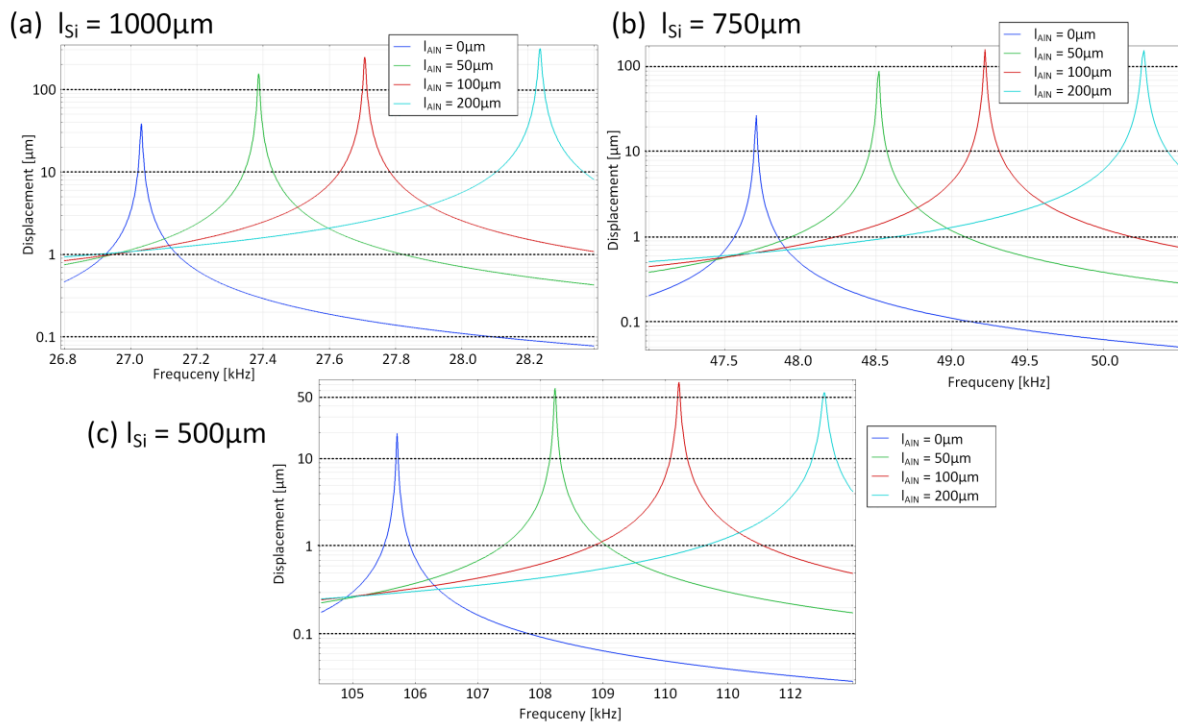
Fig. 3.5: Frequency spectrum of cantilever deflection of AlN actuation with a supply circuit for a cantilever length of (a) 1000 µm, (b) 750 µm and (c) 500 µm.

When comparing the figures of Fig. 3.4(a-c) with Fig. 3.5(a-c), the best trade-off between the amplitude at resonance, which has to be as low as possible and the impact of the electrical stimulation, which has to be as high as possible, is at l_{AlN} from 50 µm to 100 µm. In order to minimise the parasitic effects of the AlN layer, the area of the AlN layer has to be kept as small as possible, therefore a l_{AlN} of 50 µm is chosen. In addition, the small surface area prevents large charging and discharging currents in the electrodes due to the excitation voltage. Remarkably, the data show that an oscillation amplitude is also generated with a piezoelectric length of 0 µm at the beam. But nevertheless, the remaining piezoelectric layer (x < 0) at the bulk Si in Fig. 3.2 deforms the bulk Si which stimulates the cantilever oscillation.

3.3.4 Q control, damping of resonant MEMS cantilevers (Mode 3)

The superposition of two actuators is used to adjust the oscillation amplitude of the cantilever. The first actuator is the piezo shaker, which introduces the basic mechanical oscillation, here it is called Mode 3. In the model, the shaker introduces its oscillation via the edges which are marked as "predefined displacement" (Fig. 3.3). This primary oscillation constructively or destructively interferes with the oscillation, which is introduced by the piezoelectric AlN layer integrated on the cantilever. The stimulation amplitude of the shaker and voltage supply will be kept constant over the entire frequency range. The phase displacement between shaker and piezoelectric actuation will trigger the damping or amplification of the cantilever oscillation amplitude, respectively. The simulation results are presented in Fig. 3.6.
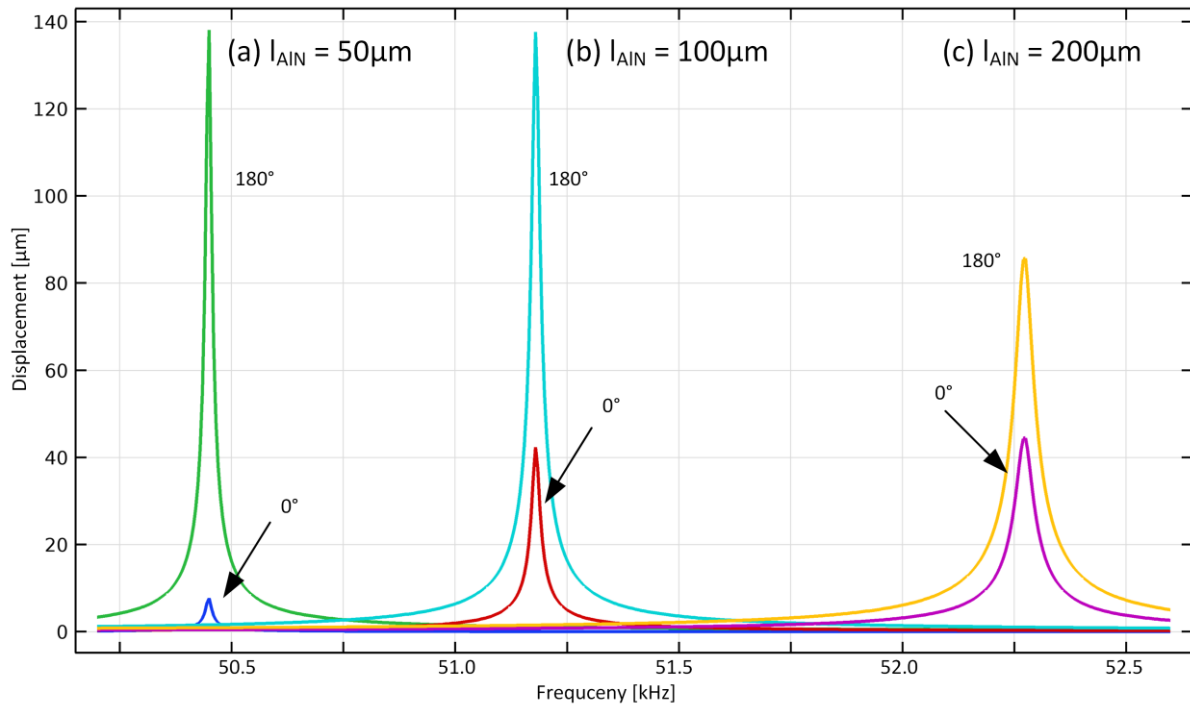
Fig. 3.6: The deflection frequency spectrum of a 750 μm cantilever shows the superposition of shaker displacement and of AlN actuation. The stimulation signals have a phase range from -180 ° to 0 °. (a) The detail view of the cantilever deflection with an AlN length of 50 μm. (b) The detail view of the cantilever deflection with an AlN length of 100 μm. (c) The detail view of the cantilever deflection with an AlN length of 200 μm.

When comparing the frequency range of (a) to (c), the resonance curve becomes wider. This can be explained by the varying stiffness applied by the different materials. The longer the integrated piezoelectric layer including the metallic top electrode, the broader the resonance spectrum gets. Focusing on the shape of the resonance spectrum, the width of the resonance peak increases when the phase is changed from -180 ° to 0 °. The drop in amplitude is attributed to the impedance behaviour of the piezoelectric material. The larger impedance of piezoelectric layer reduces the current flow and in parallel decreases the effect on the excited oscillation, respectively.

The Q-factor is used to estimate the decrease in oscillation amplitude. For this purpose, a Lorentz function [50] is fitted to the impedance spectrum using Matlab®. The Q-factor obtained from this procedure is displayed in Tab. 3.4 for the different lengths of the piezoelectric layers.

Phase	Q-factor (l_{AlN} = 50 μm)	Q-factor (l_{AlN} = 100 μm)	Q-factor (l_{AlN} = 200 μm)
- 180 °	4242	3061	1360
0 °	4242	3061	1360

Tab. 3.4: The overview of the Q-factor manipulation by phase shifting from -180 ° to 0 ° on the cantilever deflection.

It can be seen in Tab. 3.4 that the reduction of the oscillation amplitude does not necessarily manipulate or reduce the Q-factor. A constant phase reduces the deflection through the frequency spectrum but it has no effect on the Q-factor. To manipulate the Q-factor, the phase has to be adjusted with frequency, which will be verified at the "Results" chapter with a shaker and cantilever measurement set-up.

3.4   Summary

The comparison between the resonance frequencies obtained by FEM simulations and by analytical solutions show minor deviations. It has been demonstrated that the geometrical dimension of the active actuated piezoelectric layer cannot be neglected and must be considered for the cantilever

layout. Therefore, the total area of the piezoelectric AlN layer needs to be chosen carefully to prevent excessive parasitic capacitance and resistance effects. It has been shown that the superposition between shaker actuated and AlN layer actuated oscillation can have constructive or destructive character.

4 Aluminium nitride (AlN) characterisation

Parts of this chapter have already been published in [144, 145]

The warping of a wafer during thin film deposition results in a variation of the thermal coupling between wafer and sample holder, thus leading to a variance of film properties in different deposition runs. To prevent the warping of the wafer during the AlN deposition process, a clamped wafer holder is introduced. It provides a constant thermal contact between the wafer and the wafer holder enabling reproducible thermal conditions during deposition. As a consequence, a substantially higher reproducibility in mechanical and electrical AlN film properties is demonstrated in contrast when using a standard sample holder.

4.1 Design of experiment (DOE) parameters

To start, a DOE, which is shown in Tab. 4.1, is carried out to evaluate the impact of the clamped sample holder on the mechanical (film stress σ), microstructural (etch residuals area $\bar{\bar{A}}_{>0.95}$, X-ray diffraction) and electrical (piezoelectricity d_{33}, leakage current density J) properties of the AlN layers. Every week, a new set of samples with AlN thickness values of 0.5 μm, 1.0 μm and 2.0 μm is fabricated. This series of experiments are performed over the course of five weeks and the results are compared with sample number 6, which uses the standard holder allowing the wafer to move completely free during deposition. Deposition parameters like ISE power P_{ISE} and time t_{ISE}, deposition power P_{AlN} and target-sample distance are kept constant. The different thickness values of the layers h_{AlN} are achieved by adapting the deposition time t_{AlN}.

Set	P_{ISE} [W]	t_{ISE} [s]	h_{AlN} [nm]	P_{AlN} [W]	t_{AlN} [min]
1, 2, 3, 4, 5	500	300	500	800	18
6 (Mo holder)	500	300	500	800	18
1, 2, 3, 4, 5	500	300	1000	800	37
1, 2, 3, 4, 5	500	300	2000	800	74
6 (Mo holder)	500	300	2000	800	74

Tab. 4.1: Design of experiments (DOE) for the clamped sample holder experiments with dependence on fabrication week/lot number and AlN layer thickness. The AlN deposition labelled as set 6 is used to compare the clamped holder with the standard holder. For this purpose, only the thickest and thinnest layers were considered.

4.2 Clamped substrate holder

The development of the clamped sample holder considers the thermal heat flow between sample and sample holder. Next, the thermal expansion of the wafer material and the sample holder is addressed.

4.2.1 Thermal considerations

For this work, the AlN thin films are deposited with an industry-type DC magnetron sputter equipment (VonArdenne LS730S). Typically, the samples are placed on a molybdenum (Mo) plate, which then is placed on a rotary table inside the deposition vacuum chamber. The relevant thermal resistance fractions are noted in Fig. 4.1. When changing the type and the material of the substrate holder, improvements in the thermal resistance between substrate and substrate holder as well as between the substrate holder and the sputter deposition chamber are expected.
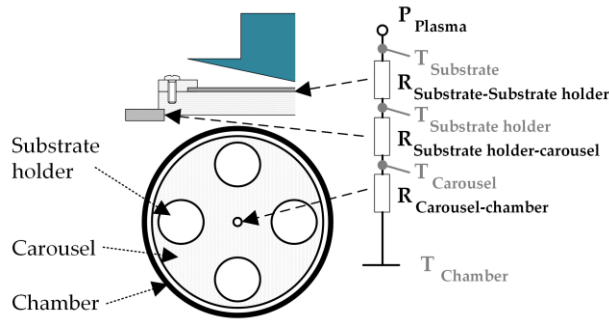
Fig. 4.1: Schematics indicating the most dominant thermal resistance values of the thermal path from the substrate to the chamber, which is acting as heat sink.

While the AlN layer is deposited, the particle bombardment continuously heats up the wafer. Therefore, the difference between the thermal expansion coefficients of silicon Si (α_{Si} = 7.6 ppm/K [146]) and the deposited AlN (α_{AlN} = 4.1 ppm/K [147]) deforms the wafer as indicated in Fig. 4.2 (a). During film growth, the difference in thermal expansion of Si and AlN and the intrinsic stress of AlN originating from *e.g.* the altering crystal boundaries [148] leads to the reduction of the biaxial stress. The value changes from compressive (negative values) to tensile stress (positive values) [149], which is reflected in the change of the wafer curvature from convex to concave bending, as schematically illustrated in Fig. 4.2 (a).
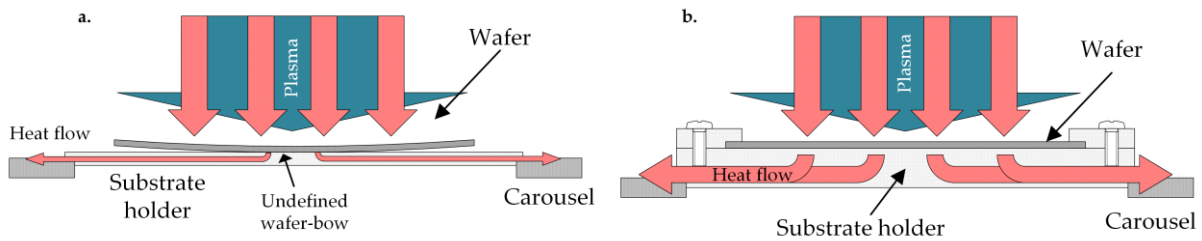
Fig. 4.2: (a) Schematic visualisation of the heat flow at the standard Mo substrate holder. The image shows a reduced heat flow due to wafer bending during deposition. For simplicity reasons, only the situation with a convex bending is depicted. But also concave bending may occur during a deposition process resulting also in a high thermal resistance to the wafer holder. (b) To reduce the latter parameter, a clamping substrate holder, which is made out of Al is used, to minimize the effect of wafer bending.

Consequently, the thermal contact resistance of the wafer to the substrate holder varies with deposition time because the wafer bow inhibits the heat flow. This results in temperature variations on the wafer surface. Furthermore, reactive sputter depositions strongly depend on temperature profile [150, 151], which has to be held constant to minimize the variation of layer stress across different deposition runs. The change of the sample holder material from Mo with a thermal conductivity of λ_{Mo} = 142 $\frac{W}{m \cdot K}$ [146] to aluminium (Al) with λ_{Al} = 247 $\frac{W}{m \cdot K}$ [146] helps to increase the heat transport. The thermal heat flow I of a material can be calculated, according to Fourier's law (4.1)

$$I = \frac{A \cdot \lambda \cdot \Delta T}{l} ; \frac{I_{Al}}{I_{Mo}} = \frac{\lambda_{Al}}{\lambda_{Mo}} \qquad (4.1)$$

where A represents the area of a solid sample, l the sample length, ΔT the temperature difference and λ the thermal conductivity, respectively. When the geometrical dimensions can be regarded as identical, the thermal conductivity of aluminium λ_{Al} is about 1.7 times higher than Molybdenum λ_{Mo} which allows a greater heat flow just by changing the material of the substrate holder.

In addition, clamping the wafer, as shown in Fig. 4.2 (b), helps to reduce the thermal resistance between substrate and substrate holder.

4.2.2   Mechanical considerations

A high degree in c-axis orientation of the AlN thin films quality can be archived by a clamping fixture for 4" wafers. The tailored wafer holder comprises a high heat dissipation and a homogeneous force distribution. Apart from easy handling, the suitability for high vacuum processing, high thermal stability for long-term usage as well as reusability are required. The wafer as well as the holder is heated up by the deposition process and both undergo thermally induced expansion. Any buckling of the wafer is prevented by the three times lower thermal expansion coefficient of the clamped Si wafer (α_{Si} = 7.6 ppm/K [146]) in comparison to the clamping fixture which is made of aluminium (Al) (α_{Al} = 23.1 ppm/K [146]). Therefore, an Al clamping disk is tightened with four diagonal placed screws (torque of 4 Nm) to an Al base plate to ensure a homogeneous surface pressure at the wafer edges (see Fig. 4.3 (b, c)).
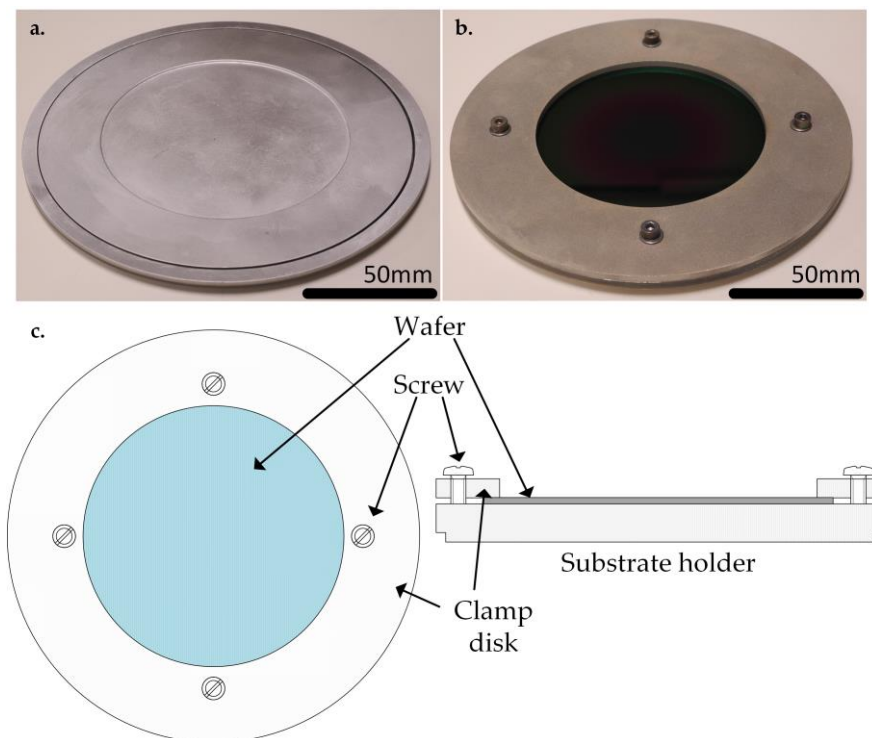
Fig. 4.3: Standard sample holder (a) and tailored substrate holder (b). The sample holder for clamping the wafer consists of a base plate (Al), a clamping disk (Al) and fixing screws made of stainless steel (c).

4.3   Characterisation of the AlN layers

4.3.1   Sample holder temperature *vs.* layer stress

The measured peak temperature T_m during AlN depositions for different layer thicknesses at various time points with the clamped substrate holder is shown in Fig. 4.4 (a). The temperature during deposition of 0.5 µm AlN thin films always remains below the lower measurement limit of the pyrometer being at 100 °C. The T_m of 1.0 µm thin AlN increases up to 135 °C due to an extended deposition time. Finally, the temperature measurements of the layers with 2.0 µm AlN thickness do not exceed a substrate temperature of 144 °C. The compressive stress is in the range from -8.8 MPa to -110 MPa (2.0 µm), from -190 MPa to -325 MPa (1.0 µm) and from -301 MPa to -520 MPa (0.5 µm), as illustrated in Fig. 4.4 (b). A higher deposition temperature (of 160 °C) modifies the film stress in such a way, that cracking of the film can occur, which can be seen for the 2.0 µm AlN thin film of week 1. The depositions with a Mo substrate holder reveal substantially higher T_m and σ values in contrast to depositions with the clamped substrate hold. Later, the results are compared in the respective context.

a.

b.
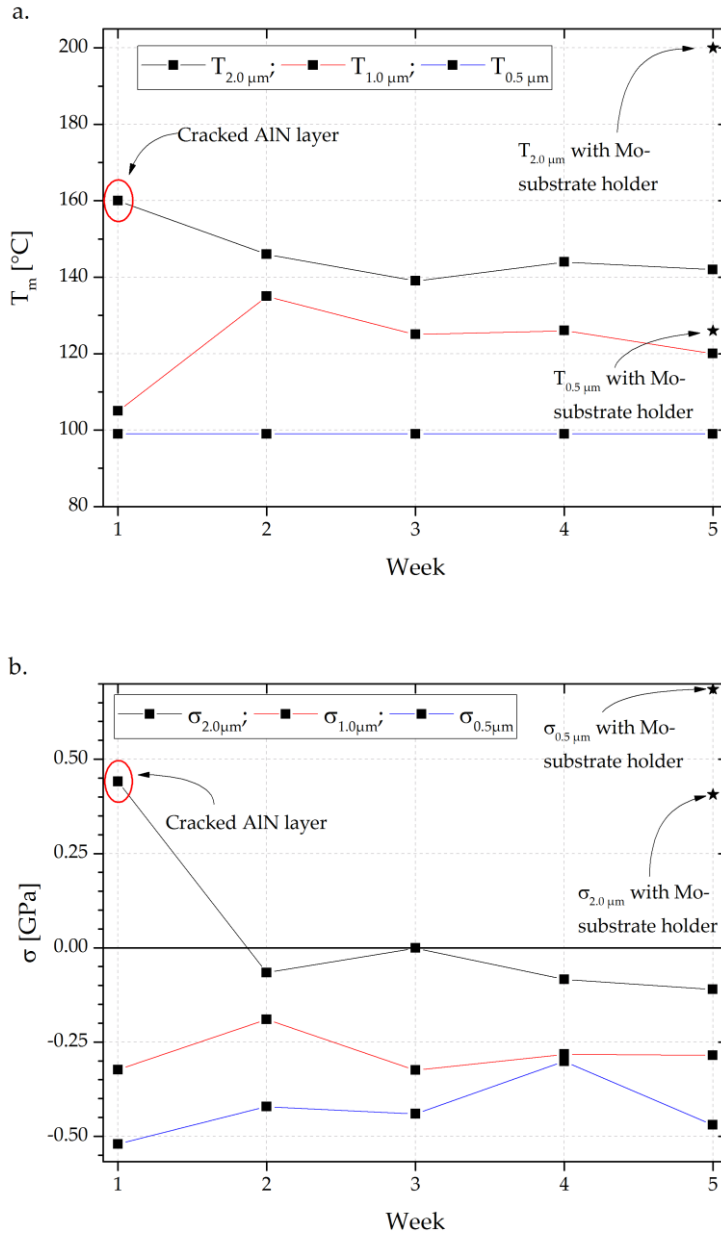
Fig. 4.4: (a) Maximum temperature T_m and (b) layer stress σ of deposited AlN layers with clamped sample holder synthesized in week 1 to 5. The maximum temperature represents the highest process value during deposition. The inserted straight lines serve as guide to the eye.

4.3.2   Wet-chemical etching

The etching process and parameters are described in the chapter "Methods and Instrumentation". In Fig. 4.5, the SEM images (etching time from 20 s to 375 s) are overlaid with a post-processed mask. The original picture is shown on left-hand side of each micrograph, whereas on the right half the detected residues are enclosed by green borders. Through an optical quantification method, the thresholding is varied in case of differing brightness of the images.
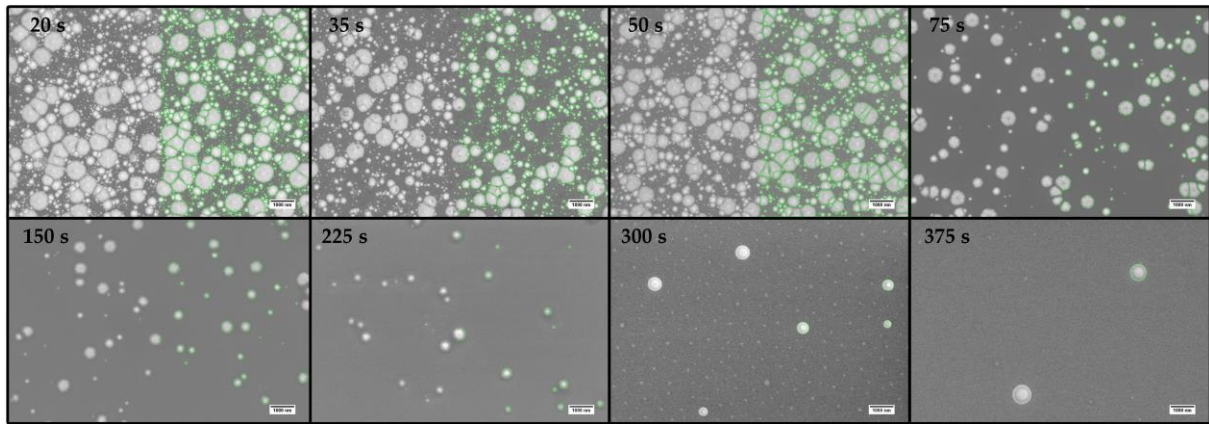
Fig. 4.5: Each image represents the residue distribution of the 0.5µm AlN film deposition on silicon after wet-chemical etching for 20 s to 375 s. At the left area, the micrograph of the original SEM image is shown, whereas at the right half the modified analysis image is inserted.

The apparent reason to investigate the etching performance are the large residues, which have low count. For this, the parameter A_I is introduced representing the total area of residues having a specific size. The quantity of residues of each interval N_I is then multiplied by the centre value of interval A_C to the total of residues of each interval $A_I = A_C \cdot N_I$. The evaluation of the sample after an etching time of 50 s shows in the diagram that a large total area is covered by the small residues, whereas a uniform distribution results for larger residues. The average of largest 5% of residues is specified as the significant area called $\overline{A}_{>0.95} = \overline{\sum_{0.95}^{1} A_I}$. In Fig. 4.6, exemplarily histograms of the area distribution of residues for week 3 samples with 0.5 µm AlN thickness are shown. The etching time ranges from 20 to 375 s and in every histogram the considered area of 0 to 0.500 µm² is divided into 40 intervals. For example, the histogram for 50 s has an average total area $\overline{A}_{>0.95}$ of 1.217 µm².
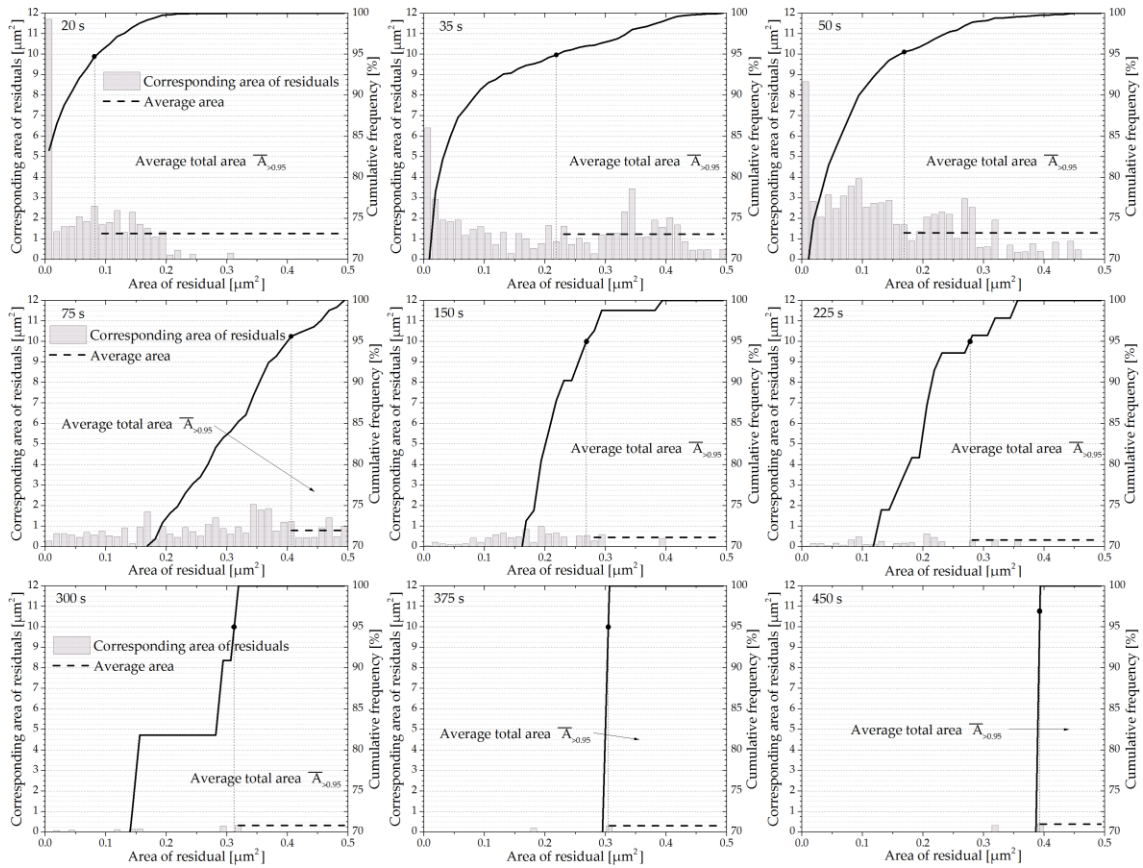
Fig. 4.6: The histograms of residues area distribution for sample week 3 with 0.5 µm AlN thickness for the etching time of 20 s, 35 s, 50 s, 75 s, 150 s, 225 s, 300 s, 375 s and 450 s are shown. The centre of each interval is multiplied with the number of residues at each interval. Significant for one sample measurement is the average of the largest 5% residues area which is defined as the average total area $\overline{A}_{>0.95}$

To plot the remaining residue area $\overline{A}_{>0.95}$ after the wet chemical etching, the value after each etching time and of week 1 to week 5 are summarized in a boxplot. All results for the thicknesses of 0.5 µm, 1.0 µm and 2.0 µm are plotted in Fig. 4.7.
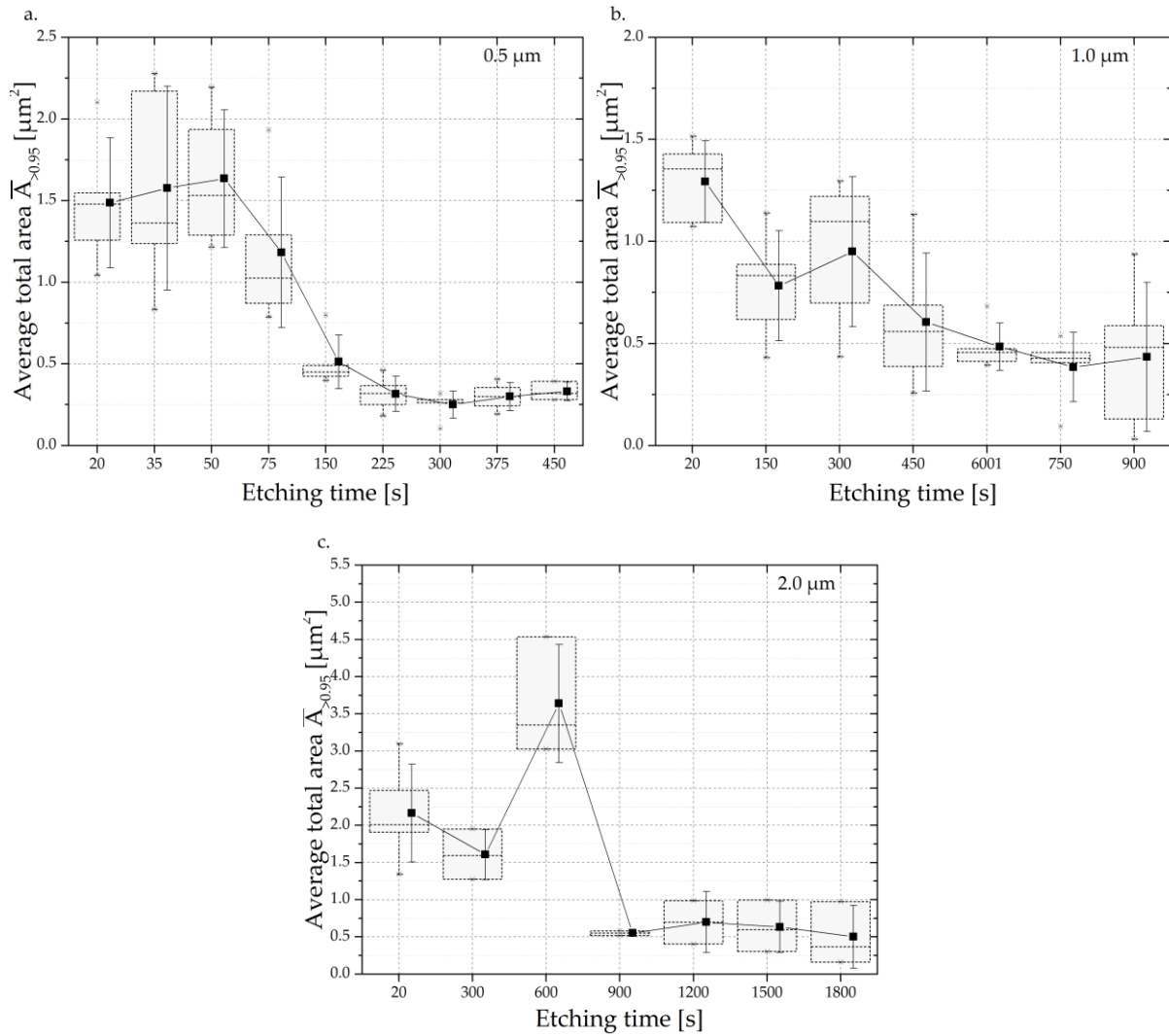
Fig. 4.7: The boxplot shows the total area $\bar{\bar{A}}_{>0.95}$ determined from the etching results of 0.5 µm, 1.0 µm and 2.0 µm AlN thin film samples. At each etching time the boxplot represents week 1 to week 5 values. At 0.5 µm (a) the average values increase to an etching time of 50 sec. At the end it drops to a value of 0.369 µm². At a thickness of 1.0 µm AlN (b) the average value drops from the beginning with a minor peak at 300 sec down to 0.433 µm². (c) It represents the etching result of 2.0 µm AlN layer. The average value decreases constantly, and it is only interrupted by a significant increase at 600 sec etch time. However, the final average size after 1800 sec etching is 0.433 µm².

For a better clarity, the average value $\bar{\bar{A}}_{>0.95}$ and its standard derivation are introduced, which include $\bar{A}_{>0.95}$ of week 1 to week 5. The results of the samples (see Fig. 4.7 (a)) with 0.5 µm thickness got additional etch times, 20 s, 35 s, 50 s and 75 s, to increase the time resolution. At 20 s the $\bar{\bar{A}}_{>0.95}$ is 1.483 µm² where most of the surface area is covered with large residues. After 50 s etching, $\bar{\bar{A}}_{>0.95}$ increases slightly to 1.634 µm² where the primarily small residues are dissolved and the larger residues are still present. After an etching time of 225 s to 420 s, the slow etching residues are reduced to 0.369 µm² and are not fully dissolved. As it can be seen in Fig. 4.7 (b) the average value $\bar{\bar{A}}_{>0.95}$ for the samples with 1.0 µm thickness drops from 1.290 µm² down to 0.433 µm² at 900 s. The etching results of the 2.0 µm samples are shown in Fig. 4.7 (c), where $\bar{\bar{A}}_{>0.95}$ drops from originally 1.834 µm² down to 0.6 µm² at 900 s. The peak of 4.406 µm² at 600 s results from the difference in etching speed between the slow and the etchable crystallographic planes in the AlN layer. Less dominant is this behaviour for the samples with 1.0 µm and 0.5 µm thicknesses. After 1800 s, $\bar{\bar{A}}_{>0.95}$ remains constant at 0.433 µm², which is similar to the etching results of AlN samples having a thickness of 0.5 µm and 1.0 µm, respectively. The etch results of the samples with 2.0 µm thickness which indicate a connection between etching behaviour and film stress, where only the layers with negative stress can be etched.

As illustrated in Fig. 4.4 (b), the samples from week 1 and week 3 show a positive or close to zero film stress, which results in small etching trenches at the AlN surface even when the sample is kept in the etchant solution up to the maximum etch time of 1800 s (see Fig. 4.8 (b), untreated surface Fig. 4.8 (a)). In a rough estimation, increasing the thickness by a factor of two, the etch process needs twice the time than before.
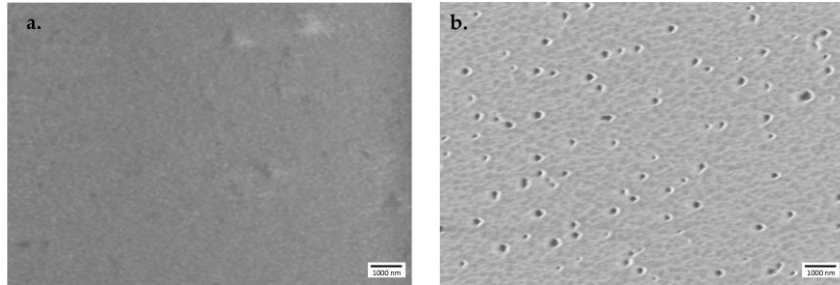
Fig. 4.8: (a) Image of a sputtered AlN surface. (b) Image of the surface of the week 3 AlN etched sample after 1800 s etching time.

4.3.3 X-ray diffraction (XRD)

With the use of the sputter deposition parameters, listed in the chapter 5.2 "Manufacture of MEMS cantilevers", a high degree of c-axis orientation of the deposited AlN layer is achieved. To compare the improvement of the deposition with the clamped sample holder to the conventional Mo substrate holder, the logarithmically scaled XRD diffraction patterns of 0.5 µm thin AlN layers samples from week 1 to 5 are presented in Fig. 4.9 (a). Here, an example of the analysis of the (002) related diffraction peak is given in Fig. 4.9 (b). Despite the straightforward Bragg-Brentano (BB) measurement, the exemplary analysis of the peak shows a difference in peak characteristics between the c-axis orientation of the Mo sample holder and the clamped sample holder of week 3. The peak amplitude is increased by almost a factor of two and the peak position is slightly shifted from 36.11° to 36.08°. The fitted peak of the full width half maximum (FWHM) is reduced from 0.29 to 0.23, which indicates an improvement of the c-axis orientation of the deposited AlN layer compared to the standard Mo substrate holder.
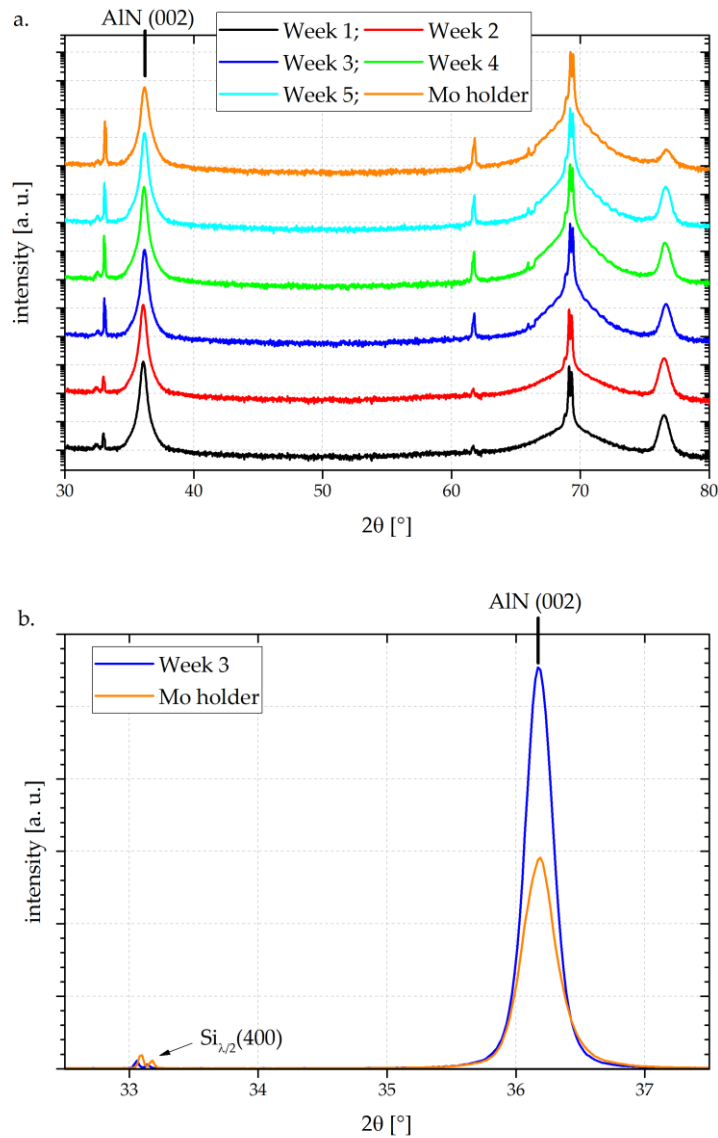
Fig. 4.9: (a) The XRD characteristics show the c-axis orientation of 0.5 µm AlN layers from week 1 to week 5 in comparison with the Mo sample holder. (b) The enlarged view on the (002) peak demonstrates the difference in XRD intensity of the week 3 sample synthesized with the clamped sample holder in comparison with the Mo sample holder.

4.3.4 Piezoelectricity

The piezoelectric coefficient measurements are executed with the piezometer by slicing one half of the wafer into four pieces (see Fig. 4.10). With the needle of the piezometer a uniform pressure is applied to the 1 mm diameter circular electrodes. The piezoelectric coefficient is measured on 4 samples of each wafer, which has itself 18 electrodes for each sample.
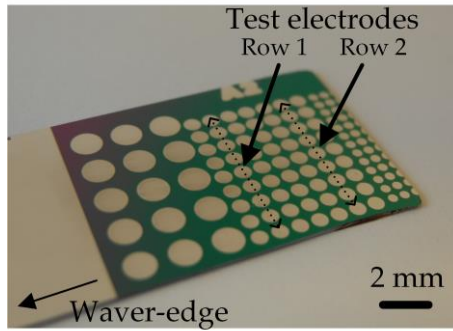
Fig. 4.10: Optical micrograph of the fabricated AlN circular test pattern on silicon circular top electrodes (diameter of 1.0 mm, indicated by arrow).

In Fig. 4.11 every boxplot consists of 72 circular electrodes per wafer. The minimum, the maximum, the arithmetic mean and the median value are marked in the diagram. It can be seen, that the sample holder has a strong impact on the sign of d_{33}. The results show that the clamped sample holder causes a negative sign of d_{33}, whereas the standard sample holder, where the wafer can bend freely, results in a positive sign of d_{33}. Additionally, the boxplots of the clamped sample holder indicate a substantial reduction of scattering of d_{33}. It shows an overall value of about -7 pC/N for all week samples and individual arithmetic mean values for each week. In contrast, the samples with the molybdenum (Mo) sample holder have a larger distribution in d_{33} values in every boxplot.
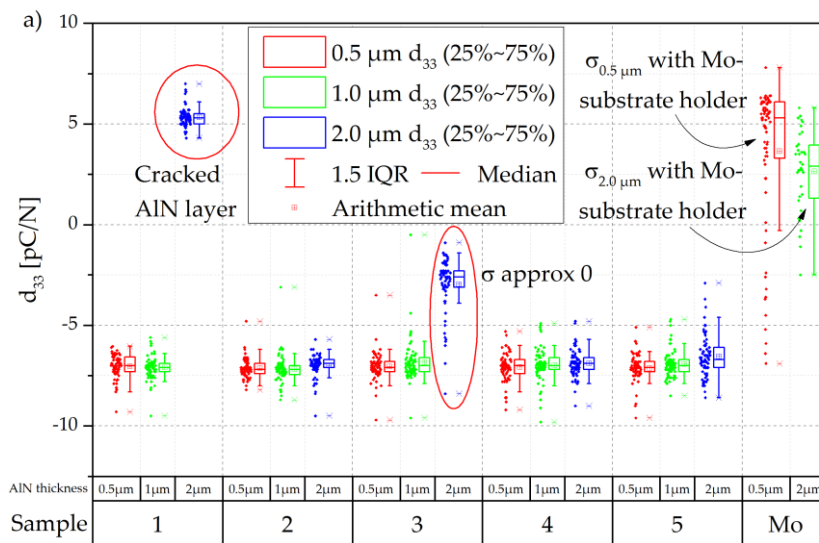
Fig. 4.11: The boxplots show the piezoelectric coefficient d_{33} of the samples from week 1 to 5 with an AlN device layer thickness of 0.5 µm, 1.0 µm and 2.0 µm fabricated with the clamped wafer holder compared to the standard wafer holder. Each boxplot represents the measurement of 72 individual test structures.

In the diagram, the samples with 2.0 µm thickness synthesized in week 1 and in week 3 attract attention due to their diverged measurement values. This is caused by the clamping fixture between the sample holder and the silicon wafer. Thereby the sample of week 1 reaches the highest deposition temperature of 160 °C during this investigation. The same sample has a positive layer stress of about 450 MPa with a positive d_{33}, as it can be seen in Fig. 4.4 (b). In fact, the AlN layer has particularly high stress level, which is shown through cracks in the AlN layer. This leads to a reduction, or even more noticeable, to a positive value of d_{33} as it is shown in Fig. 4.11 (a). Paying attention to the sample at week 3 with 2.0 µm thickness, where the evidence of a link between a very low layer stress sample with a layer stress value of -8.8 MPa and a low average d_{33} of -2.5 pC/N is shown. Referring to the temperature sensitivity of the c-axis orientation during deposition, the clamped sample holder keeps

the temperature typically below 140 °C. The temperature distribution on the surface may be uneven which implies an inhomogeneous d_{33} and an σ distribution [137]. A closer look at the larger range of d_{33} values suggests that the temperature of the wafer was not evenly distributed (see Fig. 4.12). The images of the Mo holder have a wide range d_{33} variation which is indicated in the larger scale at each image. The image at (c), week 1 attracts attention due to the mostly red colour, which is traced back to a cracked sample.
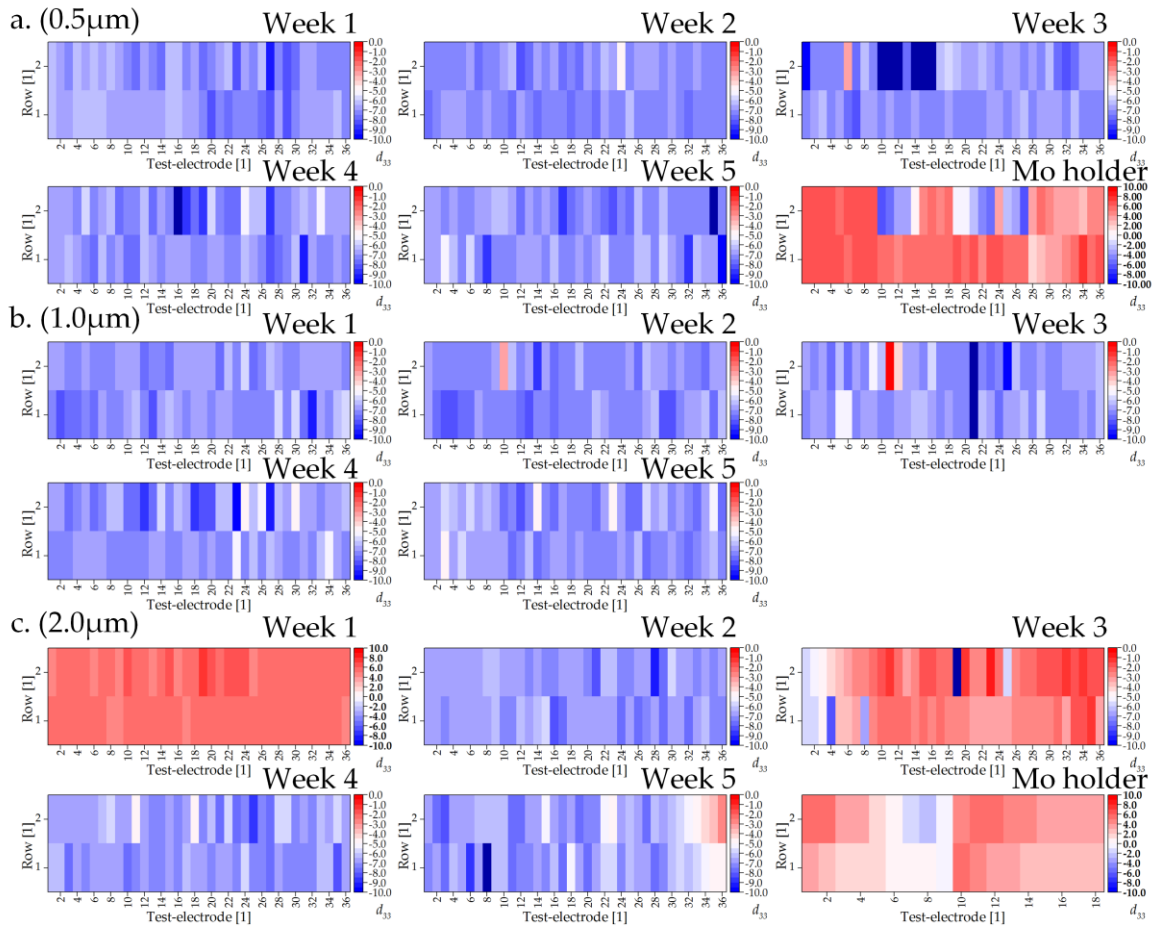
Fig. 4.12: d_{33} of (a) 0.5 µm (b) 1.0 µm (c) 2.0 µm AlN layer thickness.

These results indicate a relation between the biaxial layer stress in the deposited AlN layer and the d_{33} values both of which are depending on the crystallographic orientation (c-axis) of the deposited piezoelectric layer. Therefore, a change of the sign of d_{33} value indicates a change of the sign of the layer stress when the substrate and deposition-related conditions are kept constant.

4.3.5   Leakage current

The electrodes used for d_{33} measurements are also used for leakage current measurements. The leakage current density J of sputter-deposited AlN thin films at low electric fields, i.e. $E \leq 0.1$ MV/cm, show a dominant ohmic behaviour conduction mechanism. At larger electrical field strength of $E \geq 0.3$ MV/cm, J is dominated by a Poole-Frenkel (PF) mechanism [152] which is expressed as a function of E and T by the following relations,

$$J(E, T) \sim E \cdot e^{\frac{-E_A(E)}{k \cdot T}}$$

(4.2)

$$E_A(E) = q\left(\phi_B - \sqrt{\frac{qE}{\pi \varepsilon_0 \varepsilon_r}} \right),$$

(4.3)

where k denotes the Boltzmann constant, T the sample temperature, q the elementary charge, ϕ_B the barrier height, ε_r the relative permittivity, ε_0 the vacuum permittivity and $E_A(E)$ the thermal activation energy, respectively [132]. For ε_r a reasonable value for sputter-deposited AlN thin films is 10, as reported in a previous investigation [120].

An exemplary JV curve approximation of a 0.5 µm thin AlN sample deposited in week 3 is shown in Fig. 4.13 (a). The leakage current density J increases with the electrical field E and with the temperature T. The curves show a symmetric behaviour between positive and negative applied voltage. Additionally, an increase in temperature results in reduced hysteresis at lower voltage levels. In comparison, Fig. 4.13 (b) shows a larger hysteresis at the 0.5 µm AlN sample, which is deposited with the standard sample holder where the wafer can bend freely.
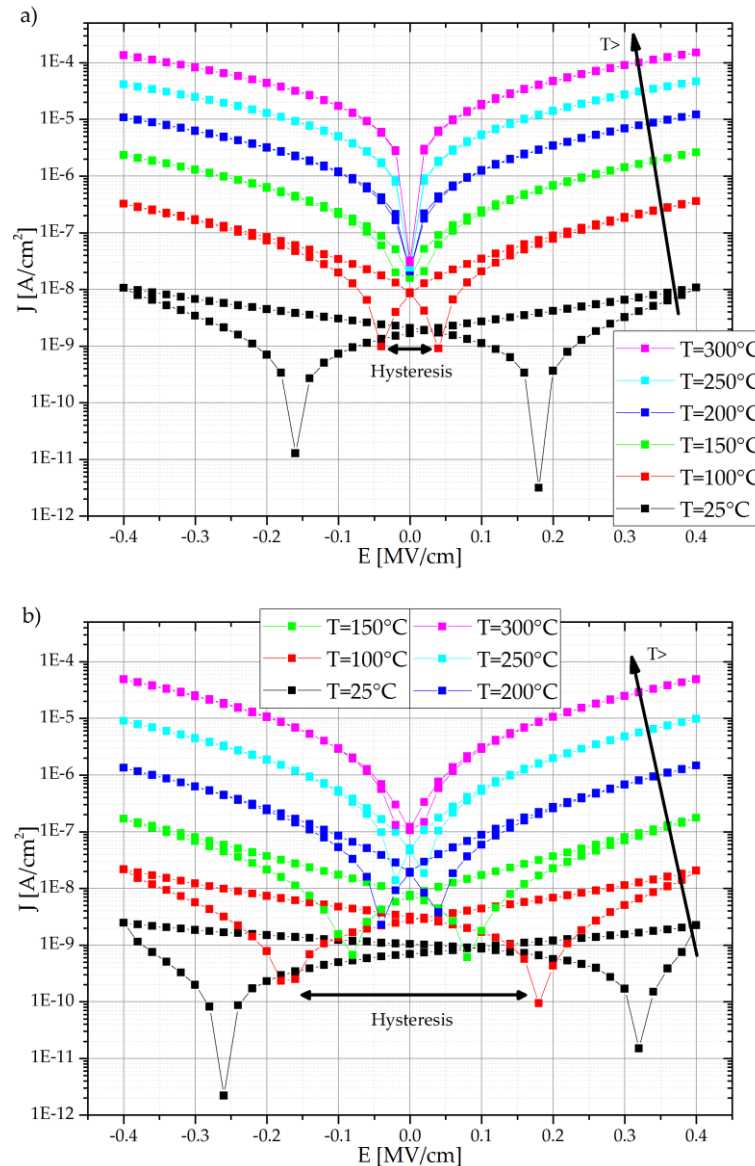
Fig. 4.13: A typical leakage current characteristics at different temperature levels of a 0.5 µm thin AlN film deposited in week 3 with clamped substrate holder at (a) and with free moving Mo substrate holder (b).

By rearranging eq. (4.2) to *ln(J)* divided by *kT*, $E_A(E)$ suggests a Poole-Frankel charge transport mechanism. A high linearity due to the thermally activated conduction mechanism of $E_A(E)$ for each E is observed. As example, the week 3 AlN sample with 0.5 μm was taken and displayed as Arrhenius plot in Fig. 4.14 (a). Compared to the sample deposited with the Mo holder, the fit to the standard sample fits less exactly to the experimental data, as shown in Fig. 4.14 (b). The measuring points of both diagrams are below the inner section of the linear curve, but above at the upper and lower end, what indicates a variation in trap depth. Comparing the results of (b) to (a), an improvement in linearity can be seen.
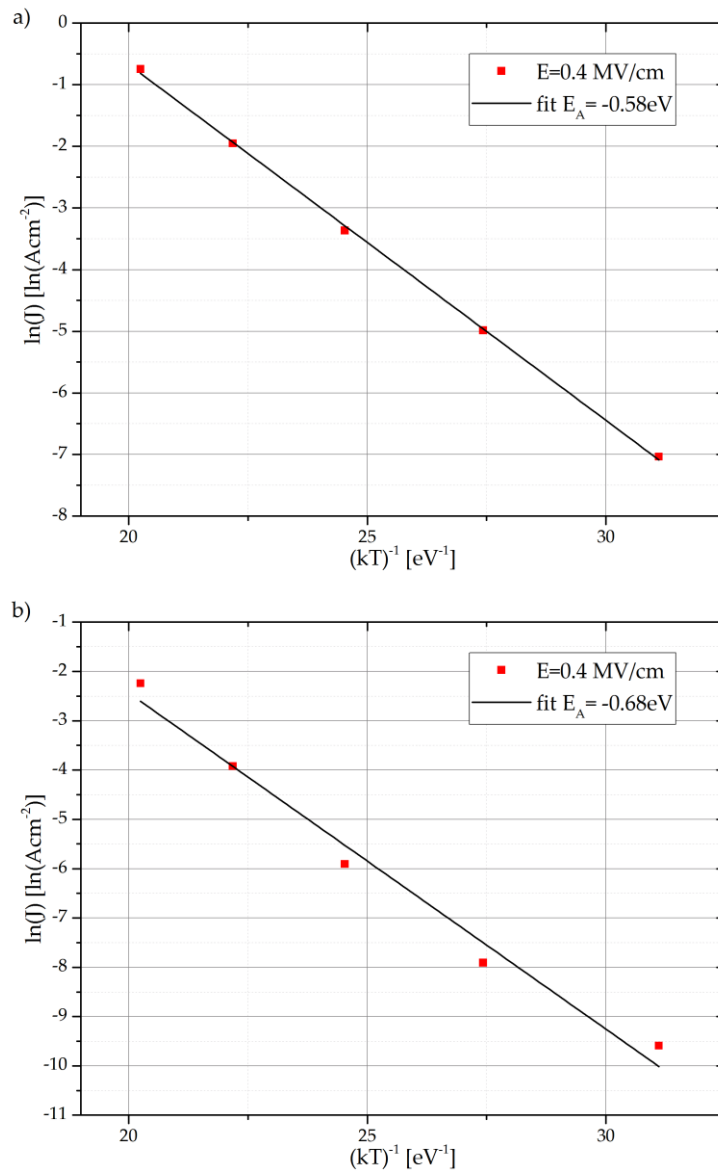
Fig. 4.14: The Arrhenius plot of leakage current of sample week 3 with 0.5 μm AlN thickness at E = 0.4 MV/cm is shown. The measurement points are at 100 °C, 150 °C, 200 °C, 250 °C and 300 °C with clamped substrate holder at (a) and with free moving Mo substrate holder (b).

Applying this approach to all samples from week 1 to 5, even for each thickness and also to the reference sample with the Mo holder, the results of the E_A values are listed at Tab. 4.2. Due to the focus on the dielectric strength of the AlN layer, the maximum voltage was limited to 20 V. This voltage is not exceeded by the measurement circuit equipment, which will be developed and presented in a later chapter. This results in a variation of electric field strengths in the layers of 0.5 μm (E = 0.4 MV/cm), 1.0 μm (E = 0.2 MV/cm) and 2.0 μm (E = 0.1 MV/cm) thickness.

AlN thickness	0.5 µm	1.0 µm	2.0 µm
Week	E_A [eV]	E_A [eV]	E_A [eV]
1 (clamped)	-0.53	-0.58	-0.60
2 (clamped)	-0.57	-0.62	-0.63
3 (clamped)	-0.58	-0.59	-0.59
4 (clamped)	-0.56	-0.61	-0.55
5 (clamped)	-0.56	-0.61	-0.56
Mo holder (freely movable)	-0.68	---	-0.63

Tab. 4.2: Activation energy E_A for AlN thickness of 0.5 µm (E = 0.4 MV/cm), 1.0 µm (E = 0.2 MV/cm) and 2.0 µm (E = 0.1 MV/cm) from week 1 to 5 for clamped sample holder and free moving sample holder (Mo sample holder).

Inserting (4.2) to (4.3) and fitting $E_A(E)$ to the measurement results, ϕ_B is determined. The results with 0.5 µm Fig. 4.15 (a), 1.0 µm (b) and 2.0 µm (c) AlN sample thickness are shown. The fitting curves result in the same values for ϕ_B for the negative and positive bias direction as it is expected from the results presented in Fig. 4.15 (a). In Fig. 4.15 (a, Mo holder) the barrier height of a sample fabricated with the Mo sample holder is shown. For electrical field values above $|E| > 0.35$ MV/cm it shows a Poole-Frenkel mechanism as the samples which were fabricated with the clamped substrate holder.

51
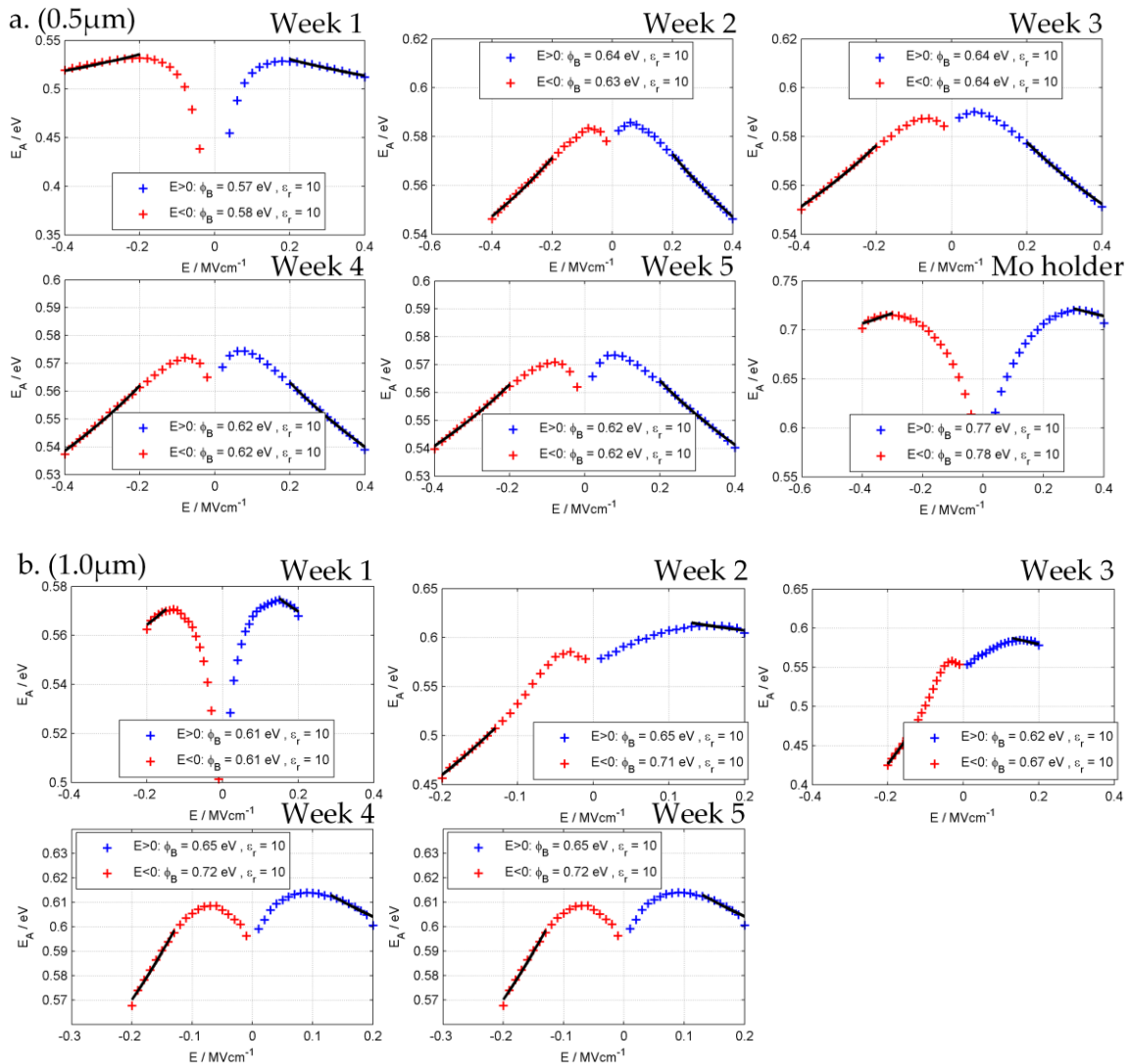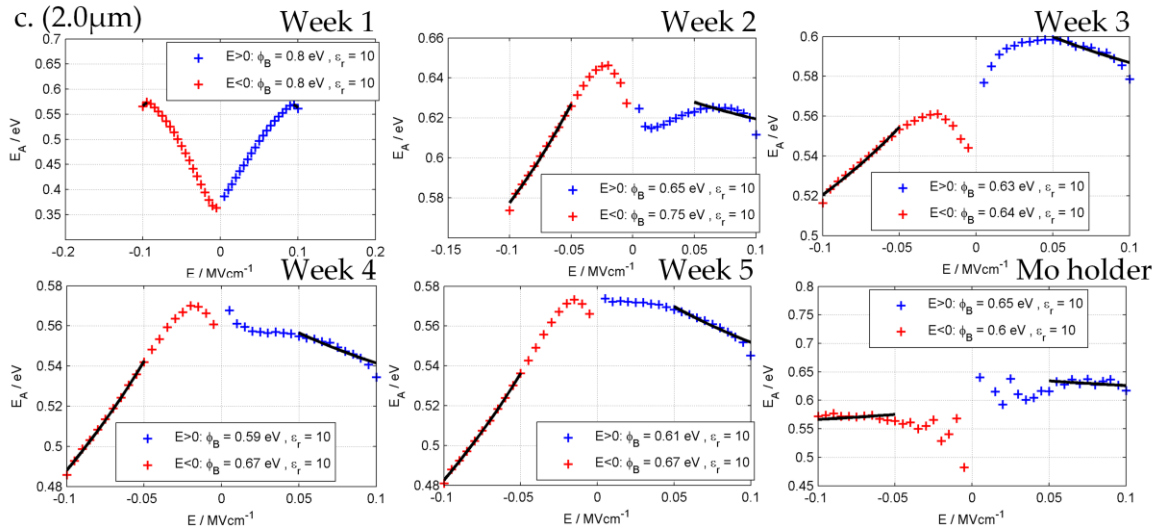
Fig. 4.15: The Poole-Frenkel evaluation of the barrier height of the samples with (a) 0.5 µm thickness, with (b) 1.0 µm and with (c) 2.0 µm.

The fit was applied to all samples fabricated with the clamped sample holder from week 1 to 5 and to all AlN layer thicknesses and for reference the fit was applied to samples fabricated with the Mo holder too. At Tab. 4.3, the results of ϕ_B are noted, which includes the ϕ_B values for both polarity directions of the supply voltage ($E > 0$ and $E < 0$).

AlN [µm]	0.5	0.5	1.0	1.0	2.0	2.0
E cond.	E < 0	E > 0	E < 0	E > 0	E < 0	E > 0
Week	ϕ_B [eV]	ϕ_B [eV]	ϕ_B [eV]	ϕ_B [eV]	ϕ_B [eV]	ϕ_B [eV]
1 (clamped)	0.58	0.57	0.61	0.61	0.80	0.80
2 (clamped)	0.63	0.64	0.71	0.65	0.75	0.65
3 (clamped)	0.64	0.64	0.67	0.62	0.64	0.63
4 (clamped)	0.62	0.62	0.72	0.65	0.67	0.59
5 (clamped)	0.62	0.62	0.72	0.65	0.67	0.61
Mo holder (freely movable)	0.77	0.78	---	---	0.60	0.65

Tab. 4.3: The barrier height separated into positive and negative E - field for samples with AlN thicknesses of 0.5 µm, 1.0 µm and 2.0 µm from week 1 to 5 for clamped sample holder and Mo sample holder is noted.

The values of E_A (Tab. 4.2) and ϕ_B (Tab. 4.3) of the samples fabricated with the clamped sample holder and fabricated with the Mo sample holder are shown graphically in Fig. 4.16. The distributions of ϕ_B in Fig. 4.16 (a) show that only the cracked AlN layer at the sample of week 1 has an influence on ϕ_B. The low stress sample at week 3 (2.0µm AlN thickness) has hardly any influence on ϕ_B. The samples fabricated with the Mo sample holder with a thickness of 0.5 µm draw attention due to the larger ϕ_B value of 0.77 eV compared to an average of 0.62 eV for the clamped sample holder. The detailed analysis of the JV characteristics in Fig. 4.13 (b) reveals a wider hysteresis of 0.36 MV/cm compared to 0.08 MV/cm in Fig. 4.13 (a) at 100 °C for the sample fabricated with the clamped substrate holder. Obviously, this effect disappears at increased temperature at the same AlN thickness, which can be seen at the Fig. 4.16.

52
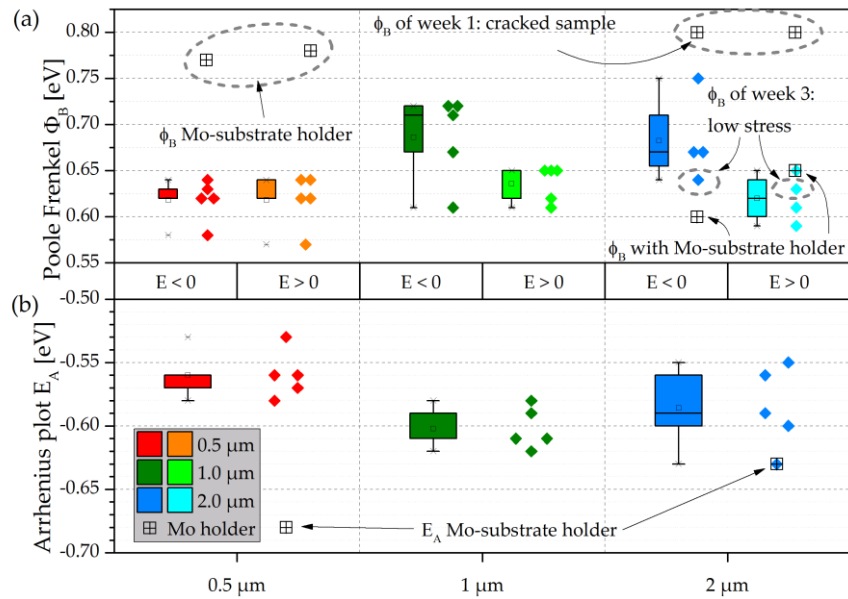
Fig. 4.16: The box plot of (a) Poole-Frenkel ϕ_B and (b) Arrhenius plot E_A of AlN samples from week 1 to 5 fabricated with clamped sample holder and fabricated with the Mo sample holder is shown.

A closer look to the boxplots of E_A in Fig. 4.16 (b) reveals a strong similarity of the average values for all fabricated AlN layer thicknesses and fabrication weeks in comparison to the Mo substrate holder. It is observed that E_A increases while the layer thickness increases from 0.5 µm layer to 1.0 µm. But the thickness of the AlN layer has minor impact on E_A when layer thickness increases to 2.0 µm. This leads to the conclusion that E_A strongly depends on the clamping mechanism and on the quality of the thermal contact.

4.4   Summary

In this chapter, a tailored Al substrate holder is developed, which allows to clamp the wafer before and during reactive sputter deposition of the thin film. In comparison to the standard Mo substrate holder, where the wafer can bend freely during AlN deposition, a noticeable temperature reduction of more than 60°C at the wafer holder was achieved, due to the reduced thermal contact resistance between the new substrate holder and the silicon substrate. This shifts the film stress from tensile to compressive which is observed at AlN samples in the film thickness range of 0.5 µm to 2.0 µm. This is presumably achieved by fixing the wafer, which prevents the wafer from bending further during the deposition process. The reduced deposition temperature has an impact on the etching characteristics as well. Basically, AlN samples with close to zero or positive film stress are much less attacked by phosphoric acid, independent of the substrate holder type used. In contrast, all samples with negative film stress are etchable in phosphoric acid. Etch residues originating from the AlN layers were found on the silicon surface after etching. For a quantitative analysis, the residues were evaluated by determining the size-specific area of the etch residues on the Si surface. Independent of AlN film thickness these distributions show a drop in area $\bar{\bar{A}}_{>0.95}$, indicating the removal of fast etching crystallographic planes in the AlN films. However, even after 1800 s exposure time, AlN residues remain on the silicon wafer, so that a complete removal of the AlN films is challenging. Due to the decrease in deposition temperature, other patterning approaches for the AlN film, like lift-off with organic photoresist, are feasible. Most importantly, a shift of layer stress of all deposited layers with the clamped substrate holder to compressive values is observed, thus enabling a reliable realization of defined film properties.

Additionally, an improvement of the electrical and piezoelectric properties of deposited AlN thin films as for instance the piezoelectric coefficient d_{33} or the IV characteristics was found. The leakage current

was determined to be a Poole-Frenkel conduction mechanism at high electrical field and the activation energy E_A and barrier height ϕ_B of the AlN layers from 0.5 µm to 2.0 µm thickness were evaluated. The AlN layers show a lower spread of piezoelectric coefficient d_{33}, activation energy E_A and barrier height ϕ_B compared with the AlN layers deposited with the Mo substrate holder. Interestingly, the cracked layers and the positive stress layers show a change in the d_{33} value, which provides the opportunity for future investigations.

5 MEMS cantilever

A cantilever serves as the sensing element within an AFM. The main properties, *i.e.* the Q-factor, resonance frequency and cantilever deflection depend on the material and the geometrical dimensions. The tip shape, tip radius and tip material are important for the surface interaction, but have negligible influence on the cantilever performance when changing from ambient pressure to vacuum. In this chapter, the design and the fabrication process of a micromachined cantilever, which offers the capability to dynamically change the Q-factor, are presented.

5.1 MEMS cantilever designs

5.1.1 Geometrical considerations

The components of the amplifier board limit the maximum resonance frequency of the cantilever to 120 kHz, which puts certain restrictions on the cantilever geometry. For most AFM tapping mode applications, the cantilever probe is excited in the first out-of-plane vibrational mode. The resonance frequencies (listed at Tab. 5.1) of this mode depend on both the cantilever length l_{Si} and thickness h_{Si} (see Eq. (3.26)). The red fields indicate resonance frequencies above while green marked fields indicate frequencies below this cut-off frequency. Nevertheless, all cantilever lengths are considered for the mask design, which allows to use the same mask set for an amplification set up with a higher cut-off frequency. The width of the cantilevers has no influence on the first out-of-plane resonance frequency when assuming an Euler-Bernoulli beam.

Cantilever length [µm]		100	250	500	750	1000
Cantilever thickness h_{Si} [µm]	3	414 kHz	66.2 kHz	16.6 kHz	7.4 kHz	4.1 kHz
	20	2.8 GHz	441 kHz	110.4 kHz	49.1 kHz	27.6 kHz

Tab. 5.1: The table shows the resonance frequencies depending on cantilever length l_{Si} and cantilever thickness h_{Si}.

5.1.2 Cantilever layout without compensation

The design of the fabrication masks is made accordingly to chapter 5.2.1, where the AlN lift-off patterning process is described. The MEMS device consists of three layers, which are shown in Fig. 5.1.
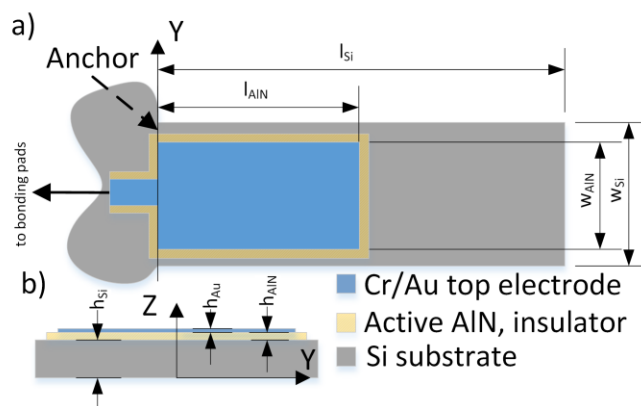
Fig. 5.1: Schematic of the cantilever, where (a) illustrates the top and (b) the cross-sectional view.

The resonantly operated cantilever is made from monocrystalline silicon using an SOI wafer, which is defined by the Si device layer thickness and formed through the Bosch etching process. For the cantilever length l_{Si} values of 100 µm, 250 µm, 500 µm, 750 µm or 1000 µm are selected. The width w_{Si} is set to 20 µm, 80 µm, 160 µm or 320 µm. The length and width of the piezoelectric layer, l_{AlN} and w_{AlN}, influence the electrical properties, *i.e.* the capacitance and the parasitic resistance of the

piezoelectric layer. Using the results from the simulation in chapter 3, the shortest length l_{AlN} is set to 100 µm. In addition, 150 µm, 200 µm, 250 µm, 300 µm and 500 µm are used for l_{AlN} in the mask design to investigate the impact of l_{AlN} on the cantilever oscillation performance, such as the Q-factor, the resonance frequency and the electrical output signal. The top electrode is used to apply an electric field across the piezoelectric layer and covers the entire AlN surface with the exception of an edge clearance, which is designed as self-aligned stack up. To avoid overlapping or shorts between bottom and top electrodes, the fabrication takes advantage of the different deposition methods related to the second mask. An undercut of 1 to 2 µm is used for the lift-off photo resist. As sputter deposition is not fully anisotropic, the open Si area including the area below the undercut is coated with AlN. Evaporation on the other hand, however, offers a much higher degree of anisotropy, resulting in a deposition-free area below the under-cut being masked by the photo resist. Consequently, the top electrode edge is recessed inwards from the AlN layer edge, resulting in good insulation between top and bottom electrode. To show an example of the manufacturing process related mask set, a representative set of photomasks for a cantilever with l_{Si} = 750 µm, l_{Si} = 80 µm and l_{AlN} = 500 µm is shown in Fig. 5.2. In order to demonstrate the device manufacturing process, the figure does not only show the mask, but also the resulting microstructure on the surface.
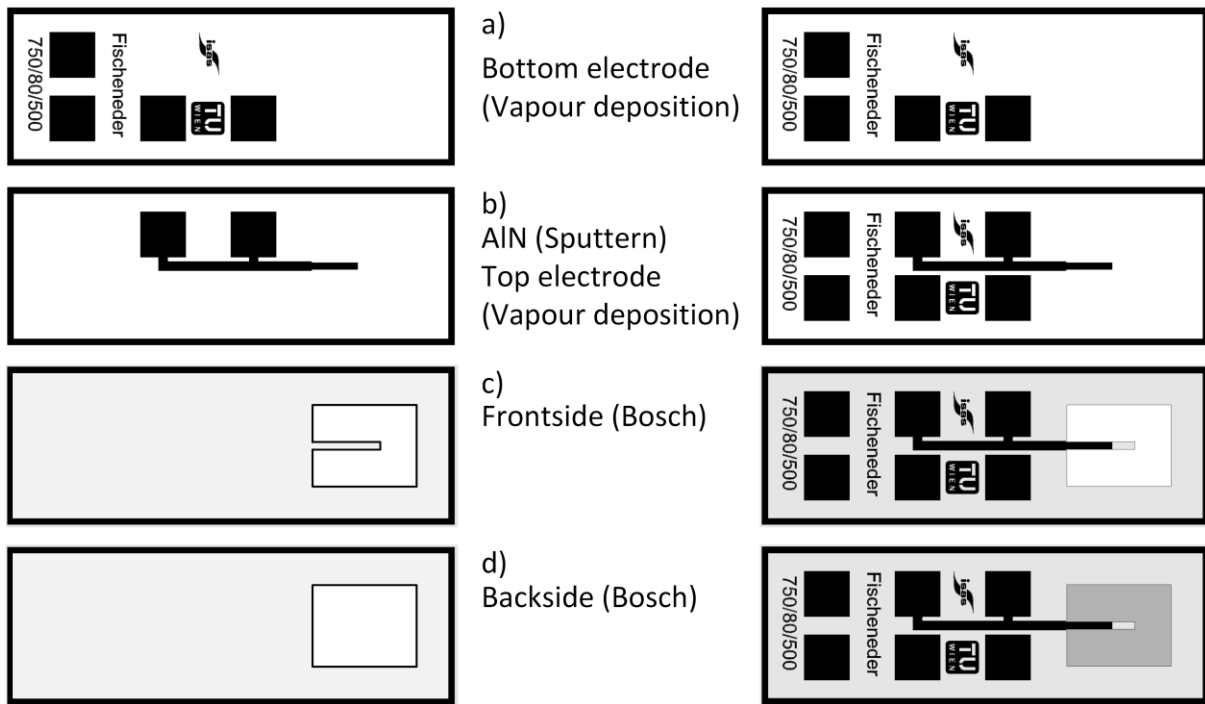
Fig. 5.2: A typical mask layout for cantilever fabrication is shown. The cantilever dimensions are 750 µm length, 80 µm width, 500 µm AlN length and 20 µm thickness. The schematic at (a) shows the first layer the bottom electrode contact, (b) the device layer with AlN and top electrode, (c) the front side Bosch etch which defines the cantilever and (d) the backside Bosch etch, which releases the cantilever.

With the first photo mask, which is shown in Fig. 5.2 (a), the electrical connections to the doped silicon bottom electrode are formed. Here, a Ti/Au bi-layer is e-beam evaporated and annealed to generate an ohmic connection to the highly-doped Si device layer. The layout contains two pads for the bottom electrode, which allows an electrical four-point measurement configuration. The second mask is shown in Fig. 5.2 (b). The AlN layer is sputter-deposited and subsequently, the Cr/Au top electrode is again e-beam evaporated. Both layers are patterned by a lift-off process in one fabrication step. The different coverage of the resist undercut through the use of different deposition processes ensures a local separation of the two layers. Here, the mask shows the two terminals of the four-point measurement configuration. The third mask, shown in Fig. 5.2 (c), is used for the topside Bosch etch to define the width and the length of the cantilever. Finally, the fourth mask for the backside etch is shown in

Fig. 5.2 (d). The backside Bosch etching step releases the cantilever from the bulk material. After dicing and cleaning, the devices are ready for mounting and wire bonding. The nomenclature on each cantilever die comprises the length, the width and the piezoelectric layer length, which is labelled as $l_{Si}/w_{Si}/l_{AlN}$. For the complete description of a cantilever, the thickness of the device layer is also necessary. This is given in the format $l_{Si}/w_{Si}/l_{AlN}/h_{Si}$. In addition, the cantilever has a frame (see Fig. 5.3), which protects the cantilever during the fabrication process. After mounting, the frame has to be removed.
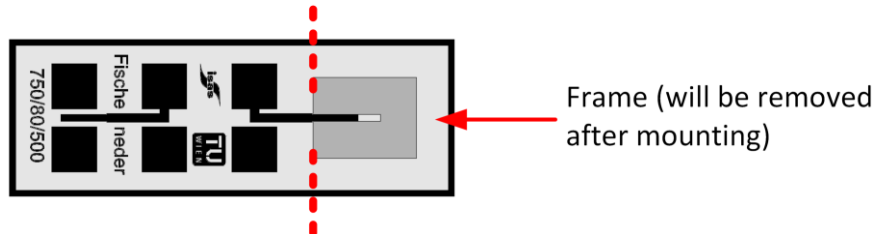
Fig. 5.3: Schematic of the protection frame, which will be removed after mounting.

5.1.3 Cantilever layout with compensation structures

A second set of masks is designed to realize an accurate compensation of temperature-induced, parasitic effects of the piezoelectric layer. For this purpose, an identical mechanically fully clamped (*i.e.* from the substrate non-released) compensation structure with the same cantilever dimension $l_{Si}/w_{Si}/l_{AlN}$ is used. The redesigned mask set with an additional compensation structure is shown in Fig. 5.4. In Fig. 5.4 (a) the unchanged bottom electrode is illustrated. The compensation structure, as shown in Fig. 5.4 (b), is an exact copy of the resonantly operating cantilever and thus, has the same electrical properties as the released cantilever, besides the motional branch of the Butterworth-van Dyke model. As before, the front-side Bosch etch process is used to define the geometrical dimensions of the cantilever. The associated mask is shown in Fig. 5.4 (c). The mask for the backside Bosch process, which releases the cantilever from the bulk material, is shown in Fig. 5.4 (d). Both final masks are the same as for the process without compensation structure.

a) Bottom electrode (Vapour deposition)

b) AlN (Sputtern) Top electrode (Vapour deposition)

c) Frontside (Bosch)

d) Backside (Bosch)
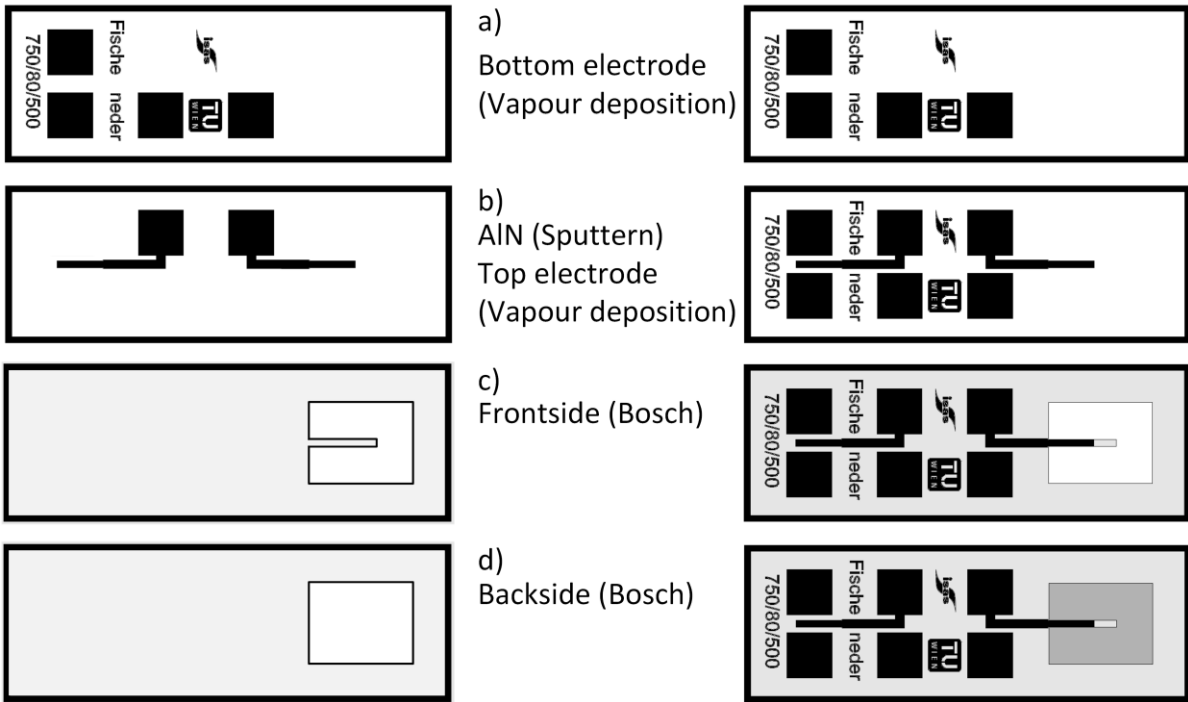
Fig. 5.4: The exemplary mask layout for cantilever with 750 µm length, 80 µm width and 500 µm AlN length is shown. The schematic in (a) shows the first layer the bottom electrode contact, (b) the device layer with AlN and top electrode, (c) the front side Bosch etch which defines the cantilever and (d) the back-side Bosch etch, which releases the cantilever.

An image of the fabricated wafer is shown in Fig. 5.5. The wafer is fixed onto adhesive tape subsequently diced using a rotating wafer dicing saw. Each device is then individually removed from the tape and cleaned with acetone and isopropanol.
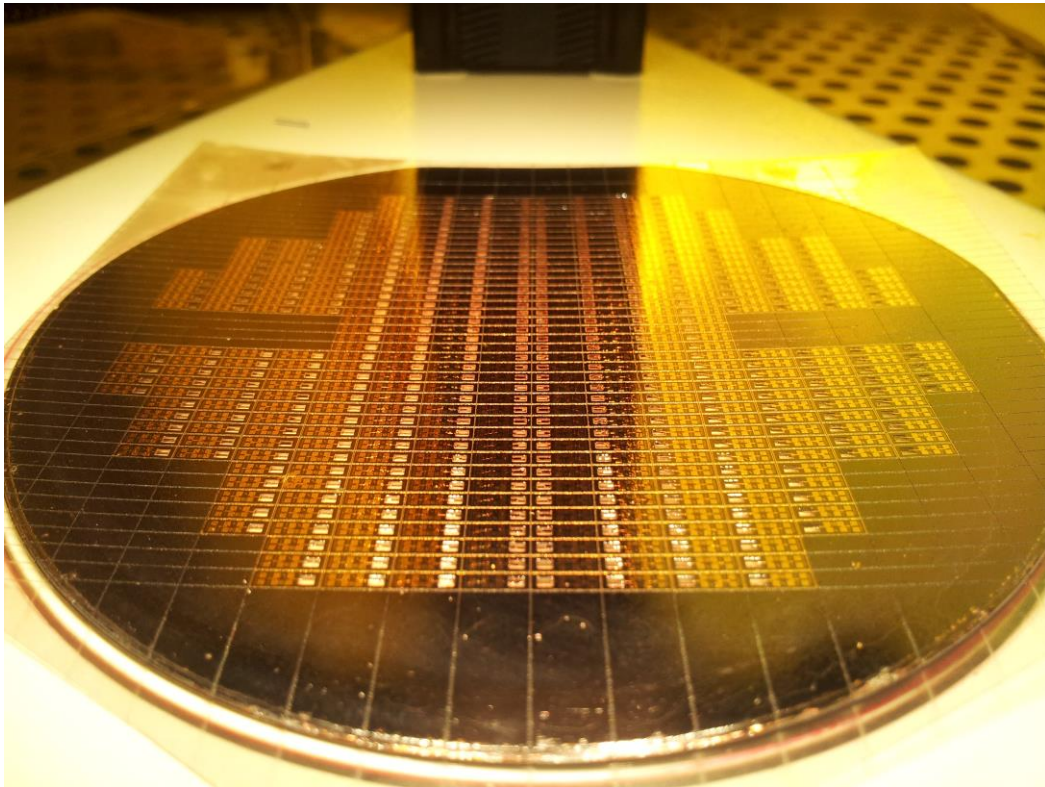
Fig. 5.5: Optical micrograph of the wafer with processed and diced cantilevers.

5.2 Manufacture of MEMS cantilevers

Beside the design of the photomask, a new process flow has to be developed for the tailored substrate holder, which is discussed in 4.2 "Clamped substrate holder". To ensure a proper photolithographic layer, which is the key for patterning with a lift-off process, the substrate temperature during deposition has to be kept well below the degeneration temperature of the resist.

5.2.1 Fabrication process of cantilevered resonators

An SOI wafer (Fig. 5.6 (1)) is used as substrate for the fabrication process. The photoresist AZ5214 is spin-coated onto the surface (Fig. 5.6 (2)) and subsequently UV exposed using the lithography mask for the bottom electrode contacts. Next, the resist is baked and flood exposed to achieve image reversal (Fig. 5.6 (3)). Ti (as adhesion promoter and for ohmic contact formation) and Au (as main electrode material) is deposited onto the surface using e-beam evaporation, what is schematically shown in Fig. 5.6 (4). After lift-off, the contact pads are formed and an annealing step is applied to create ohmic contacts to the highly doped Si (device resistivity of < 0.01 Ωm) bottom electrode (Fig. 5.6 (5)). Next, a second lift-off lithography step using the second mask is done (Fig. 5.6 (6)). AlN is sputter deposited [110, 120] (Fig. 5.6 (7)) and the top electrode of Cr/Au is again e-beam evaporated (Fig. 5.6 (8)). The clamped wafer holder is used to fix the wafer during the sputter process, which prevents wafer movement and keeps the process temperatures below 130°C. In Fig. 5.6 (9) the lift-off has been done, forming the piezoelectric layer stack. The topside Bosch etching process stops at the buried oxide (BOX) layer and separates the cantilever from the surrounding Si device layer, indicated in Fig. 5.6 (10). The backside Bosch etch process releases the cantilever from the bulk Si and a HF dip is used to remove the BOX to finalize the fabrication process.
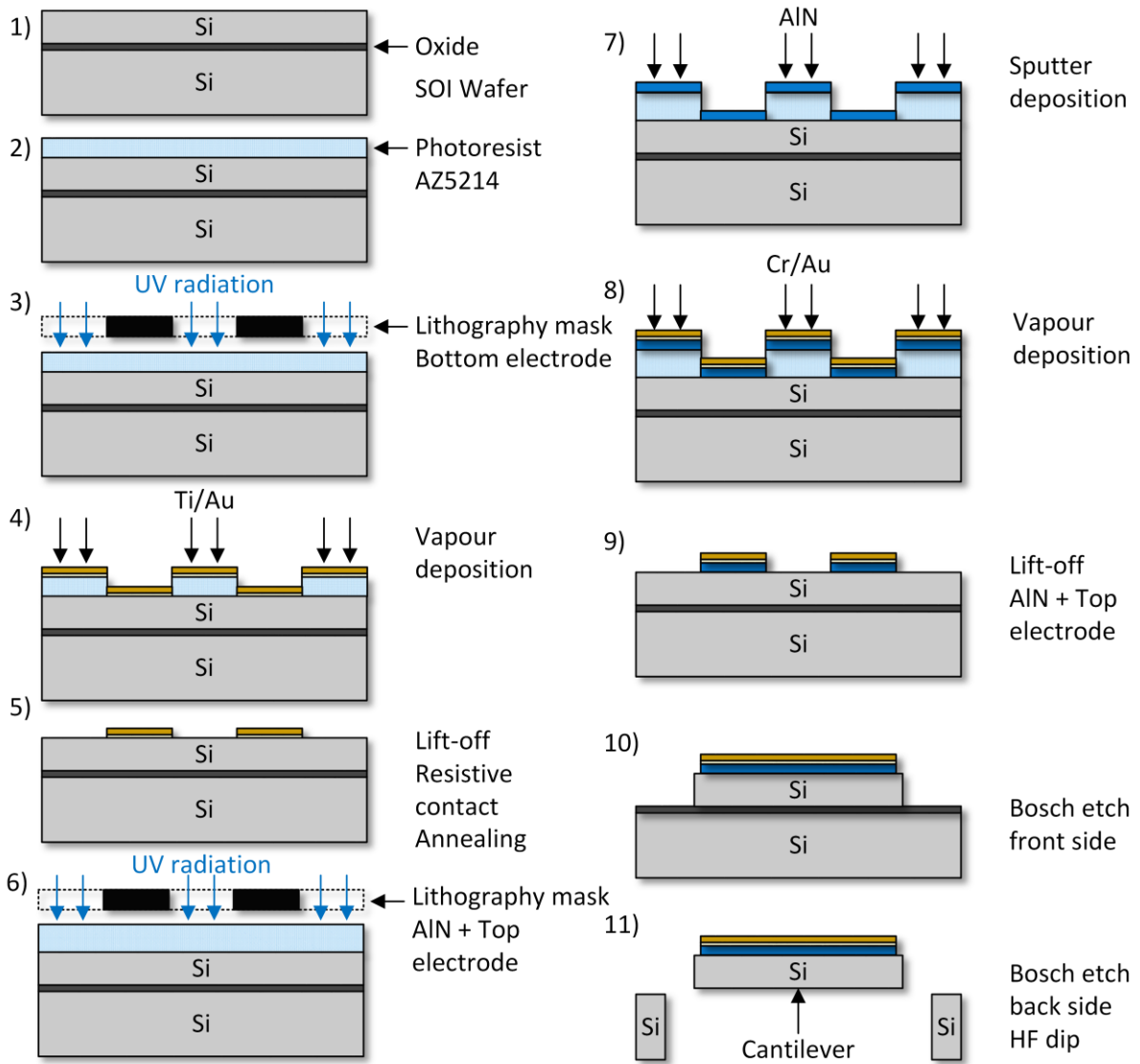
Fig. 5.6: Schematic process flow of self-actuated AlN cantilevers which initially start from a SOI (1) wafer. With optical lithography (2), (3), (6), thin film deposition (4), (7), (8) and lift-off steps (5), (9) the piezoelectric transducer is realized. Finally, the cantilever is formed and released via Bosch etching (10), (11).

The process flow in Tab. 5.2 shows the main process steps of cantilever fabrication process.

Technology	Description	
Substrate cleaning	Wafer-cleaner + ISO + HF	Bottom electrode
Lithography bottom electrode	Mask **"01 Layer Bot El Silicon"**	
E-beam deposition Ti/Au	100nm Ti, 200nm Au, annealing	
	Lift-off	
Lithography AlN + top electrode	Mask **"02 Layer AlN+Top El"**	AlN + top electrode
Sputter deposition AlN	500 nm AlN	
E-beam deposition Cr/Au	50 nm Cr, 200 nm Au	
	Lift-off	

BOSCH ÄTZEN FS	Mask "**05 Layer Top Bosch**"	
BOSCH ÄTZEN BS	Mask "**04 Layer Back Bosch**"	Release and separation
HF release		
Cut - separation		
Clean		

Tab. 5.2: MEMS cantilever process flow with tailored wafer holder for wafer clamping ensuring a low temperature sputter-deposition process.

The accuracy of the AlN lift-off process is tested using alignment marks on the wafer. After surface cleaning with acetone and isopropanol, an AlN layer with a thickness of 1 µm is deposited and patterned with lift-off as described above. After lift-off with acetone and surface cleaning with isopropanol, the resulting alignment mark is shown in Fig. 5.7.
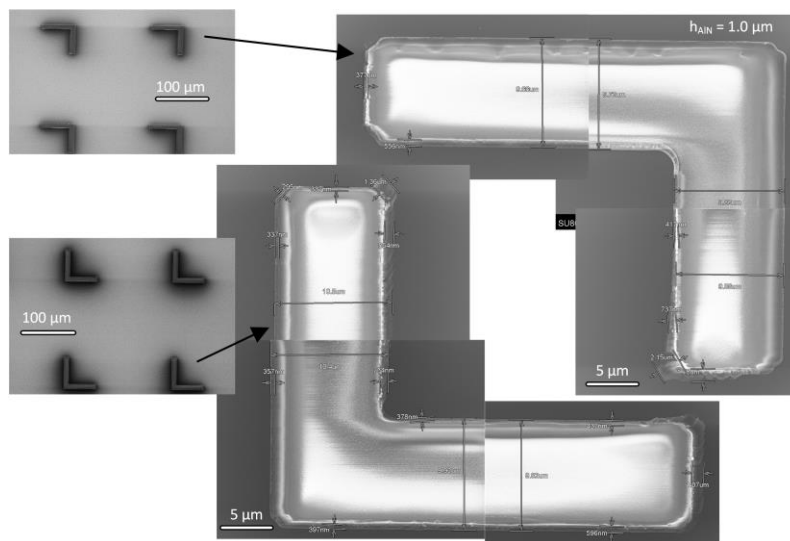
Fig. 5.7: Low and high-resolution SEM images of a 1.0 µm thin AlN test pattern are shown which was patterned by a lift-off process.

The figure is separated into low and high-resolution SEM images of the patterned AlN. The detailed SEM images show sharp AlN edges all around the alignment structure. With a deposited thickness of 1.0 µm, the nominal width of each alignment structure is 10 µm. As it can be seen from the figure, the resulting test structure has an actual width between 9.5 and 9.8 µm.

5.2.2 Thermal emissivity coefficient of Mo- and Al-substrate holder

For a successful patterning of the piezoelectric layer with lift-off, a substrate temperature during deposition below 130°C is required (with a safety margin of 10°C to 140°C, where the photoresist deteriorates). Therefore, a continuous monitoring of the substrate temperature is mandatory. A DIAS Pyrospot DGE°10N pyrometer with a temperature range of 100°C to 850°C, with a spot diameter of 3 mm at a distance of 300 mm and a spectral response at 2 µm to 2.6 µm wavelength is used to measure the temperature of the substrate holder inside the deposition chamber during deposition. Since the pyrometer is mounted below the substrate holder, it can only measure the temperature of the sample holder. Therefore, the pyrometer is employed to estimate the temperature of the substrate. Consequently, it is necessary to know the emissivity coefficient of the substrate holder material. The relation between thermal energy radiation by a blackbody radiator and the absolute temperature is given by the Stefan-Boltzmann law (5.1).

$$\frac{P}{A} = \sigma T^4 \; ; \; \sigma = 5.6703 \cdot 10^{-8} \; \frac{W}{m^2 s} \tag{5.1}$$

The emissivity e (e=1 for ideal radiator) is introduced in (5.1) to describe non-ideal radiators and is a material and temperature-dependent quantity, which has to be evaluated for the given substrate holder material. σ is the Stefan-Boltzmann constant and P the radiated power from an object. The resulting relation is given in (5.2). If the hot object is radiating energy into its cooler environment with temperature T_C, the radiation loss rate takes the form of (5.3).

$$\frac{P}{A} = e\sigma T^4 \tag{5.2}$$

$$P = e\,\sigma A(T^4 - T_C^4) \tag{5.3}$$

To determine the emissivity, a calibration measurement with a k-type nickel/chrome/nickel thermo-couple (temperature range -270 °C and 1372 °C), which is connected to an Agilent U1241A, was performed. Therefore, the sample holder is placed onto a hotplate and heated up to a certain temperature. The emissivity factor is adjusted until the temperature measured by an Optris MS Pro pyrometer corresponds to the temperature measured by the thermo-couple. The relation between the thermo-couple and the pyrometer reveals a constant emissivity of 0.102 at temperatures higher than 112 °C.

5.2.3 Electrical evaluation of deposited piezoelectric layer

The fabricated wafers undergo a process verification to confirm the successful deposition of the piezoelectric layer and the top electrode. Non-functioning piezoelectric layers typically have an electrical short between top and bottom electrode. To test for such failures, a wafer prober, which is described in 2.3.6 "Leakage current measurements", is used to apply a voltage up to 20 V between bottom and top electrode. Typically, the resistance is larger than 100 MΩ, but if the current through the piezoelectric layer exceeds 1 mA (< 20 kΩ), the device is classified as "Not OK". The results for two wafers with a device layer thickness of 3 µm and 20 µm are shown in Tab. 5.3.

Device layer	OK	Not OK	Amount	Yield
3 µm	75	129	204	37%
20 µm	37	24	61	61%

Tab. 5.3: The results of the electrical evaluation process of self-actuated AlN cantilevers with a device thickness of 3 µm and 20 µm are listed.

The difference in yield between the samples having either 3 µm or 20 µm device layer thickness suggest that the short circuit may not be the only failure mode. The reason has to be investigated in more detail in future efforts.

Cantilever impedance test with Agilent

After the release of the cantilever from the bulk and die separation, some exemplary devices are electrically examined. The electrical measurements are performed with a 4294A precision impedance analyser from Agilent. The impedance analyser applies a DC-bias of maximal 40 V with a maximum AC-voltage of 1 V_{rms} for a 4-wire measurement with a maximum frequency of 110 MHz. In this study, the device under test (DUT) is stimulated with a sinusoidal voltage of 0.5 VAC at zero bias while the current is recorded. The mounted devices are directly connected to the Agilent via BNC cables. The

recorded electrical parameters *i.e.* the conductance G, the susceptance B, the equivalent parallel capacity C_p and the equivalent parallel resistance R_p are plotted in Fig. 5.8 for three different cantilever and piezoelectric layer dimensions.
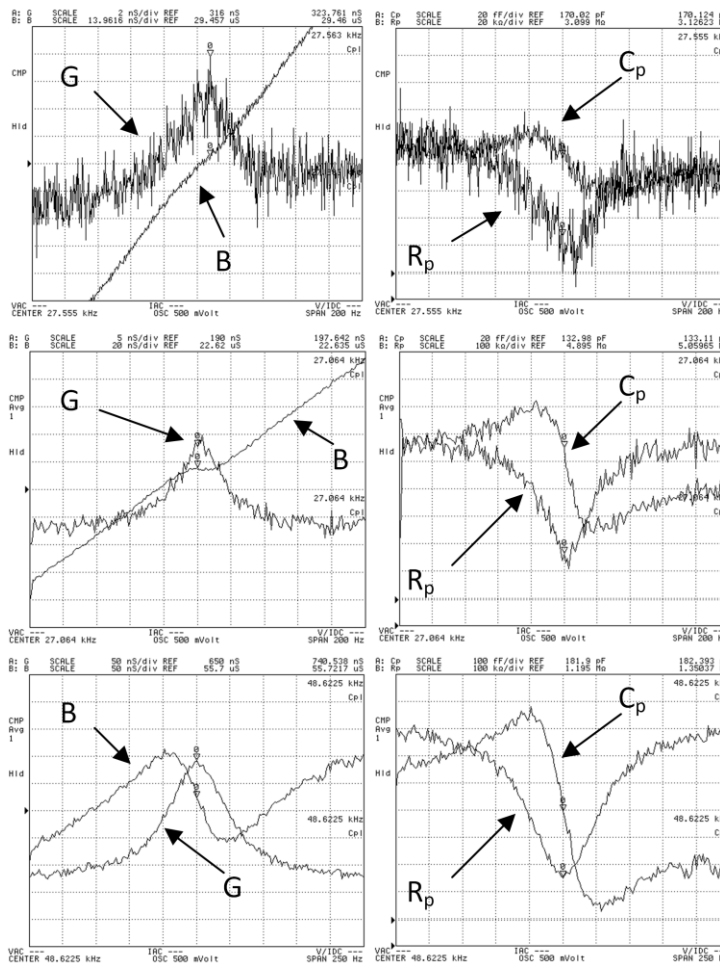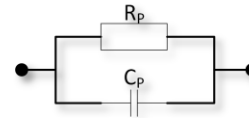
Fig. 5.8: Typical impedance measurements with three types of cantilevers with a thickness of 20 µm are shown. In (a) the cantilever has the dimension of 1000 µm length, 80 µm width and an AlN length of 150 µm. At (b) the cantilever has the dimension of 1000 µm length and 80 µm width and an AlN length of 300 µm. At (c) the cantilever has a dimension of 750 µm length and 80 µm of width and an AlN dimension of 500 µm.

In Fig. 5.8 (a) the AlN length is 150 µm and the resonance frequency is 27.555 kHz. Due to the short piezoelectric layer, the measurement signal is ΔG = 9.17 nS and ΔB is not quantifiable due to very small signal amplitude. The equivalent values are ΔR_p = 93.3 kΩ and ΔC_p = 0.076 pF. If the active layer area is doubled as shown in Fig. 5.8 (b), the electrical parameters increase to ΔG = 19.6 nS and ΔB is not quantifiable and the equivalent values are ΔR_p = 547 kΩ and ΔC_p = 0.106 pF. The resonance frequency decreases to 27.064 kHz which is caused by the increased weight and stiffness of the cantilever due to the integrated material. The signal noise ratio (SNR) increases due to the larger signal of the piezoelectric layer. In Fig. 5.8 (c) the cantilever is shorter, which increases the resonance frequency to 48.6225 kHz. The piezoelectric layer of the cantilever has the electrical parameters of ΔG = 209 nS and ΔB = 200 nS and the equivalent values are ΔR_p = 560 kΩ and ΔC_p = 0.752 pF, which show a lower noise level due to the larger amplitudes. The increase of the piezoelectric area does not go hand in hand with the increase of ΔR_p and ΔC_p. Primary the mechanical resonance of the cantilever is responsible for ΔR_p and ΔC_p and the area of the piezoelectric layer has a minor influence.

5.3   Cantilever mounting

The fabricated devices have to be connected mechanically to the shaker piezo and electrically to the supply/measurement circuit (see chapter 6.1.1 System description, Fig. 6.1). Therefore, a PCB is designed, on which the cantilever is glued to with UHU "Endfest 300" and cured with a temperature step at 100°C for 1 h. The higher temperature increases the glue strength. The PCB (Fig. 5.9) has a double layer design with a thickness of 1 mm and a dimension of 5.6 mm by 4 mm. The gluing area accommodates chips with a size of maximum 1.6 mm by 3 mm. The cantilever is electrically connected to the top side with bonding wires, as shown in Fig. 5.9 (a). The mechanical and electrical connections are handled with a PCB plug at the bottom side, which is shown in Fig. 5.9 (b). Doing so, a simple and quick exchange of cantilevers is possible. In Fig. 5.9 (c) the cantilever is mechanically glued and electrically bonded to the PCB.
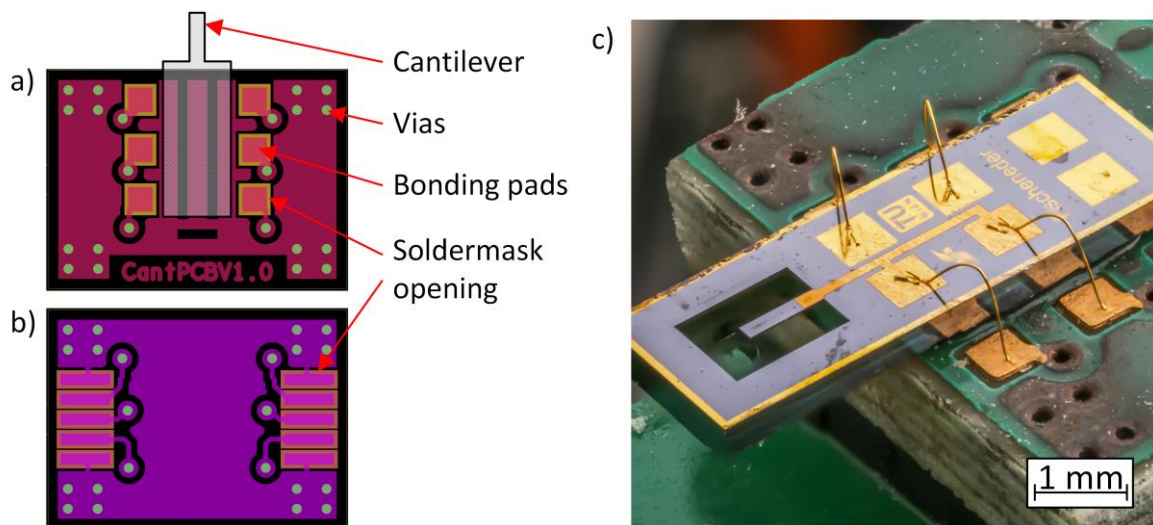
Fig. 5.9: *The layout of cantilever PCB (a) shows the corresponding top view with a cantilever placed schematically. The connector for the electrical and mechanical connections are placed on the bottom side of the PCB (b). (c) shows an optical photograph of the cantilever mechanically and electrically mounted onto the PCB.*

5.4   Summary

In this chapter, a new fabrication process flow with a low temperature AlN deposition and a self-aligned transducer stack up was introduced. Therefore, a lift-off process with an AZ5214 photoresist can be used for forming the active AlN layer and the top electrode. Through the reduction of process steps and through a lower count of lithography masks, a fast, cost-effective and reliable fabrication process is established. The improvements were verified by electrical and optical inspections to demonstrate the successful implementation of the fabrication and mounting process.

6 Results

In chapter 3 "Simulation of MEMS cantilevers" the proposed approach for Q-factor manipulation was evaluated through simulations. Later, a novel process flow for the cantilever fabrication, with self-aligned structures, was introduced. A low temperature fabrication process, described in section 4.2 (Clamped substrate holder) was used to synthetize in a reliable way piezoelectric AlN-layers with similar mechanical and electrical properties. After processing, the wafer was diced and the dies were glued and bonded onto a PCB. As a result, a piezoelectric driven cantilever was fabricated, to demonstrate the impact of an active Q-factor manipulation in vacuum. Three different approaches are discussed in this chapter.

In section 6.1 "Measurement system: Frequency generator (FGEN) and oscilloscope (DSO)", the superposition of mechanical oscillations from two sources is evaluated. The tapping piezo (shaker) is commonly installed on an AFM and serves as the primary excitation source. Second source will be the mechanical oscillation excited from the piezoelectric layer integrated on the cantilever. The superposition of both oscillations is used to manipulate the deflection of the cantilever and hence, to manipulate the Q-factor. Therefore, the impact of the phase-shift between cantilever excitation and the external tapping piezo is evaluated. A dual-channel frequency generator supplies the stimulation signals for both the tapping piezo (shaker) and the cantilever. An oscilloscope records the voltage signals from the laser LDV and Wheatstone bridge where the cantilever manipulates the differential voltage.

In section 6.2 "Measurement system: STM32", the capability of a microcontroller approach is demonstrated. When targeting an integration into an existing AFM, this approach focuses on the lowest space requirement. Therefore, the pulse-pause output of the microcontroller is selected to supply the piezoelectric film during the first half of the oscillation. The pause period is used to measure the voltage of the piezoelectric layer, which is generated by the force of the second half of the oscillation. Thereafter, the impact of variable phase shifts with rectangular pulse-pause signals between two channels is demonstrated. Like in section 6.1, the tapping piezo is powered with the first channel. The second channel of the microcontroller powers the piezoelectric layer. The desired Q-factor can be set through the software on the microcontroller, which is connected to a tailored amplification PCB, and adjusts the cantilever as well as the tapping piezo excitation pulse accordingly.

Finally, in section 6.3 "Measurement System: Mixer and Lock-In", the Q-factor manipulation with a Lock-In amplifier is introduced. This approach manipulates the excitation voltage of the piezoelectric layer through an amplified feedback of the current through the piezoelectric layer. The current is converted into a voltage by a transimpedance amplifier and the Lock-In amplifier extracts the real part and amplifies it proportionally. Through adjusting the amplification factor, the Q-factor can be adjusted.

6.1 Measurement system: Frequency generator (FGEN) and oscilloscope (DSO)

With this approach, the frequency generator provides two individual sinusoidal stimulation signals with a defined frequency-dependent start phase ϕ_{start}, which are applied to the cantilever and to the shaker, respectively. By using only standard lab-equipment for the manipulation of the cantilever oscillation, this straightforward approach can be transferred to a microprocessor-controlled solution, which can be realized as a low-cost measurement equipment.

6.1.1 System description

The complete measurement system is illustrated in Fig. 6.1, where a MATLAB program controls the FGEN and the DSO via USB interfaces.
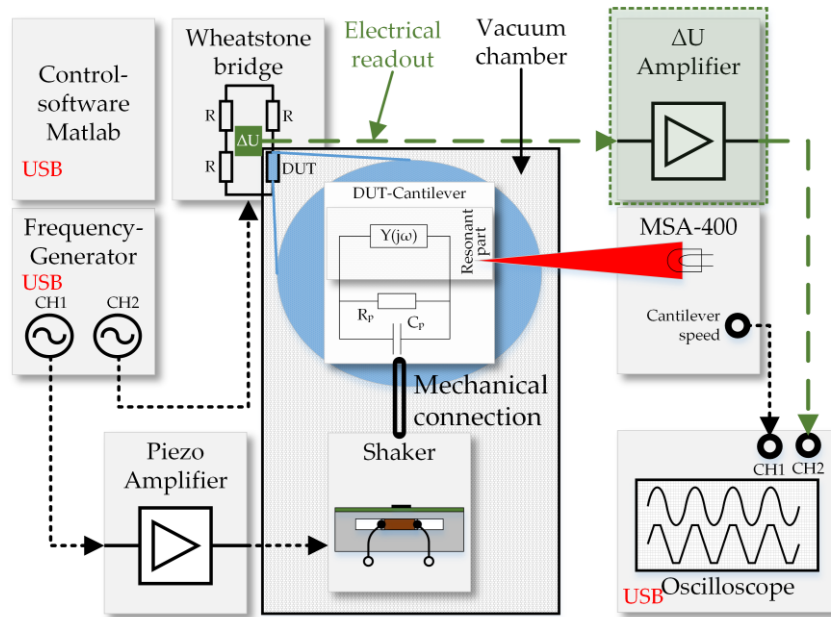
Fig. 6.1: The block diagram shows the measurement set-up, which is used for the characterization of the actively damped MEMS cantilever.

The FGEN provides a sinus signal from CH1, which is boosted to 27 V by a custom-made piezo amplifier. This drives the tapping piezo (shaker), which generates the external mechanical excitation of the cantilever. In contrast to the external mechanical excitation, the signal from CH2 is applied to the Wheatstone bridge where the cantilever acts as DUT, which is called the internal mechanical excitation. The potential difference *ΔU* of the Wheatstone bridge is amplified (adjustable up to 95 dB) and recorded by the oscilloscope at CH2. To verify the electrical signal, the cantilever oscillation is simultaneously measured with a LDV (MSA-400) and recorded with the oscilloscope at CH1. A MATLAB program records the signals via a USB interface.

The DUT is located in the vacuum chamber at a pressure of $6.5 \cdot 10^{-5}$ mbar, where the viscous damping effect of the residual gas atmosphere is negligible [153]. A partial view on the vacuum chamber is shown in Fig. 6.2, where the LDV has an optical access port to the cantilever. Inside the chamber, the cantilever is glued onto the cantilever PCB, which is connected to the interface PCB, which is attached to the shaker (shown in Fig. 6.3). The tapping piezo externally stimulates the cantilever oscillation through the mechanical connection between tapping piezo and cantilever. The second mechanical stimulation is done with the piezoelectric AlN layer, which is connected via the BNC plugs to the Wheatstone-bridge.
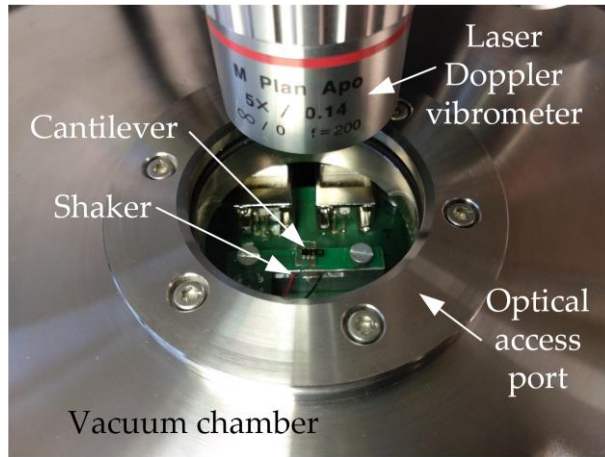
Fig. 6.2: The photograph shows the bonded MEMS cantilever which is mounted on a custom-built shaker. The complete set-up is placed in a vacuum chamber, which has an optical access for the LDV.
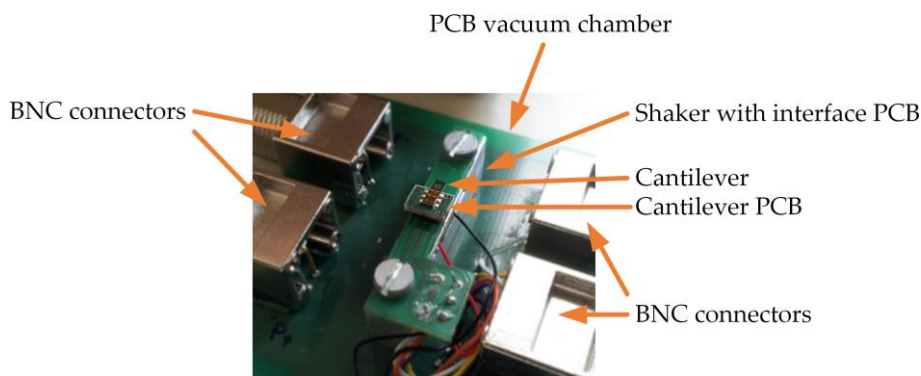
Fig. 6.3: The photograph shows the PCB which is fixed in the vacuum chamber. It contains the shaker with the cantilever and allows the connection to the piezo amplifier and to the Wheatstone bridge.

The electrical read out of the Wheatstone bridge is verified with a PSpice circuit simulation (see Fig. 6.4).
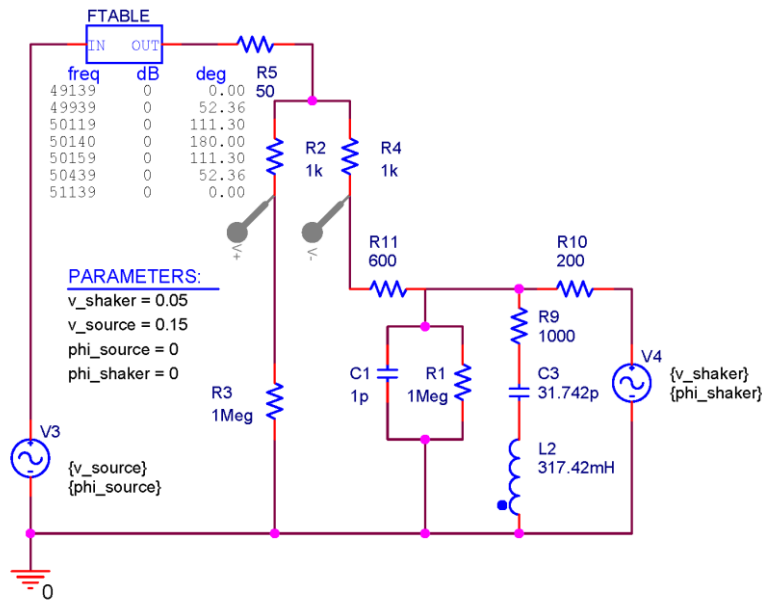
Fig. 6.4: The equivalent circuit of the electrical circuit shows the piezoelectric cantilever, the Wheatstone bridge and the shaker. The phase difference between the stimulating voltage at the integrated piezoelectric layer and the drive signal for the piezo shaker is mapped through the FTABLE block.

The simulation circuit is supplied by two voltage sources V3 and V4. The V3 is chosen by the measurement of the voltage far off the resonance frequency and it becomes attenuated by the wiring resistor R5 with 50 Ω. The phase deflection of V3 is mapped by the block FTABLE, which generates the frequency-dependant phase shift. V3 powers the Wheatstone bridge (WB) and the voltage difference *ΔU* is measured between the branch of R2, R3 and the branch of R4, cantilever circuit. R2, R3 and R4 are defined by the measurement setup. The equivalent circuit of the wiring and the piezoelectric layer is constructed through R11, C1, R1, R9, C3 and L2. R11 implies the wiring to the vacuum chamber, the electrical feedthrough, the wiring of the cantilever holder, the printed circuit board, the bonding and the resistance of top and bottom electrode of the die. C1 and R1 are the parasitic piezoelectric elements and R9, C3 and L2 the electrical equivalent circuit of the mechanical resonator which are matched to the electrical measurements. The impact of the mechanical shaker on the differential voltage (*ΔU = V₊ - V₋*) at the measurement bridge is represented by V4 and R10. The mechanical shaker was replaced by an electrical equivalent circuit, which consists of a voltage source with an internal resistance.

6.1.2   Phase shifting at resonant operating MEMS cantilevers

The active Q-factor adjustment requires two parameters, namely the start phase ϕ_{start} and the phase deflection $\phi_{deflection}$. The phase curve is shown in the diagram (see Fig. 6.5) where ϕ_{start} is denoted from -90 ° to 0 ° with a $\phi_{deflection}$ of 180 °. While the phase of the shaker actuation voltage is always fixed to 0°, the relative phase of the integrated piezoelectric actuator follows the presented characteristics, where the phase is constantly adjusted at each frequency value. This approach applies to one resonance frequency spectrum, which is unique for one type cantilever. For simplicity reason, the phase curve is modelled with straight lines instead of applying a Lorentz-function.
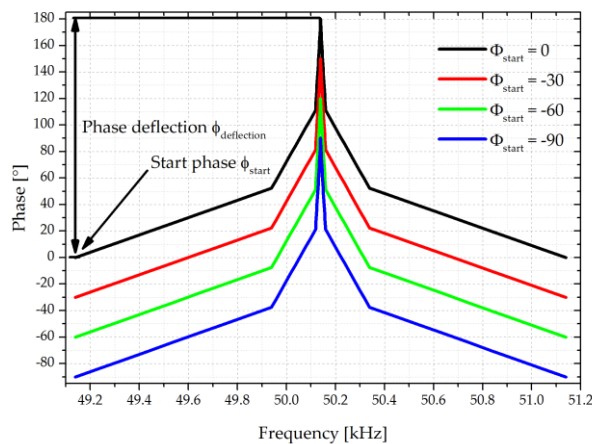
Fig. 6.5: The phase characteristics of the stimulating voltage, which is applied to the integrated piezoelectric layer with respect of the supply voltage of the shaker. The shape of the phase shift between cantilever and shaker is kept the same, while the starting phase ϕ_{start} is varied to manipulate the Q-factor.

6.1.3   Frequency independent phase shift applied at MEMS cantilever

In advance, the dependence of the Q-factor in air atmosphere related to any frequency independent phase shifts between cantilever and shaker actuation has to be verified. The phase of the power supply (FGEN - CH1) of the shaker is kept constant while ϕ_{start} of the integrated cantilever actuation is changed in 30 ° steps from 0 ° to 330 °. The oscillation of the cantilever is recorded both optically with a laser Doppler vibrometer (LDV) and electrically by the Wheatstone bridge and the differential voltage amplifier. Basically, the cantilever velocity amplitude depends on the cantilever phase difference between cantilever and shaker actuation, which is shown in Fig. 6.6 (a). When the phase shift is increased, the amplitude of the cantilever velocity amplitude reduces while it reaches its lowest value

at 180 ° due to destructive interference. Considering the Q-factor of the normalized cantilever velocity, which is presented in Fig. 6.6 (b), the equal curve shapes indicate an almost constant Q-factor in the range of 3460 to 3860. This confirms the independence of the Q-factor from the phase shift value at the piezoelectric thin film.
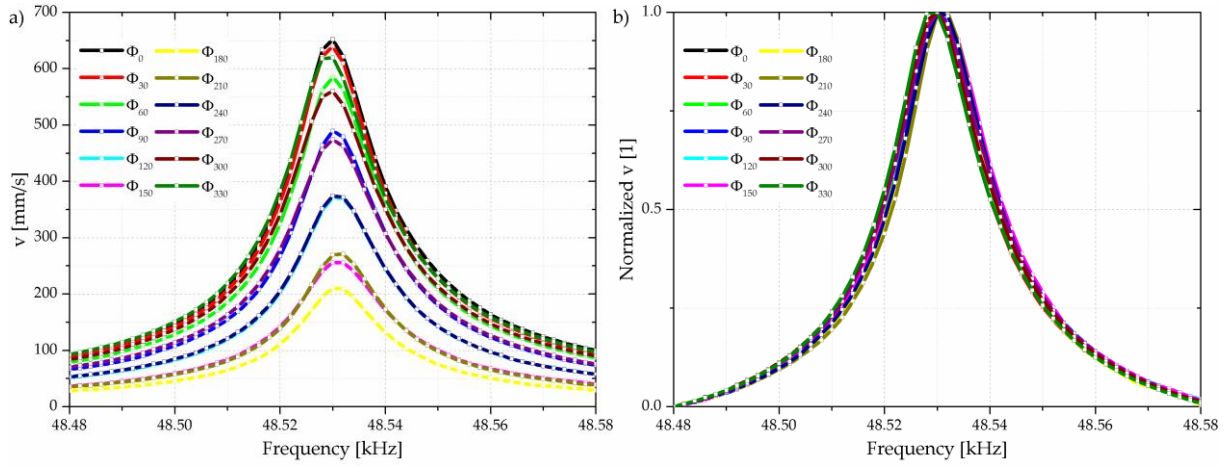
Fig. 6.6: (a) The absolute velocity measured with LDV and (b) the normalized velocity of the cantilever tip are shown. The cantilever actuation phase is changed in 30 ° steps from 0 ° to 330 ° related to the shaker actuation.

At the same time, the electrical measurements of *ΔU* at the Wheatstone bridge are illustrated in Fig. 6.7 (a). If these data are normalized, as shown Fig. 6.7 (b), an easier comparison of the electrically measured Q-factors, which are ranging between 3300 and 5300, is possible.
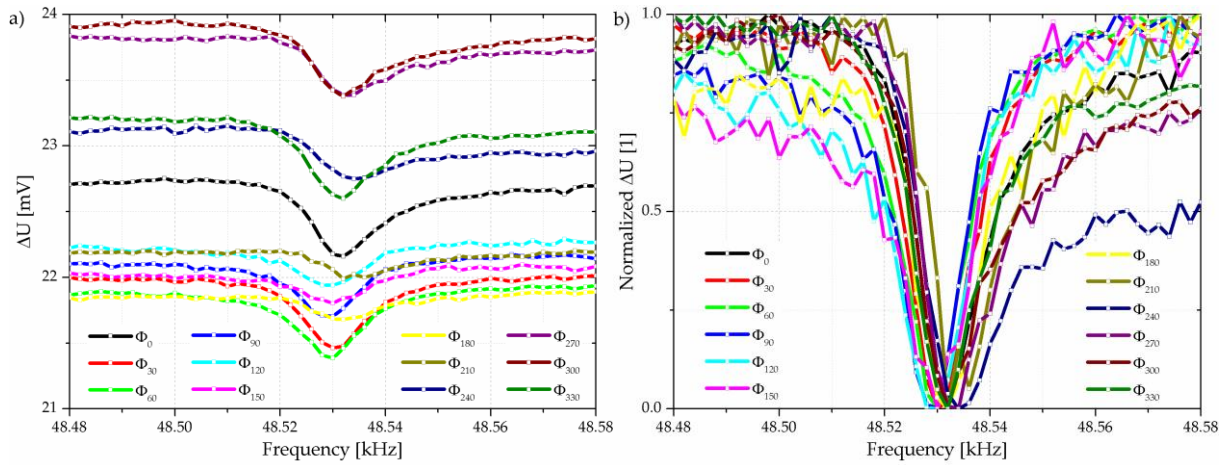
Fig. 6.7: The Wheatstone bridge differential voltages (a) and the corresponding normalized values (b) are shown. The cantilever actuation phase shift varied stepwise between 0 ° and 330 ° with respect to the shaker actuation.

The significant variation in the electrical output signal can be attributed to the absence of shielding in the wiring circuit and the presence of a DC component in the electrical signal, which limits the oscilloscope's utilization of the entire measurement range. The Q-factors are determined by $Q = \frac{f_r}{B_{0.707}}$ (optical measurement) and $Q = \frac{f_r}{B_{0.293}}$ (electrical measurement), where f_r, $B_{0.707}$ (3dB cut-off bandwidth) and $B_{0.293}$ (3dB transmission bandwidth) represent the resonance frequency and amplitude bandwidths, respectively. As shown in Fig. 6.8, the Q-factors determined by LDV are constant within the measurement accuracy of about ± 6%, but those deduced from the electrical measurements show a substantial higher scatter due to the poor peak characteristics at the resonance frequency. The systematic deviation between the optical and the electrical obtained Q-factor can be attributed to the narrower electrical resonance peak (confer Fig. 6.6 (a) with Fig. 6.7 (a)). The Wheatstone bridge and

the oscilloscope might clip the lower side of the resonance peak (see the peak in Fig. 6.25 (a)) and the resonance peak appear narrower.
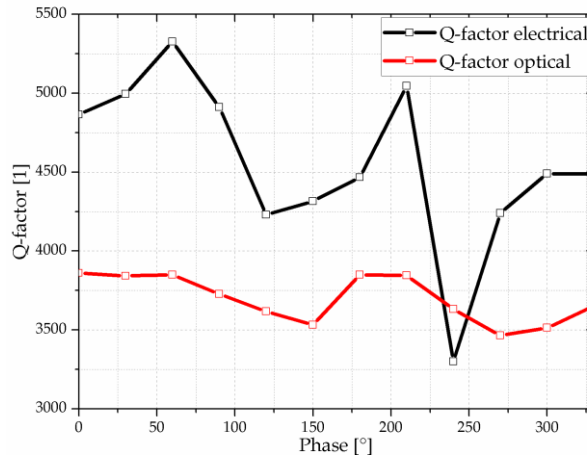
Fig. 6.8: The Q-factors are determined either electrically or optically as a function of phase shift between cantilever actuation and shaker.

6.1.4   Variable phase shift applied to the MEMS cantilever in the frequency domain

In the latter section it was shown, that the Q-factor remains constant even when the frequency-independent phase-shift between shaker and cantilever actuation changes. While the phase of FGEN - CH1 is fixed at 0°, a MATLAB script varies the phase shift of the signal from FGEN - CH2. The oscilloscope records the cantilever tip velocity measured with the laser Doppler vibrometer, as shown in Fig. 6.9 (a) at CH1. It should be mentioned, that these measurements are made with a different cantilever, which has a larger resonance frequency of 50139 Hz (before: 48530 Hz). The corresponding normalized oscillation velocity amplitudes are shown in Fig. 6.9 (b). Due to the change of ϕ_{start} in 30 ° steps from -90 ° to 0 °, the cantilever oscillation amplitude spectrums show a broader normalized resonance peak, which is shown in detail in the insert of the figure.
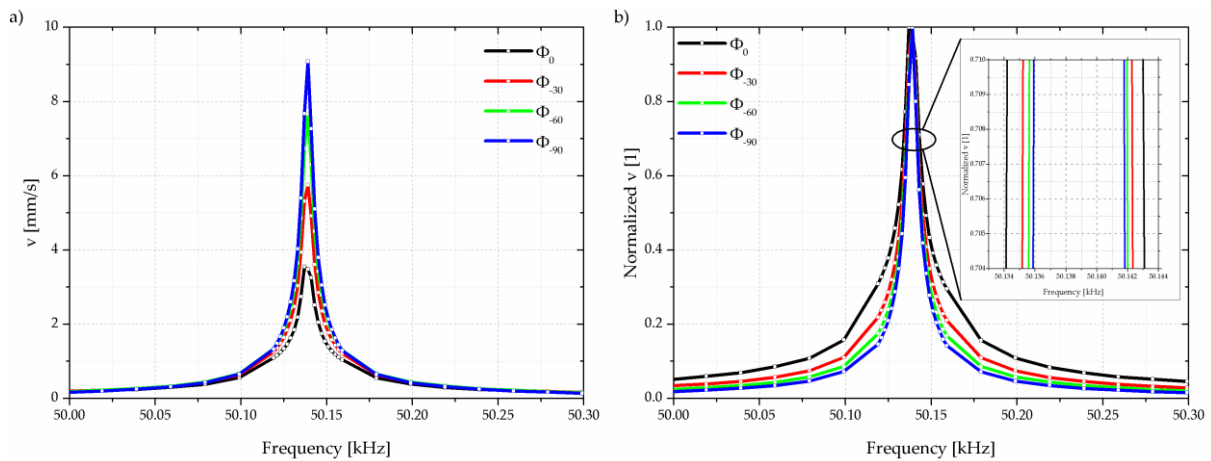
Fig. 6.9: The absolute velocity (a) and the normalized velocity of the cantilever tip (b) of a frequency-dependent, phase shifted excitation are shown. The inserted lines serve as a guide to the eyes.

Simultaneously to the capturing of CH1, the oscilloscope records the amplified electrical differential voltage of the Wheatstone bridge at CH2. In Fig. 6.10 (a) the frequency spectra of the electrical measurements are shown, while in Fig. 6.10 (b) the curves are shifted in y-direction for the purpose of clarity. Furthermore, the frequency spectra of the electrical characterisation are compared with simulated data. The latter spectra are calculated with the equivalent circuit from Fig. 6.4 and plotted in blue, green, red and black.
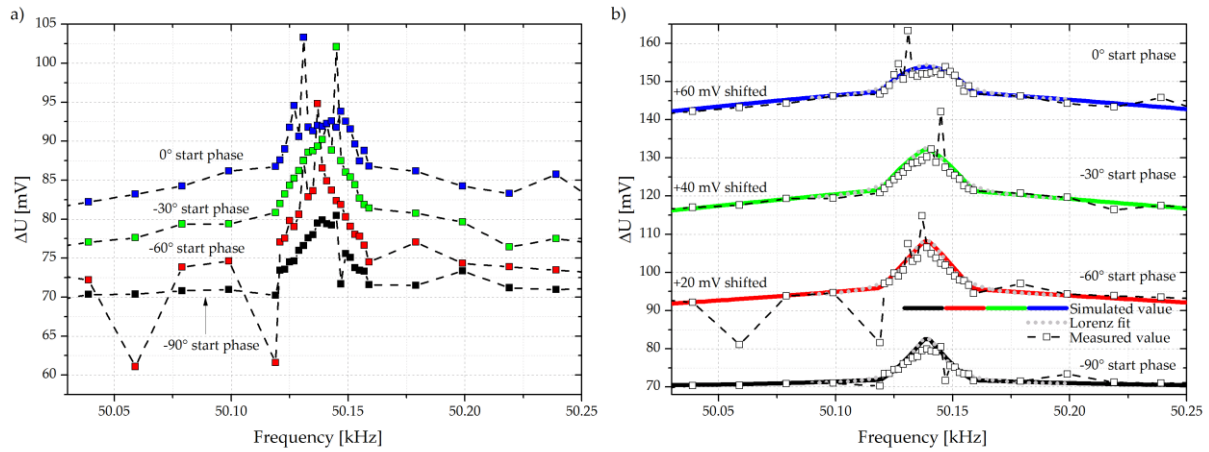
Fig. 6.10: (a) The differential voltages of the Wheatstone bridge of the starting phase of -90 °, -60 °, -30 ° and 0 ° are shown. (b) The differential voltages of the Wheatstone bridge and the simulated voltage frequency spectra of the starting phase of -90 °, -60 °, -30 ° and 0 ° are shown. For reasons of clarity, the individual curves are shifted of +20 mV, +40 mV and +60 mV in y-direction.

The Q-factor is extracted from Fig. 6.9 with $B_{0.707}$ and from Fig. 6.10 with a Lorentz fit (6.1). Tab. 6.1 lists the optically measured Q-factors, which are decreased by a factor of about 1.6 from 8746 at ϕ_{start} = -90° to 5533 at ϕ_{start} = 0°. The evaluation of the electrical spectrum reveals a Q-factor reduction of about 1.9 from 4328 to 2299. Independent of the starting phase, the Q-factors determined electrically are twice the value of the optically measured values. This systematic deviation in Q-factors is attributed to the different measurement methods as the electrical circuit influences the electrically measured Q-factor. In a small signal approximation, the piezoelectric layer or the Wheatstone bridge may be short-circuit by the voltage sources at the resonance frequency.

ϕ_{start}	Q_{mech}	Q_{el}
-90	8746	4328
-60	8016	3372
-30	7048	2843
0	5533	2299

Tab. 6.1: The table shows the Q-factors which are obtained by optical and electrical measurement methods. A frequency-dependent, phase-shifted stimulus is applied at the MEMS cantilever.

6.2 Measurement system: STM32

The results of the previous chapter prove the concept of the phase shift approach. There, a frequency generator delivers pure sine wave signals. In this section, these sine signals are replaced by pulse-pause (PP) signals from a STM32 microcontroller. The analog signal from the piezoelectric layer of the Wheatstone bridge *ΔU* is recorded by the STM32 to provide a closed-loop feedback driven alternation of the excitation signal. Hence, a further development of this approach enables a miniaturisation of the excitation and measurement setup which then can be located close to the cantilever. The software of the STM32 controls the amplification board and provides a USB interface for data exchange.

6.2.1 System description

An STM32 (32F429I-DISCOVERY Board) evaluation board is used to set up the measurement system. Based on the microcontroller board headers, a tailored PCB provides the signal amplifiers for cantilever actuation and oscillation measurement. In Fig. 6.11 two measurement principles are sketched. In (a)

the direct measurement with the pulse-pause method is shown. During the pulse period, the cantilever is excited and during the pause period the voltage at the piezoelectric layer is measured. In (b), the enhanced measurement setup captures and processes the voltage difference ΔU of the Wheatstone bridge.
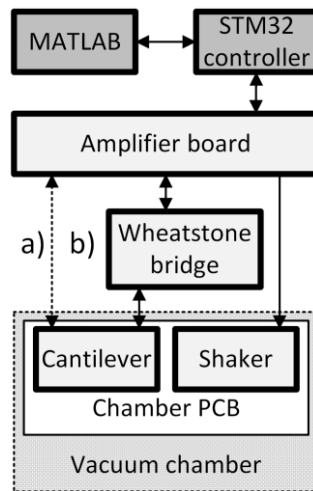
Fig. 6.11: The schematic functional block diagram shows the STM32 measurement setup. The option (a) shows the initially wiring between the amplifier board and the cantilever and (b) shows the changed setup with a Wheatstone bridge.

The MATLAB script configures the STM32. The amplifier board, which is shown in Fig. 6.12 (a), amplifies the PP signals for the cantilever- and shaker excitation and offers BNC connections for additional measurement and excitation equipment. The vacuum chamber houses the chamber PCB, the shaker and the cantilever, which is shown in Fig. 6.12 (b).
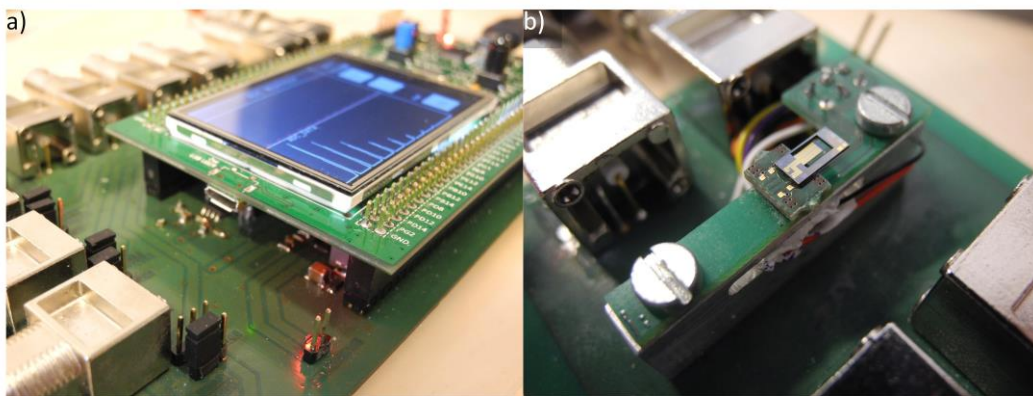
Fig. 6.12: (a) The image shows the controller board and amplifier board which are placed outside of the vacuum chamber. (b) The image shows the shaker, cantilever and PCB, which is fixed inside the vacuum chamber.

When the STM32 controller is set in local operation mode, the menu consists of the items, which are shown in Fig. 6.13. Here, every value can be set manually to test the cantilever and the shaker independently.
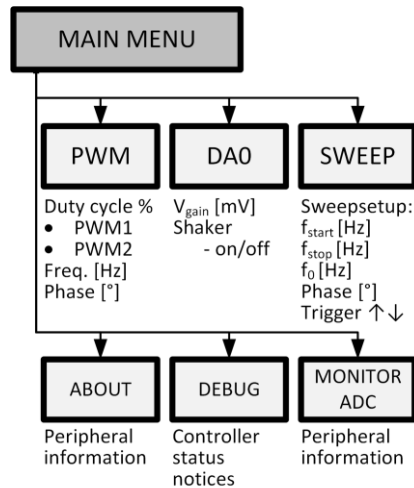
Fig. 6.13: The control menu structure of the local operation mode is illustrated.

6.2.2 Schematic sketch and circuit diagram

The amplifier board consists of five main sections, which are shown in Fig. 6.14 (a). The instrument and adjustable amplifiers increase the ΔU of the Wheatstone bridge, while the cantilever and shaker amplifiers boost the driving signals from the STM32 to excite the cantilever and the shaker. The power supply provides a dual voltage of +/-5 V for all amplifiers. In Fig. 6.14 (b), the connections of the amplifier board, the signal path (red arrows), the layout of the amplifier board itself and the microcontroller board are shown schematically. The amplifier board offers the routing from the cantilever signal to the oscilloscope (BNC01) and to the STM32. The frequency generator or the STM32 can supply the PP signal for the driving circuit. The analysis of the mounted cantilever is possible by the CON01 connector or by placing the cantilever in the vacuum chamber.
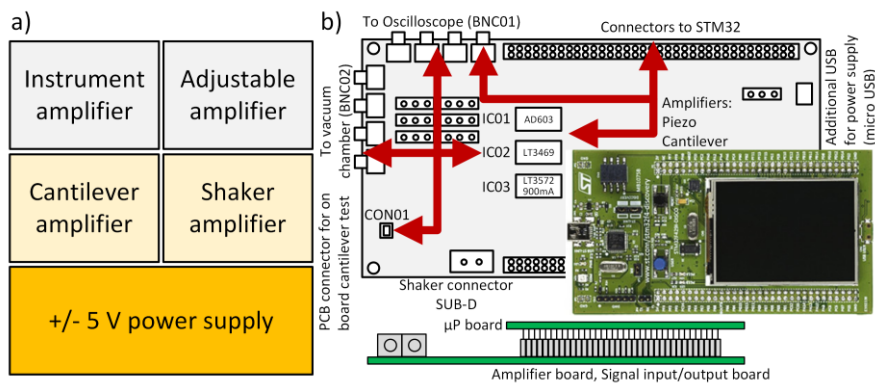
Fig. 6.14: (a) The functional block diagram of the amplifier board is shown. (b) The schematic sketch displays the components, connection and signal flow of STM32 measurement system.

The amplifier board consists of two piezo drivers from Analog Devices. The LT3469 is a "Piezo Microactuator Driver with boost Regulator", which stimulates the piezoelectric layer at the cantilever (Fig. 6.15 (a)). The chip has a frequency range up to 1.3 MHz, while offering a driving voltage up to V_{CC} = 35 V and a maximum current of 40 mA. The LT37572 (Fig. 6.15 (b)) drives the shaker piezo, which is a "Dual Full-Bridge Piezo Driver with 900mA Boost Converter". This device is capable of powering piezos with up to 40 V from a 5 V power supply and it has a high current output with a current limit up to 900 mA. The voltage, which is generated by the cantilever oscillation, is pre-amplified with the AD8422 (Fig. 6.15 (c)). It has a low nose input of maximum 8 nV/√Hz and a variable gain range from 1 to 1000. Then, the AD603, which is a "Low Noise, 90 MHz Variable Gain Amplifier" (Fig. 6.15 (d)), is

used as a two-stage amplifier, where the differential voltage is adjusted to the input level of the STM32. The STM32 is able to adjust the gain with a D/A output.
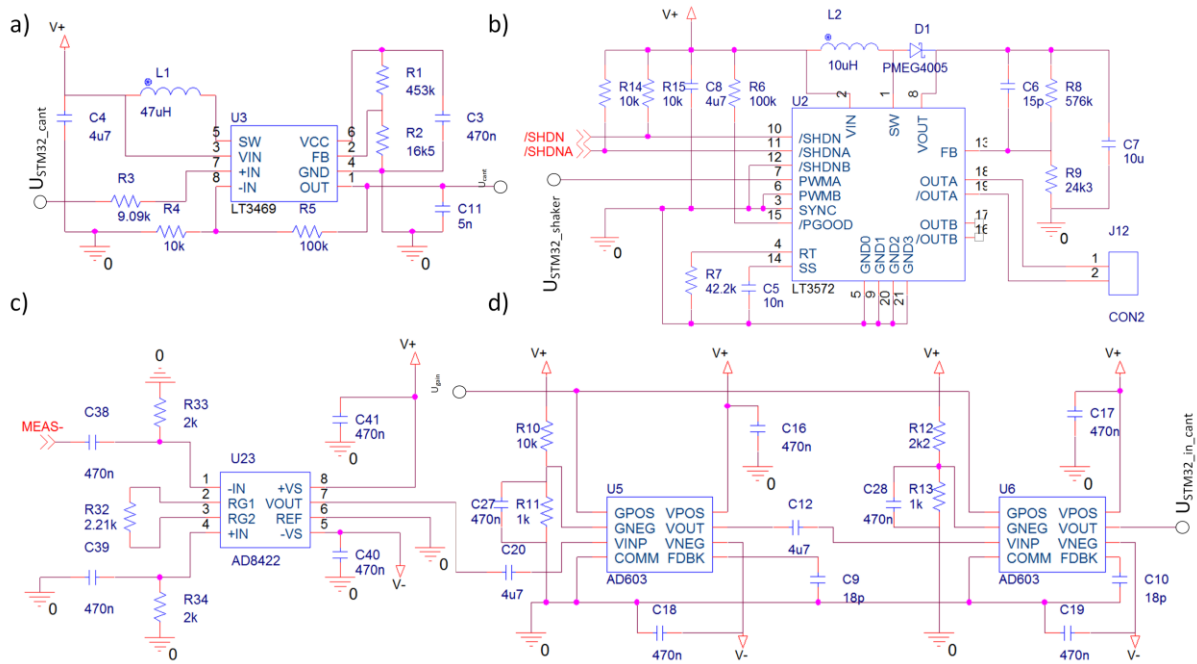
Fig. 6.15: The image shows the circuit schematics of (a) power amplifier of cantilever oscillation excitation, (b) power amplifier of shaker oscillation excitation, (c) cantilever voltage amplifier and (d) variable gain two-stage cantilever voltage amplifier.

6.2.3 Verification of analog input and output signals

Two PP signals, which are varied from 0.1 to 99 % PP r1atio and 0 to 360° phase shift, are generated by the STM32. The PCB board amplifies the two channels and routes the signals to the cantilever and to the piezo shaker. The diagrams in Fig. 6.16 show the voltage curve of the amplified PPs after the amplifier step. In Fig. 6.16 (a), the STM32 drives the shaker amplifier with 10 kHz and a PP of 50 % and 5 %. The diagrams show a rectangular output signal, where the amplitudes reach the maximum voltage of 12 V. At a frequency of 100 kHz, the rising slope effects the rectangular shape of the output signal, which is shown in Fig. 6.16 (b). By reducing the PP to 5 %, the slope limit affects the maximum output level, which has then a maximum amplitude of only 3.5 V. The shaker excitation chip drives a high load application, which in fact reduces the bandwidth. Apart from that, in Fig. 6.16 (c) the phase shift operation with a phase shift between shaker (orange line) and cantilever (blue line) is shown.
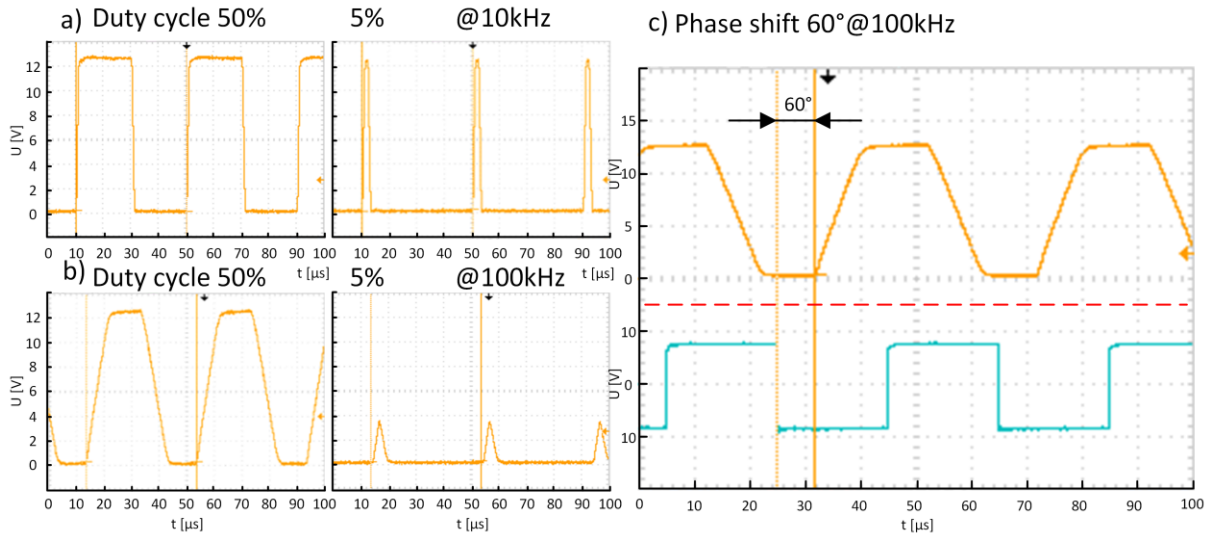
Fig. 6.16: The duty cycle signal of the shaker amplifier without load of 50% PP and 5% PP at (a) 10 kHz and (b) 50 kHz is shown. At figure (c), the phase-shift of 60 ° between cantilever and shaker oscillation excitation with 50 % PP is shown.

The cantilever oscillation amplitude can be determined by measuring the voltage of the piezoelectric layer. To utilize the resolution of the STM32 A/D-converter, the voltage at the input pin has to be as large as possible. Therefore, the variable gain amplifier increases the voltage up to the input limit of the STM32. The gain is set by an adjustable voltage, which can be changed with an integrated D/A of the STM32. The Fig. 6.17 displays the linear relationship between voltage and gain. This allows an exact correlation between measured value at the STM32 and voltage at the cantilever.
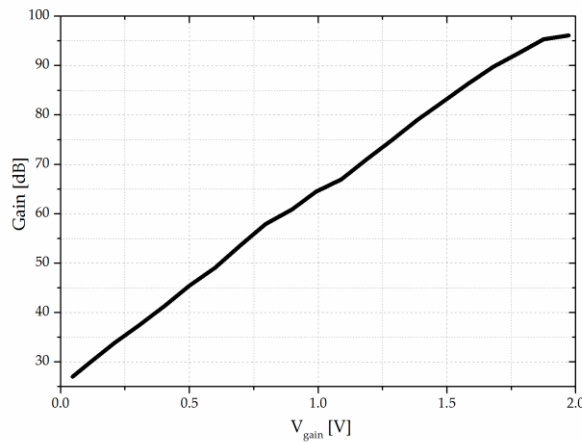
Fig. 6.17: The diagram shows the characteristic curve of cantilever voltage gain.

6.2.4   Circuit diagram design changes

After verification, the circuit design has two drawbacks. First, the measurement circuit cannot recognize the cantilever oscillation signal, while the actuation signal supplies the cantilever at the same time. The intended design of measuring the impulse of the excitation voltage, which stimulates the oscillation of the cantilever and measuring the voltage peak during the off time, where the voltage peak of the piezoelectric layer occurs, was not feasible. Even when the gain is adjusted during on and off phase of the PP-signal, the amplitude range difference of the excitation and piezoelectric voltage is too large. To overcome this issue, a Wheatstone bridge with adjustable resistors and capacitors was introduced. The Wheatstone bridge, which is shown in Fig. 6.11 (b), supplies the actuated cantilever and measures the differential voltage by comparing the two legs of the bridge circuit. The differential voltage is measured and amplified with the differential instrumentation amplifier, which is shown in

Fig. 6.18 (a). The second improvement prohibits saturation or damage of the input of the STM32 in the event of a too large gain voltage at the variable gain amplifier. An additional Z-diode limits the input voltage to 4 V, which is shown in Fig. 6.18 (b).
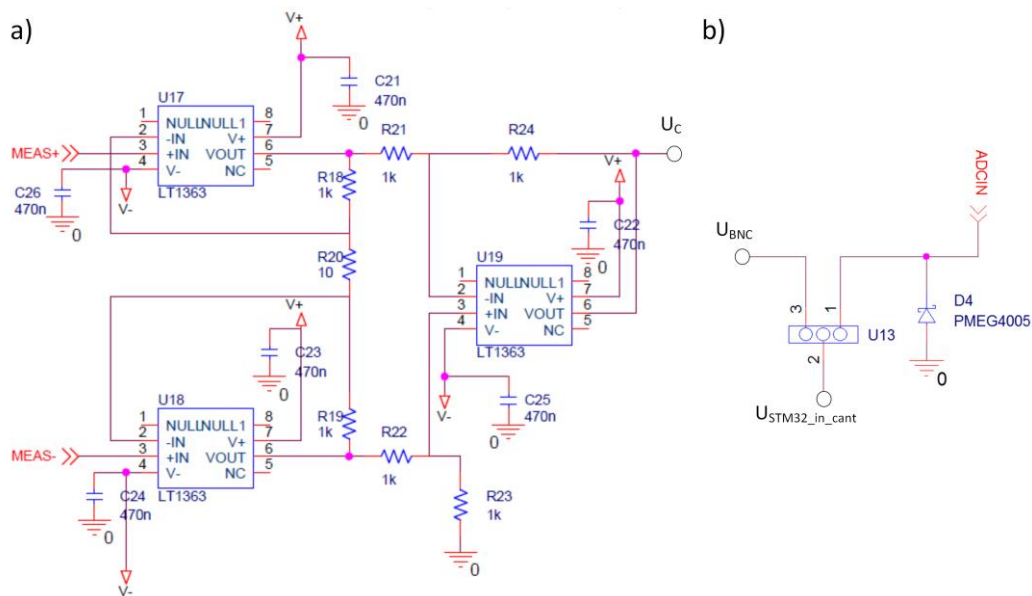
Fig. 6.18: The differential instrumentation amplifier for Wheatstone bridge for + and - signal path is shown at (a). The input voltage limiter prevents the saturation of the STM32 analog input at (b).

6.2.5 Variable phase deflection applied to a MEMS cantilever in the frequency domain

In Fig. 6.19 (a), the results of the frequency dependent phase shift between cantilever and shaker actuation are shown. The principle of adjusting the phase is shown in Fig. 6.5 in the previous section. Here, the microcontroller samples the signal with 1 MHz, which results in a width of 25 sample points for every bar. The amount of frequency steps is limited to 20 because of the memory limitation of the microcontroller. The diagram presents the captured signal of a starting phase of 0 °, 45 °, 90 ° and 180 ° in a normalized frequency spectrum. The black line shows the amplitude spectrum of ϕ_{start} = 0 °, where the resonance peak of the cantilever is difficult to recognise. By increasing ϕ_{start} to 45 °, the visibility of the resonance behaviour in the spectrum is enhanced, which becomes even more pronounced with further enlargement. The appearance of the curve at resonance depends on the amplification or damping of the mechanical vibration through the electrical manipulation at resonance. To be able to compare this process with other methods, the maximum at each data point in the spectrum was plotted on a graph and interpolated with a line, shown in Fig. 6.19 (b).
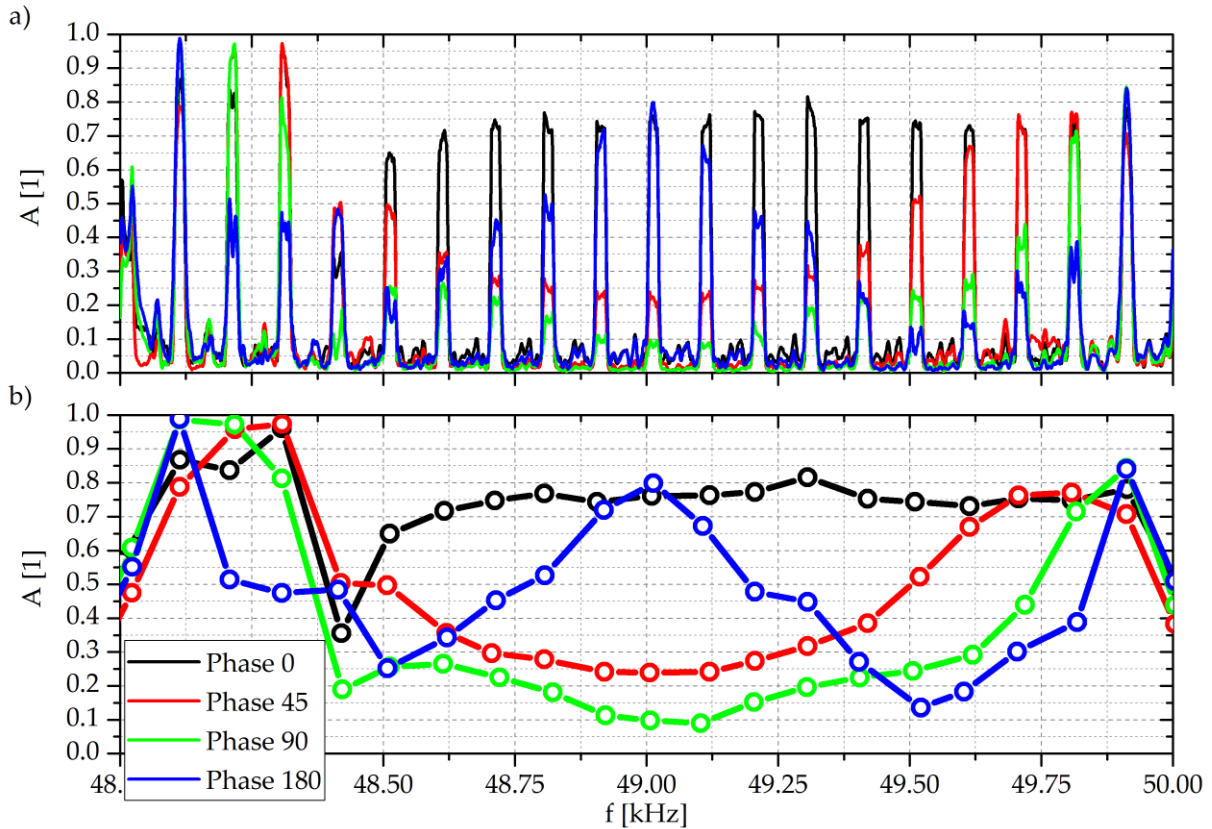
Fig. 6.19: The figure shows a normalized frequency spectrum of differential voltage of the Wheatstone bridge (a). The maximum amplitude at each sampling point results in the figure (b).

To extract the Q-factor for all ϕ_{start}, the bathtub curves given in Fig. 6.19 (b) have to be inverted. When doing so, the Q-factors can be calculated from the fit of the frequency spectrum, shown in Fig. 6.20. The Lorentz fit is applied to the curves in Fig. 6.20 (a) (black curve) and in Fig. 6.20 (b) (blue curve) to determine the Q-factors for the phase shift of 0 ° and 180 °. When knowing the circuit-depended characteristics, the inverse curves are shown in Fig. 6.20 (a) (red curve) and in Fig. 6.20 (b) (green curve), where the Q-factors are determined in the same way as before.
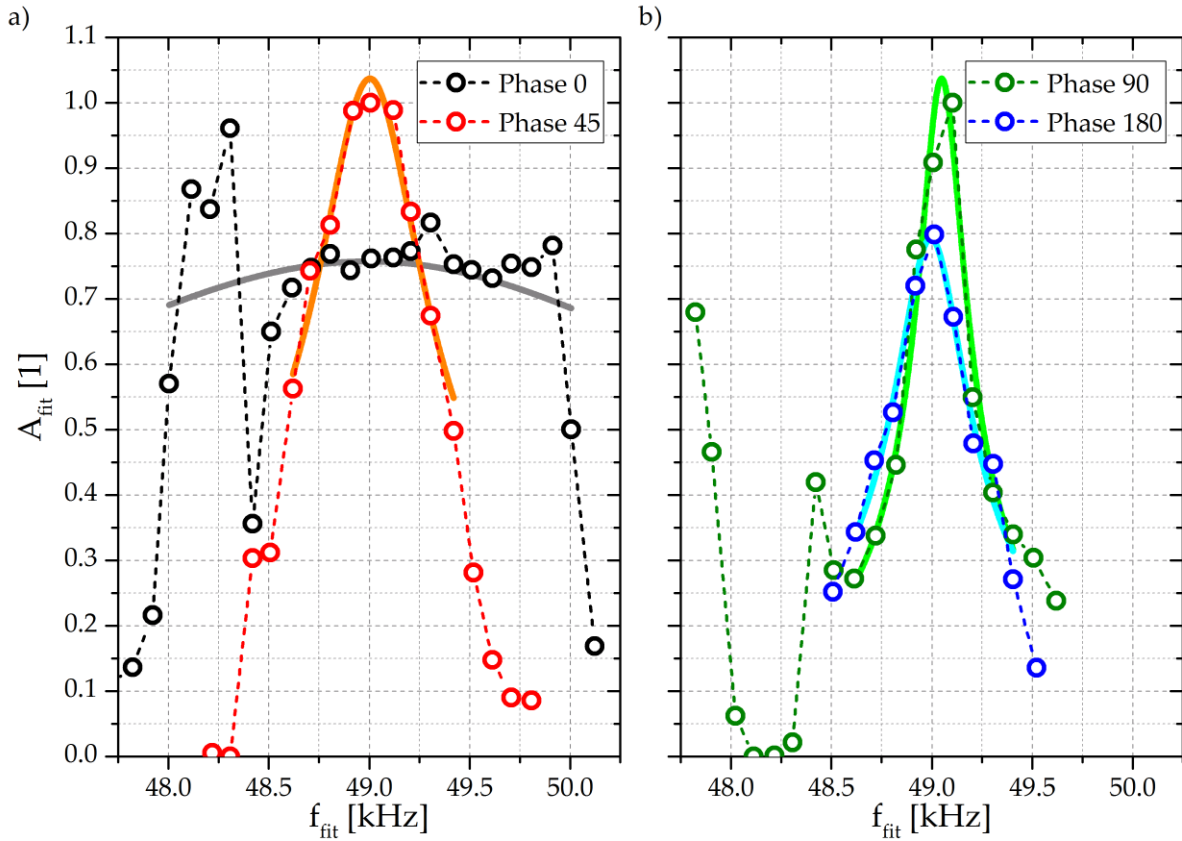
Fig. 6.20: The Q-factor is calculated with the Lorentz fit of the maximum amplitude extraction (a) of $\phi_{start} = 0$ and 45 and (b) o$\phi_{start} = 90$ and 180.

The results of the Lorentz fit are presented in Fig. 6.21, which shows the impact of the phase shift on the Q-factor. Through the presentation in list form, in Tab. 6.2, the exact values of the identified Q-factors reveal a reduction by a factor of 15. The Q-factor increases from 11 at phase 0° to 165 at phase 90° and drops to 138 at phase 180°.
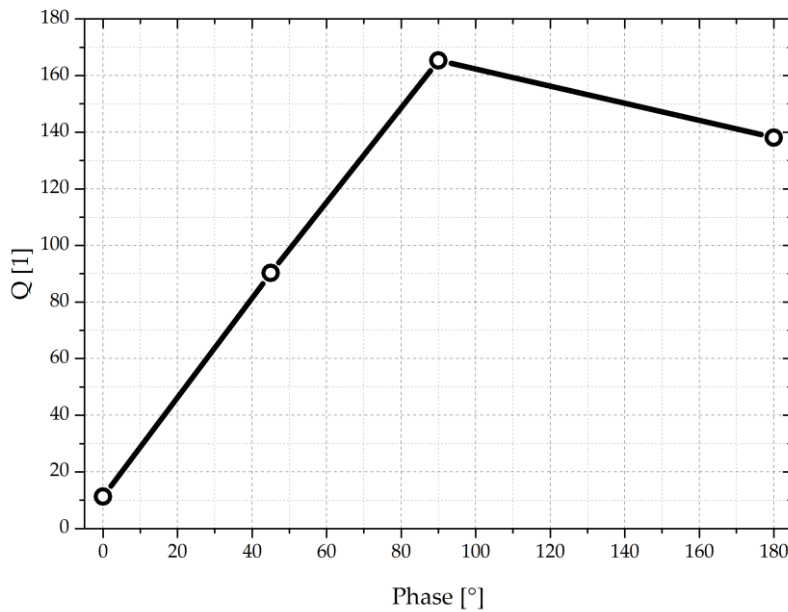
Fig. 6.21: The diagram shows the Q-factor manipulation of a STM32 setup. The microcontroller applies a frequency-dependent, phase-shifted stimulus to the MEMS cantilever.

ϕ_{start}	Q
0	11
45	90
90	165
180	138

Tab. 6.2: The table shows the Q-factors which are obtained by electrical measurements. The STM32 applies a frequency-dependent, phase-shifted stimulus to the MEMS cantilever.

In comparison to other methods of determining the Q-factor, the Q-factors, which are found here, are unrealistic low. Nevertheless, the Q-factor changes through the change of ϕ_{Start}, but this can be caused by an artefact of the pulse-pause excitation. The comparison of plot ϕ_{Start} = 90 ° and ϕ_{Start} = 180 ° in Fig. 6.19, support this hypothesis. The different directions of the curves are noticeable, which is not expected without changing the DUT or the wiring. In the section 6.1.4, the working principle of the Q-factor manipulation through a mechanical superposition with sinusoidal excitation signals was confirmed, as it can be seen in Tab. 6.1. To transfer this principle to a microcontroller approach, a closer look to the excitation with rectangle signals and the acquiring of the ΔU at the Wheatstone bridge has to be done to improve this approach.

6.3 Measurement System: Mixer and Lock-In

The approaches introduced in the previous sections allow to manipulate the Q-factor by superposition of two mechanical oscillations. The mixer and Lock-In approach on the other hand, manipulates the excitation voltage through a feedback loop. With an integrated piezoelectric layer, simultaneous excitation and acquisition of the cantilever oscillation [41] are possible. Here, the frequency-dependent adjustment of the excitation voltage manipulates the Q-factor [42] by decreasing the excitation voltage at the resonance frequency [43, 44]. To prove the impact of the active damping, the Q-factors are computed from the frequency spectra, which are created by various feedback gain levels. With the series resonant circuit model and the Lorentz curve fit, the mechanical Q-factor is extracted from the electrically and optically measured frequency spectrum. A realistic assessment of the manipulation of the Q-factor is revealed at the end of the chapter, where the response of the cantilever oscillation is investigated when excited by a step function.

6.3.1 System description

The measurement principle is shown in Fig. 6.22 (a). There, a supply voltage U_C drives a piezoelectric layer, which excites the cantilever oscillation. The cantilever movement is measured with a LDV. To measure the Q-factor of a free moving cantilever, the sample surface should be far away (d_{CS} = approx. 3 µm) from the cantilever, so that the surface has no influence on the cantilever oscillation which is tested through a variation of the excitation voltage of the shaker piezo.

The measurement equipment is separated into the control component, the signal conditioning, which is located in the vacuum chamber and the feedback loop (Fig. 6.22 (b)). The main component of the feedback loop is the Lock-In amplifier from Zurich Instruments (HF2LI). It provides the oscillation voltage U_{AC}, which is fed into a mixer stage. The output of the mixer is applied to both the cantilever and the compensation circuit via an additional fully differential OP amplifier. The compensation structure has exactly the same geometrical dimensions as the released cantilever. By driving the compensation structure with the inverted cantilever signal, the current resulting from both the parallel resistance R_P and parallel capacity C_P is cancelled. The I/U-converter ($\frac{U_o}{I_C} = R_{IU}k_U = -10^6\Omega$) transforms the compensated current into the voltage U_C. Via electrical feedthrough in the vacuum

chamber, the signal is transferred to the Lock-In amplifier. The real part of the electrical signal is extracted, multiplied with the proportional factor k_{fb} and used as feedback signal U_{fb} to reduce the DC voltage U_{in} from the channel 1 (CH1) of the FGEN. The use of U_{in} prevents nonlinearities at low input signal voltages and sets the working point at the mixer. CH2 of FGEN is used to generate the square wave signal (U_S), which is amplified and fed into the piezo (Piezomechanik, PSt 150/5x5/7). It raises and lowers a silicon sample surface with a frequency of 1 Hz, thus changing the distance between the cantilever and the substrate surface, a microscaled change in sample topography during AFM operation should be mimicked. To avoid any issues through the mechanical movement of the piezo (sample surface), the falling edge characteristic is used to evaluate the step response. The measurements start with an approached surface and the surface is moved away from the cantilever. At the Lock-In amplifier, the strength of the feedback k_{fb} is varied between 0 and 20. To confirm the electrical measurement of the cantilever movement, the mechanical velocity signal is measured simultaneously by an LDV through the optical port at the top of the vacuum chamber. Both signals, cantilever voltage and cantilever velocity, are synchronized by the oscillator and recorded with the lock-in amplifier for further evaluation.
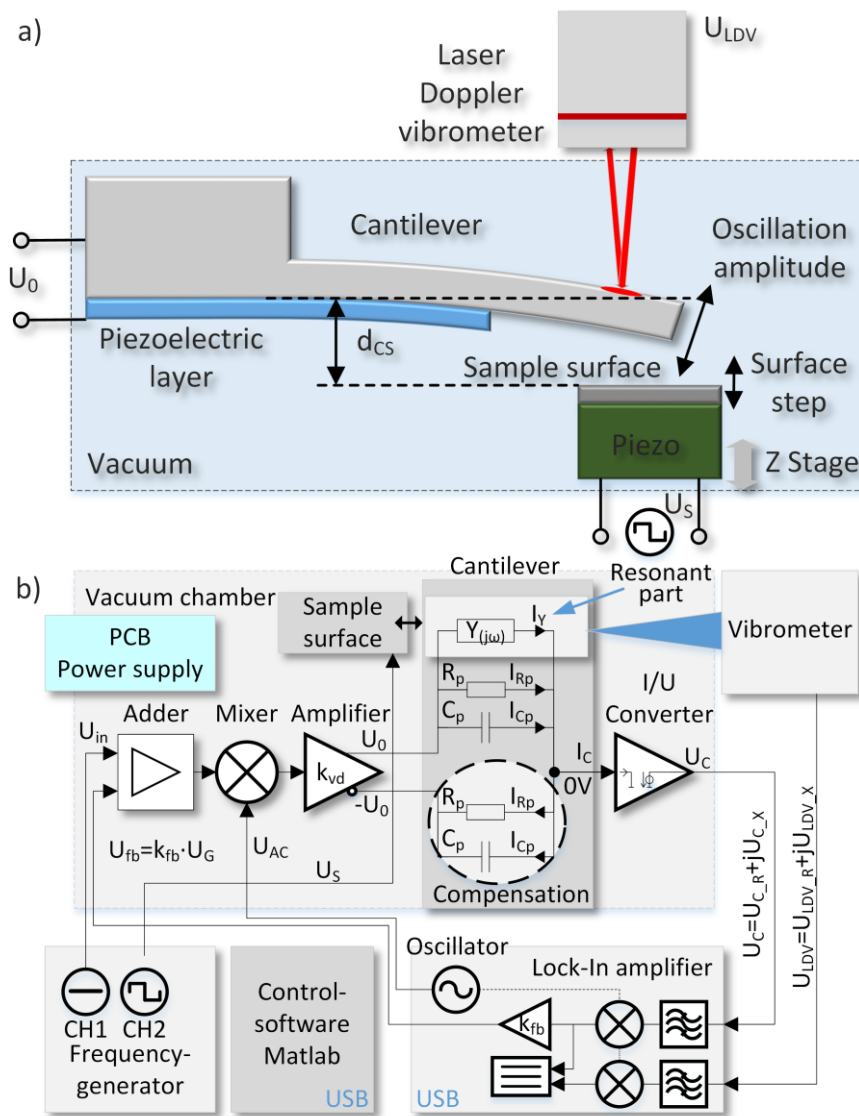
Fig. 6.22: The schematic shows the principle layout of piezoelectric driven cantilever in vacuum with an electrical readout and an optical readout (a). The measurement setup consists of a frequency generator, Lock-In amplifier and laser Doppler vibrometer, which is operated at atmospheric pressure. The signal preparation and signal capturing is located in the vacuum chamber (b).

6.3.2 Cantilever operation under vacuum environment

The experiments are carried out with an actively actuated oscillating cantilever and a non-oscillating compensation structure with the same geometrical dimensions as the released cantilever. The cantilever (Fig. 6.23 (a)) is placed into a vacuum chamber with a pressure of 10^{-5} mbar and an optical window to acquire the mechanical vibration with the LDV (shown in Fig. 6.23 (b)).
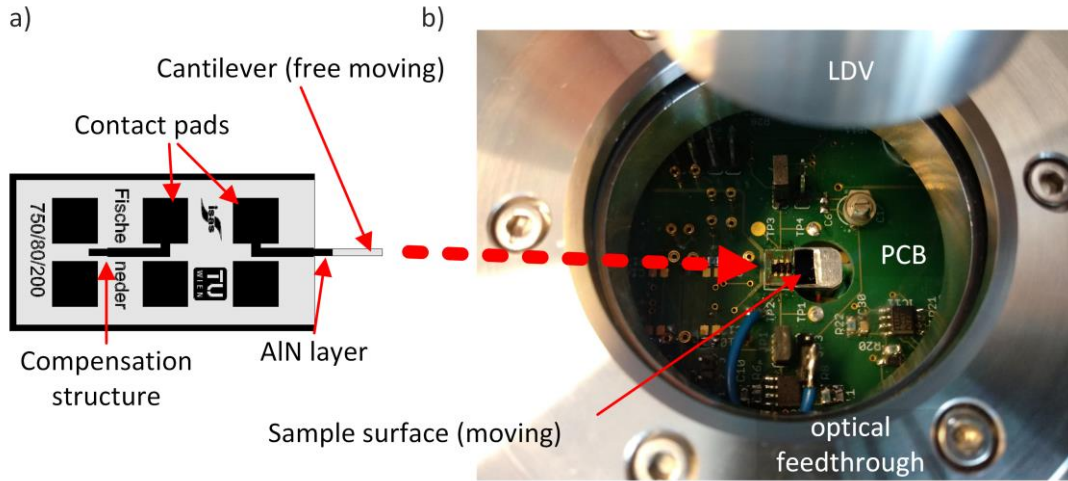
Fig. 6.23: The schematic shows the top view of the cantilever, which includes the free moving cantilever, the compensation structure and the contact pads (a). The photograph shows the PCB and the cantilever, which are placed in the vacuum chamber (b).

6.3.3 Optically and electrically determined Q-factors

While the cantilever is excited, the Lock-In amplifier records the vibrations optically via the LDV (2.3.3) and electrically via I/U-converter (see schematic in Fig. 6.22). The optically measured cantilever oscillation velocity frequency spectrum is plotted and the curves are fitted by the Lorentz equation [68]. The cantilever amplitude spectrum is given in (6.1). The LDV measures the cantilever velocity spectrum $U_{vLDV}(f) = g_{LDV} \cdot U_{LDV}(f)$, where the voltage of the LDV is multiplied by $g_{LDV} = 50\text{mm/s/V}$. At (6.1) the frequency is expressed by f, the resonance frequency by f_0, the voltage amplitude by U_0 and the Q-factor by Q_{LDV}.

$$U_{LDV}(f) = \frac{U_0}{\sqrt{\left(1 - \left(\frac{f}{f_0}\right)^2\right)^2 + \left(\frac{1}{Q_{LDV}}\frac{f}{f_0}\right)^2}}$$

(6.1)

Additionally, the information of the Q-factor is measured electrically. Therefore, the resonance of the mechanical beam is interpreted as an electrical RLC circuit, which is described in (6.2). The impedance spectrum $Z_{RLC}(f)$ characterizes the frequency f depended part of the cantilever. When looking at the schematic of the measurement setup in Fig. 6.22, the cantilever already has a compensated structure included. As a consequence, the parasitic capacitor C_p and the parasitic resistor R_p are already compensated by the identical non-moving part. Nonetheless, there are intolerances in fabrication and driving amplifier, which supplies the nominal voltage U_0 and $-U_0$ to the piezoelectric layers (*i.e.* on the cantilever and at the compensation structure). Those parameters are listed as the mismatch resistor R_{pm}, mismatch inductor L_{pm} and mismatch capacitor C_{pm} in (6.3) and result in $Z_{AlN}(f)$, which is the impedance of the compensated AlN layer. The current through the AlN layer I_C is driven by the amplifier voltage U_0 and amplified by the transimpedance amplifier (TIA) $Z_{TIA} = R_{IU}k_U$ to $U_{AlN}(f)$ in (6.4). In addition, the DC component U_Δ and the phase shift φ of the amplifier and the I/U converter

has to be considered in (6.5). The fitting of the voltage spectrum is done with $U_C(f)$, thereby all parameters can be determined. The electrically measured Q-factor Q_{RLC} is calculated through (6.6) [44].

$$Z_{RLC}(f) = R + j \cdot 2\pi \cdot f \cdot L + \frac{1}{j \cdot 2\pi \cdot f \cdot C} \qquad (6.2)$$

$$Z_{AlN}(f) = \frac{1}{\frac{1}{Z_{RLC}} + \frac{1}{R_{pm}} + \frac{1}{j \cdot 2\pi \cdot f \cdot L_{pm}} + j \cdot 2\pi \cdot f \cdot C_{pm}} \qquad (6.3)$$

$$U_{AlN}(f) = -Z_{TIA} \cdot \frac{U_0}{Z_{AlN}(f)} \qquad (6.4)$$

$$U_C(f) = \left| U_{AlN}(f) \cdot e^{-j\varphi} + U_\Delta \right| \qquad (6.5)$$

$$Q_{RLC} = \frac{1}{R}\sqrt{\frac{L}{C}} \qquad (6.6)$$

6.3.4   Mixer and Lock-In: Q-control measurement result

When applying a frequency within a range of 47.5 kHz to 48.3 kHz at the Lock-In amplifier, a voltage spectrum U_{LDVair} of the cantilever velocity can be recorded with the LDV. In Fig. 6.24 (a), the U_{LDVair} shows the spectrum in air, where the feedback k_{fb} is gradually increased from 0 to 20. The maximum feedback reduces the voltage peak by -6.4 dBV compared to no manipulation. The cut-out shows the excellent agreement between the measured U_{LDVair} and the fitted Lorentz equation (6.1) for a k_{fb} of 0, 5, 10 and 20. By increasing the feedback, the Q-factor can be reduced from 1000 to 600, which is noted in Tab. 6.3. Besides the U_{LDVair}, the phase φ_{LDVair} of the velocity is shown in Fig. 6.24 (b), the real part U_{LDV_Rair} and the imaginary part U_{LDV_Xair} are plotted in Fig. 6.24 (c) and in Fig. 6.24 (d). The cantilever shows a strong resonance behaviour (a), which can be reduced by increasing k_{fb}. At U_{LDVair} lower than -15 dBV, the curves in the diagram become wavy, because the resolution limit of the selected LDV measuring range is reached. As it can be seen in (b), the phase profile is not affected by the strength of the k_{fb}.
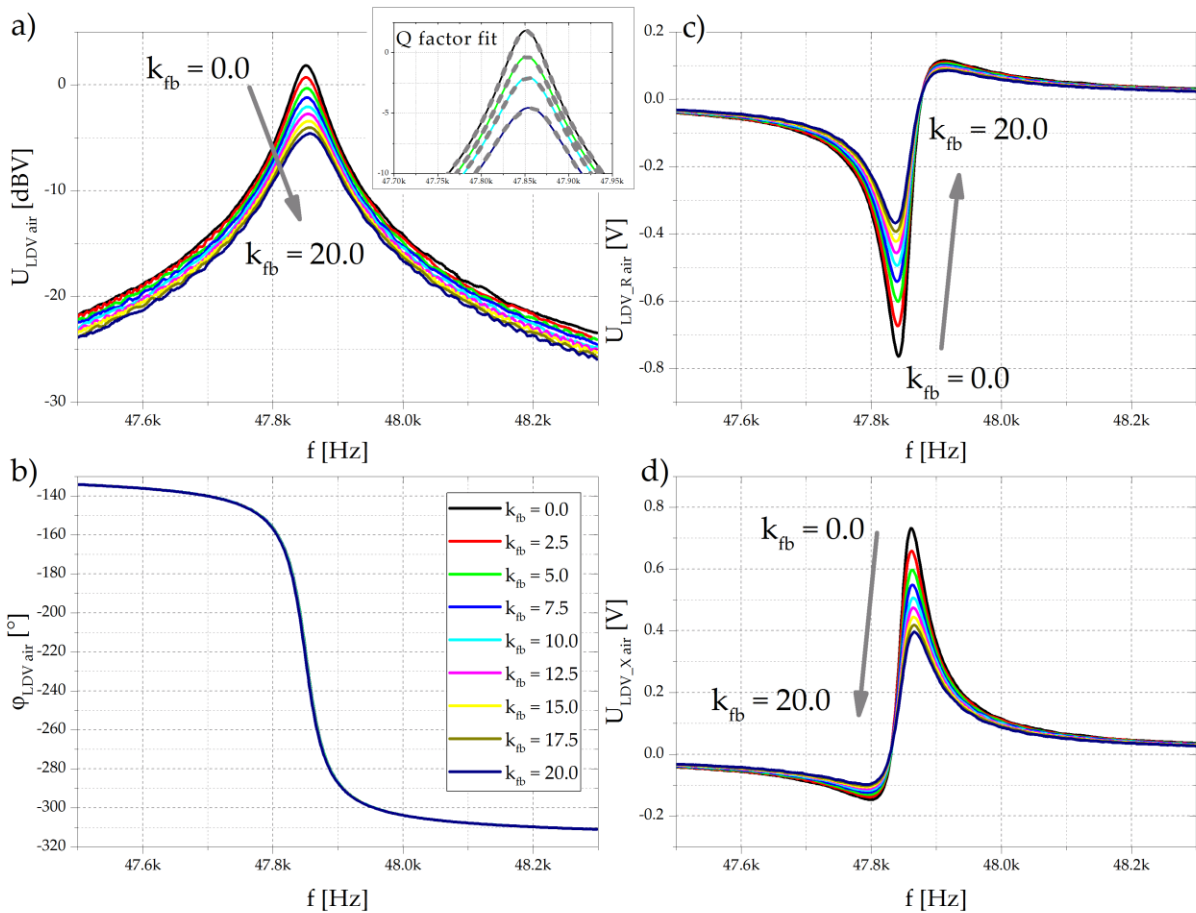
Fig. 6.24: The cantilever velocity is recorded with the LDV in air with a gradually increased feedback k_{fb}, whereas in (a) the amplitude, in (b) the phase, in (c) the real part and in (d) the imaginary part are illustrated.

Simultaneous, the U_{Cair} spectrum is recorded, which is proportional to the current through the piezoelectric layer at the cantilever. Through the constant voltage supply U_0, the mechanical resonance is interpreted through a RLC circuit, as it is stated in (6.2). The corresponding frequency spectrum is shown in Fig. 6.25 (a). An increase k_{fb} causes a reduction of the difference between the maximum and the minimum of U_{Cair} of -6.1 dBV. Moreover, the phase φ_{LDVair} is shown in Fig. 6.25 (b), the real part of the cantilever voltage U_{C_Rair} and the imaginary part U_{C_Xair} are shown in Fig. 6.25 (c) and in Fig. 6.25 (d). If these results are compared with those from the previous figure Fig. 6.24, a difference in curve shape becomes apparent at resonance. Due to the electrical interpretation of the mechanical resonance by R, L and C, the curve shape changes, as shown in Fig. 6.25. The cut-out in (a) illustrates the excellent match of RLC series resonant circuit from (6.5) with the measurement data. This allows a Q-factor calculation for each k_{fb} and comparison of the results between the electrically and optically measured Q-factors, as it is shown in Tab. 6.3. The Q-factors obtained from both methods show excellent agreement, indicating that the optical measurement can be replaced by the electrical measurement.

83
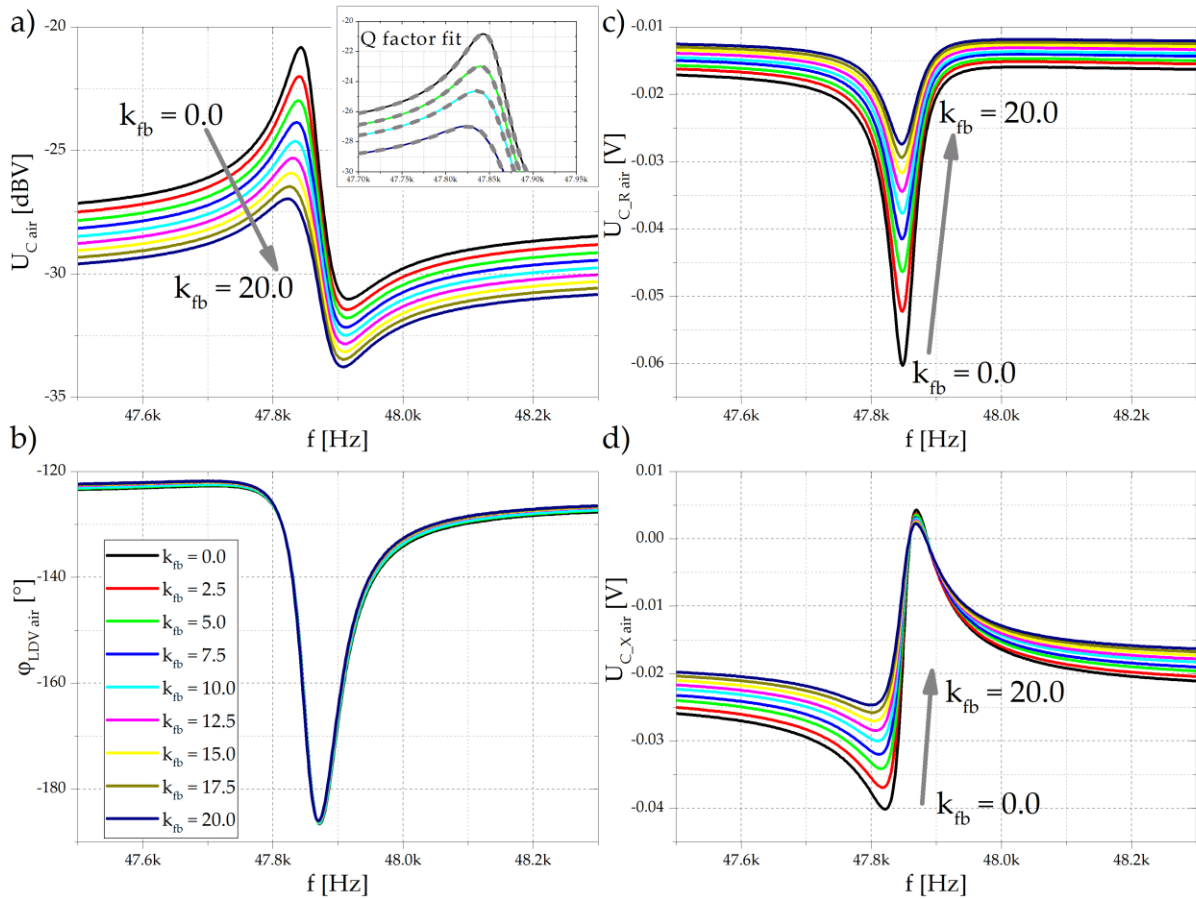
Fig. 6.25: The diagrams show the voltage of the transimpedance amplifier, which a cantilever in air with gradually increased feedback k_{fb}. In (a) the amplitude, in (b) the phase, in (c) the real part and in (d) the imaginary part are illustrated.

After evacuation of the vacuum chamber, the cantilever velocity is recorded by the LDV. The absence of air damping increases the Q-factor from 1000 to 5200. By gradually increasing k_{fb} from 0 to 20, the cantilever velocity voltage from the LDV U_{LDVvac} is reduced by -11.8 dBV, as it is shown in Fig. 6.26 (a). By fitting the Lorentz curve (6.1), which is shown in the cut-out, the Q-factor reduces from 5200 to 1400, which is noted in Tab. 6.3. The fitting demonstrates the strong correspondence between the measurement and the Lorentz curve. Nevertheless, the bump at large k_{fb} near the resonance deviates from the fitting curve. This dent is exactly at the same frequency at which the real part of U_{C_Rvac} has the maximum (see Fig. 6.27 (c)). Due to the large feedback k_{fb}, the real part is amplified very strongly, which results in an elimination of the excitation by driving the mixer into saturation. Beside that, the associated phase φ_{LDVvac}, the real part of the cantilever movement U_{LDV_Rvac} and the imaginary part U_{LDV_Xvac} are plotted in Fig. 6.26 (b), in Fig. 6.26 (c) and in Fig. 6.26 (d), respectively.

84
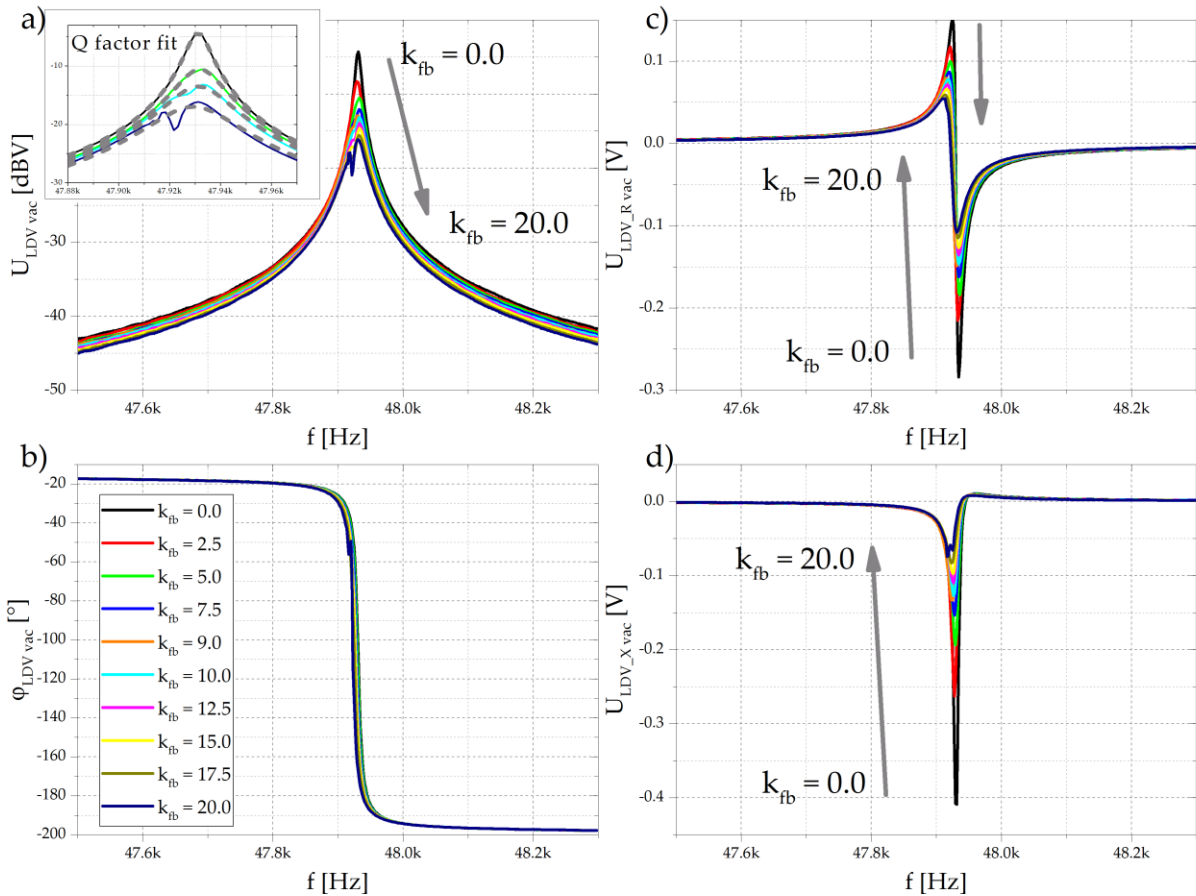
Fig. 6.26: The cantilever velocity is recorded with the LDV under vacuum with a gradually increased feedback k_{fb}. In (a) the amplitude, in (b) the phase, in (c) the real part and in (d) the imaginary part are illustrated.

Due to the absence of air damping in vacuum, not only the optically measured resonance peak sharpens in comparison to measurements in air, the same is true for the electrically measured resonance spectrum U_{Cvac}. This goes along with an increase in Q-factor from 1000 in air to 5300 in vacuum. When k_{fb} is gradually increased from 0 to 20, the amplitude undergoes a reduction of -12.7 dBV, which can be seen in Fig. 6.27 (a). The cut-out in the diagram demonstrates the accuracy of RLC circuit fitting from (6.5), where the Q-factor is reduced from 5300 down to 1400 by a k_{fb} of 20. The findings of the Q-factors with the corresponding k_{fb} are noted in Tab. 6.3. The bump near the resonance frequency is more obvious, because U_{Cvac} is recorded directly, without mechanical mass inertia from the cantilever. The phase φ_{Cvac} of U_{Cvac} is shown in Fig. 6.27 (b), while the real part U_{C_Rvac} and the imaginary part U_{C_Xvac} are given in Fig. 6.27 (c) and in Fig. 6.27 (d).
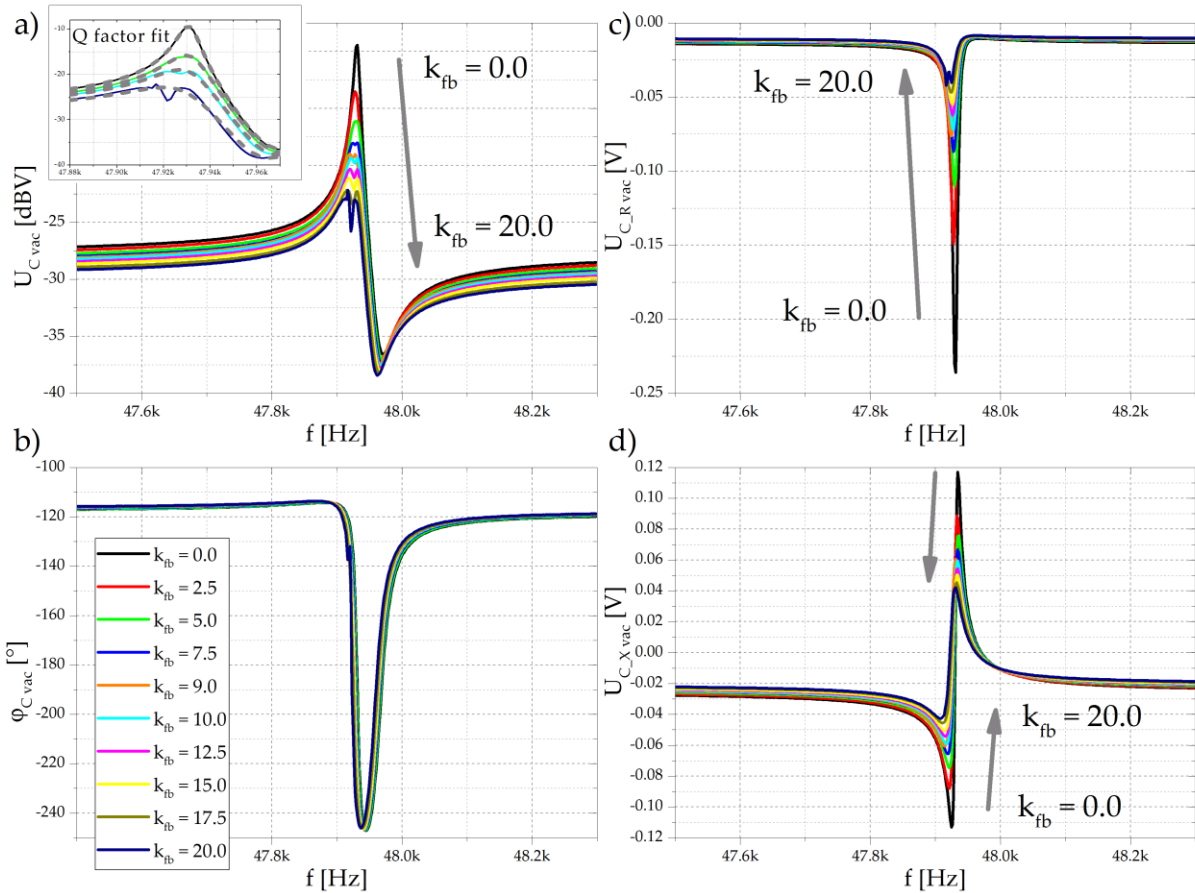
Fig. 6.27: The diagrams show the current from the piezoelectric transducer integrated on the cantilever amplified with a transimpedance amplifier in vacuum with a gradually increased feedback k_{fb}. In (a) the amplitude, in (b) the phase, in (c) the real part and in (d) the imaginary part are illustrated.

To demonstrate the impact of k_{fb} on the Q-factor in the time domain, the impact on the response time t is investigated. The response time is defined as the falling time between the normalized amplitude values 0.9 and 0.1, therefore, the measurement values are scaled from 1 to 0. This approach was used, because the feedback has only a proportional part but no integral part and the oscillation of the envelope of the step response will not be damped in vacuum at large k_{fb}. Therefore, the characterization through the ring down method, where $x = \hat{x} \cdot e^{-\frac{t}{\tau}}$ is fitted and the Q-factor can be calculated by $\tau = \frac{2Q}{\omega_0}$ is not possible.

The step is generated by applying a square wave signal at CH2, which simulateds a step-like surface feature affecting the oscillating cantilever during AFM operation. This mimics a strong change in the average interaction force between oscillating cantilever and sample surface. In air, Fig. 6.28 (a) and Fig. 6.28 (b) show the time behaviour of the oscillation amplitude recorded both electrically and optically and plotted by U_{Cair} and U_{LDVair}. In vacuum, the response time is increased, which is plotted with U_{Cvac} and U_{LDVvac} in Fig. 6.28 (c) and in Fig. 6.28 (d), respectively.
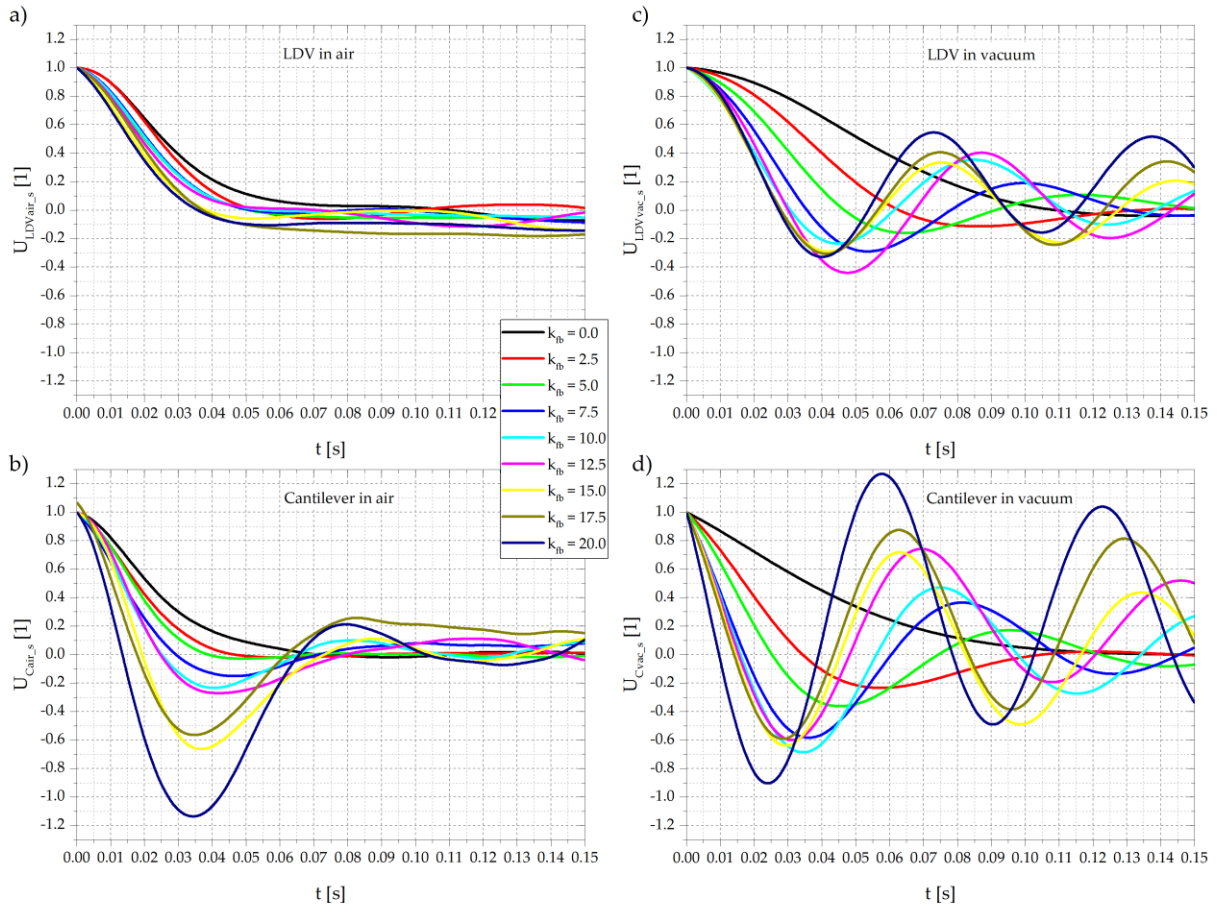
Fig. 6.28: The step response diagram shows U_{Cair} (a) and U_{LDVair} (b) in air and U_{Cvac} (c) and U_{LDVvac} (d) in vacuum.

By increasing the feedback k_{fb}, the Q-factors and the response times in air (t_{LDVair}, t_{Cair}) and in vacuum (t_{LDVvac}, t_{Cvac}) are reduced effectively, what is summarized in Tab. 6.3. In vacuum, the effect of increasing k_{fb} is even more evident due to the absence of air damping. Comparing the results of the lowest $k_{fb} = 0$ with the largest $k_{fb} = 20$, the optical measured Q-factors Q_{LDVair} are reduced by a factor of 1.62 and the optical measured response times t_{LDVair} are reduced by a factor of 1.67. Similar observations are made with respect to the optically measured Q-factors Q_{LDVvac} and optically measured response times t_{LDVvac}. Specifically, the Q-factor is reduced by a factor of 3.55, and the response time is reduced by a factor of 3.83. The electrically measured response time t_{Cair} is reduced by a factor of 4.22 in air and the t_{Cvac} is reduced by a factor of 10.13 in vacuum. The deviation $\Delta Q_{error}[\%] = \frac{Q_C - Q_{LDV}}{Q_C} \cdot 100$ between the electrically determined Q-factor Q_{LDV} and the optically determined Q-factor Q_C gives an error for air and vacuum which is lower than 2.1% for a k_{fb} up to 10. Through increasing the k_{fb} up to 20, the error increases to, however, a maximum of less than 9%. The significant larger values for the response time and the latter increase of deviation of larger k_{fb} might betraced back to the fact, that the feedback amplifies the real part U_{C_R} and k_{fb} is a proportional amplification without an integral part.

k_{fb}	Q_{LDVair}	Q_{Cair}	Q_{LDVvac}	Q_{Cvac}	t_{LDVair}	t_{Cair}	t_{LDVvac}	t_{Cvac}
1	1	1	1	1	ms	ms	ms	ms
0.0	1014	1036	5236	5320	42.11	41.14	69.21	76.02
2.5	923	937	3404	3455	32.24	29.46	41.69	25.85
5.0	851	862	2668	2686	32.10	25.15	32.10	19.18
7.5	795	799	2246	2230	31.69	21.26	24.88	13.34
10.0	747	749	1987	1948	31.69	17.65	22.24	12.37
12.5	711	706	1820	1759	30.71	16.40	20.43	11.81
15.0	679	669	1705	1625	26.40	12.79	19.59	10.98
17.5	648	638	1568	1462	25.71	11.81	19.18	10.84
20.0	627	611	1476	1355	25.15	9.73	18.07	7.50

Tab. 6.3: The table shows the Q-factors and response times t, which are determined in air and in vacuum.

6.3.5 Effectivity of Q-control

In Fig. 6.29 (a), the black and red lines represent the Q-factor in vacuum, depending on k_{fb}. In contrast, the Q-factor reduction at ambient pressure is plotted with grey lines. Additionally, the response times are presented in Fig. 6.29 (b), where the black and red lines indicate the vacuum environment and the grey lines the air environment.
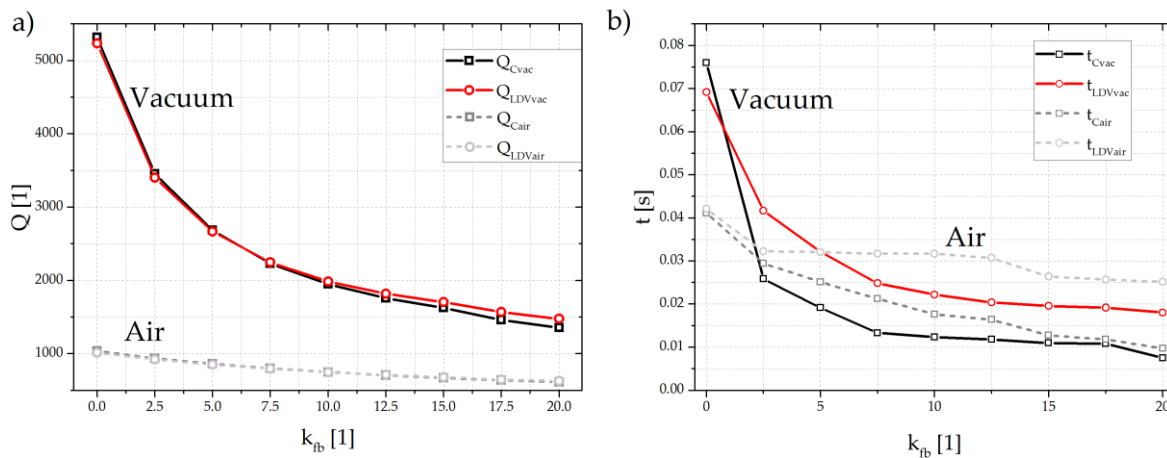
Fig. 6.29: (a) The diagram shows the Q-factor with the gradually increased k_{fb} in vacuum as well as in air. At (b) the response time reduction is drawn.

The curves in Fig. 6.29 clearly show the effect of k_{fb} on the Q-factor (Q_{LDV}, Q_C) and on the response time (t_C, t_{LDV}) in air and in vacuum. Despite this findings, there is a difference in reaction of Q-factor and response time to the change of k_{fb} which is attributed to the determination of the reaction time. As described in the latter chapter, typically the ring down method is used. Here, this is not applicable, because only a proportional gain (k_{fb}) is provided by the Lock-In amplifier. Even at moderate k_{fb} of 7.5 the feedback has the tendency to introduce electronic instability into the feedback-loop, which is evident at $k_{fb} = 20$, where the oscillation is not damped. Therefore, the falling time (time between 0.9 and 0.1 of the amplitude) is used to determine the response time.

6.4 Summary

This chapter presents three approaches for electronically manipulating the Q-factor of piezoelectric MEMS cantilevers. This is made possible due to the integration of piezoelectric thin film transducers within the cantilevers.

The first approach, based on a FGEN and an oscilloscope, uses the piezoelectric thin film actuator as serial element in a Wheatstone bridge configuration. Applying a constant phase shift between the two actuators, here between the shaker and the cantilever, the Q-factor remains constant. But, by an active phase manipulation of the supply voltage for the Wheatstone bridge, a frequency depended manipulation of the cantilever deflection is possible. Through the variable phase shift, the Q-factor reduces under vacuum from 8746 to 5533, which is a factor of 1.6, by changing the starting phase from -90 ° to 0 °. It is demonstrated that the superposition of mechanical oscillations, which are provided from two different, independent sources, can be used for an active Q-factor control when a frequency dependent phase shift is enabled.

The phase shift approach is transferred to a microcontroller (STM32) approach. The sinusoidal excitation was changed to a rectangular pulse-pause approach, which is easier to implement in a microcontroller. The evaluation reveals an unrealistic low Q-factor, which may put down to a measurement artefact of the rectangular excitation.

The third approach uses an electrical feedback loop to reduce the excitation voltage for piezoelectric actuated cantilevers. For this purpose, a variable gain feedback is designed to reduce the response time of the oscillation amplitude in vacuum. The approach features a Lock-In amplifier, which extracts the real part of the piezoelectric-induced current. By using the auxiliary output, the analog signal reduces the excitation voltage via an analog mixing circuit. Thereby, a reduction of the Q-factor by a factor of 4, from initially 5200 (with no feedback) to 1450 (with maximum feedback) under vacuum is shown. The corresponding step response decreases from 69 ms to 18 ms, which is comparable with the response time in air.

7   Conclusions and Outlook

Two types of microscopes, SEM and AFM, have great importance for surface analysis. Combining these two techniques, the new device will bring new challenges like vacuum environment, equipment size and characteristic response times, which in turn affects the measurement duration. Especially when AFM cantilevers are placed inside the vacuum chamber of a SEM, the lack of air damping substantially increases the response time of the cantilever. This work primarily focused on the major reason of the prolonged response time which was the increased Q-factor when operating a cantilever in vacuum. Two major approaches were discussed to manipulate the Q-factor. The superposition of oscillations which were stimulated by the tapping piezo of an AFM and by an actively excited piezoelectric layer integrated on the AFM cantilever. The second approach was a setup with a Lock-In amplifier, which manipulated the excitation of the piezoelectric thin film layer.

For both approaches, a cantilever with an integrated piezoelectric layer was fabricated. The main focus was the repeatable deposition of the AlN layers, which had been shown through the deposition over a 5 weeks period with a thickness of 0.5 µm, 1.0 µm and 2.0 µm. The use of a self-tailored wafer holder reduced the maximal temperature of the wafer below 100 °C (0.5 µm), 135 °C (1.0 µm) and 145 °C (2.0 µm) and the layer stress of the thin films remained compressive for all samples, with values of -0.45 GPa (0.5 µm), -0.3 GPa (1.0 µm) and -0.1 GPa (2.0 µm) . Even more, the layer thickness influenced the layer stress value. Further evaluation of the AlN layers revealed that the non-etchable residues remained at the surface with an area of 0.4 µm^2 to 0.5 µm^2, thus demonstrating a different microstructure. These results were published in [145]. To enhance the reproducibility of the layer's electrical and piezoelectric properties, the clamped sample holder enhanced the AlN (002) crystal orientation by a factor of 1.8 compared to the standard sample holder, allowing a free movement of the wafer. This was reflected in the larger piezoelectric coefficient d_{33}, which was approximately -6.8 pC/N compared to -5 pC/N for the standard sample holder. Through leakage current measurements, a Poole Frenkel behaviour of the charge carriers was found. The barrier height ϕ_B was determined to 0.62 eV (0.5 µm), 0.66 eV (1.0 µm) and 0.68 eV (2.0 µm) and the activation energy E_A resulted in -0.56 eV (0.5 µm), -0.60 eV (1.0 µm) and -0.58 eV (2.0 µm). In comparison to the standard holder, where ϕ_B was 0.78 eV (0.5 µm) and 0.63 eV (2.0 µm), and E_A was -0.68 eV (0.5 µm) and -0.63 eV (2.0 µm), a reduction of the scattering of ϕ_B and E_A was observed and the results were published in [144].

Through the improved AlN deposition process, a significant reduction of fabrication steps was achieved. The fabrication process duration was reduced from about 4 weeks to less than one week. In addition, the AlN lift-off processes and the self-aligned layer fabrication prevented short circuits between top- and bottom electrodes. Up to this point, the use of a lift-off process with organic photoresist was not feasible because of heat-induced degeneration of the resin during deposition. Therefore, the clamped sample holder was used to reduce the deposition temperature of the wafer to a maximum of 145°C for an AlN layer thickness of 2.0 µm. At an AlN thickness of 1.0 µm, the maximum deposition temperature stayed below 135°C which made the use of the organic resin as lift-off mask possible. It is worth mentioning, that one mask was used for the piezoelectric AlN layer and for the top electrode.

The cantilever dimensions were defined by COMSOL® simulations. The impact of geometric dimension of the cantilever, of the electrodes and of the active piezoelectric layer on the resonance frequency and on the Q-factor was examined. The oscillation amplitude of the cantilever was manipulated by adjusting the phase between the oscillation excitation of the shaker and the piezoelectric layer at the cantilever. It was shown, that destructive superposition helped to reduce the oscillation amplitude, but the Q-factor did not change through a constant phase shift. A frequency dependent phase shift between the shaker and the piezoelectric layer widened or narrowed the resonance peak width.

Through continuous phase adaptation, a noticeable reduction of the Q-factor was attained. At a piezoelectric layer length of 200 µm, a reduction of more than 60 % was achieved. Through the use of a piezoelectric length of 100 µm, the Q-factor was reduced by nearly 80%.

With the optimal geometrical dimensions of the cantilever and its piezoelectric layer, the design phase was initiated. A set of four masks was designed for the fabrication, which contained the mask for the contact pads, the piezoelectric layer and the front and backside Bosch etch. The cantilever had a width of 20 µm to 320 µm and a length of 100 µm to 1000 µm. The piezoelectric layer had a length of 100 µm to 500 µm and the width covers the whole width of the cantilever with a clearance of 3 µm among each layer.

The cantilevers were fabricated with two 4" SOI wafers with a Si thickness of 3 µm and 20 µm and 1 µm buried oxide. The bottom electrode had a low device resistance of 0.06 Ω·cm. Through the use of the improved AlN structuring process, the yield of working cantilevers resulted in over 60 % per wafer.

By superposition of the oscillation generated by the shaker and the oscillation induced by the piezoelectric layer, it was possible to manipulate the Q-factor. The results were transferred to a micro-controller (µC) solution, which might be placed next to the cantilever for minimal signal losses. A combined circuit board for the lab measurement equipment approach and for the microprocessor approach was designed. It included variable gain amplifiers, signal drivers and printed circuit board (PCB) connectors for the direct cantilever connection. A PCB for mounting of the cantilever itself and the bonding wires were manufactured. For the application in the vacuum chamber, an additional PCB was used as the mounting plate and the electrical connection.

A two-channel frequency generator excited the oscillations of the shaker and the cantilever. The signal at one channel was amplified and sent to the shaker, while the other channel directly drove the cantilever via a Wheatstone bridge. The differential voltage was proportional to the oscillation amplitude and after amplification, an oscillation amplitude comparison between the electrically measured oscillation (oscilloscope) and the optically measured oscillation (laser Doppler vibrometer) was done. When normalized, the recorded frequency spectrum showed a constant Q-factor with a constant phase-shift. A frequency depending phase shift widened the resonance spectrum, which manipulated the Q-factor. Thereby, a reduction of the optically measured Q-factor from 8746 to 5533 and of the electrically measured Q-factor from 4328 to 2299 was realized. The deviation between mechanical and electrical Q-factor was explained through the use of the Wheatstone bridge. These results have been published in [154].

Through the success of this approach, a STM32F4 controller (STM32F429I-DISCOVERY) was used to replace the two channels of the frequency generator with two pulse-pause signals from the µC. The signal from the first channel was amplified by a power piezo driver to drive the shaker. The signal from the second channel was amplified by a signal amplifier to drive the cantilever. The µC approach offered additional features like resonance frequency recognition, adaptive amplification, automatic calibration and simple interface to the existing AFM. In this setup, the adjustable amplification with a two-stage amplifier (AD603) for the logging of the differential signal was used mainly. The evaluation of the frequency spectrums resulted in a Q-factor change from 165 to 11. Despite the generally low Q-factor, which may arise from the rectangular stimulation of the cantilever and shaker and the FFT calculation of the microcontroller, the proof of concept was shown.

The second approach was designed with a Lock-In amplifier to replace the established AFM configurations. The principle of excitation voltage manipulation, which was shown in literature for magnifying the Q-factor in liquids, was used to damp the oscillation instead. The current, which is manipulated by the piezoelectric layer of the cantilever, was used as a feedback signal for the adjustment of excitation voltage. First results showed an inacceptable drift of the signal due to a

dramatic dependence on the temperature of the cantilever. The design of an improved cantilever layout with an additional unreleased compensation structure resulted in a significant reduction of the temperature dependence. At ambient pressure, the Q-factor showed a value of approx. 1000, either determined via electric measurement or via optical measurement. By increasing the feedback, the Q-factor was reduced by 40 % to approx. 600. The effect was much more dominant in vacuum. A gradual increase of the feedback strength lowered the Q-factor from 5200 to 1400. This was a reduction of more than 70 % and the Q-factor under vacuum approximated to the Q-factor in ambient pressure.

The impact on the dynamics of the cantilever was simulated with a moved Si plate. The step response was defined as the time between 90 % and 10 % of the oscillation amplitude. Between no and maximum feedback the response time reduced from 42 ms to 25 ms when it was measured optically and from 41 ms to 10 ms when it was measured electrically. Under vacuum, the optical step response time was reduced from 70 ms to 18 ms and the electrical response time was reduced from 76 ms to 7.5 ms.

With this results in mind, the working principle of the active damping was confirmed. Either the concept of superposition of oscillations from two different sources or the closed-loop feedback of a piezoelectric driven cantilever opened a wide range of applications. Through an application specific integrated circuit (ASIC) approach, an integration of both the read-out and feedback electronics on the sensor chip will be feasible. Noteworthy, this approach might be used as an easy-to implement add-on to existing AFMs. The latter approach also eliminated the precise excitation of the shaker piezo in an AFM, which had to be designed carefully to avoid any unwanted resonances. Due to the integrated piezoelectric transducer element, the cantilever served as oscillation excitation element, which was controlled by a feedback loop. Especially the miniaturisation by avoiding bulky components showed a huge potential for the application in advanced surface analysing tools often operated under vacuum.

8 Nomenclature

AFM .... Atomic force microscopy

Al .... Aluminium

AlN .... Aluminium nitrite

Ar .... Argon

Au .... Gold

BB .... Bragg-Brentano

BNC .... Bayonet Neill–Concelman connector

Bot El .... Bottom electrode

BOX .... Buried oxide

CMOS Complementary metal-oxide-semicond.

Cr .... Chromium

CVD .... Chemical vapour deposition

DC .... Direct current

DIP .... Dual inline package

DOE .... Design of experiment

DSO .... Digital storage oscilloscope

DUT .... Device under test

EDX .... Energy-dispersive X-ray spectroscopy

FEM .... Finite element method

FGEN .... Frequency generator

FWHM .... Full width half maximum

H_3PO_4 .... Phosphoric acid

HF .... Hydrofluoric Acid

ISE .... Inverse sputter etching

ISO .... Isopropanol

LDV .... Laser Doppler vibrometer

LPCVD .... Low pressure CVD

MBE .... Molecular beam epitaxy

MEMS .... Micro electro-mechanical systems

Mo .... Molybdenum

N .... Nitrogen

PCB .... Printed circuit board

PECVD .... Plasma enhanced CVD

PF .... Poole-Frenkel

PLD .... Pulsed laser deposition

PP .... Pulse-pause

PVD .... Physical vapour deposition

PZT .... Lead zirconate titanate

SEM .... Scanning electron microscopy

Si_3N_4 .... Silicon nitride

SOI .... Silicon on insulator

SUB-D .... D-Subminiature

Ti .... Titan

TIA .... Transimpedance amplifier

Top El .... Top electrode

UHV .... Ultra-high vacuum

UV .... Ultraviolet

XRD .... X-ray diffraction

ZnO .... Zinc oxide

9 List of Symbols

$\overline{\overline{A}}_{>0.95}$ .... Average area week 1..5 [m^2]

A .... Sample area [m^2]

$\bar{A}_{>0.95}$ ..... Significant area (Avg. largest 5%) [m^2]

A_C .... Centre of interval [m^2]

A_I .. Total area of residues of a specific size [m^2]

B .... Bandwidth [Hz]

B .... Susceptance [S]

$B_{0.293}$ .... -3dB transmission bandwidth [Hz]

$B_{0.707}$ .... -3dB cut-off bandwidth [Hz]

c .... Elastic stiffness [Pa]

C .... Capacitance [F]

C_p .... Specific heat capacity [J/(kg·K)]

C_P .... Parallel capacitance [F]

C_{pm} .... Capacitor mismatch [F]

d .... Piezoelectric coefficient [C/N]

D .... Electric displacement [As/m^2]

d_{31} ... Transversal piezoelectric coefficient [C/N]

d_{33} . Longitudinal piezoelectric coefficient [C/N]

d_{CS} .... Cantilever sample distance [m]

d_{lat} .... Latter distance [m]

e .... Piezoelectric constant [m/V]

e .... Emissivity [1]

E .... Electrical field [V/m]

E .... Modulus of elasticity [Pa]

E_A .... Activation energy [eV]

f .... Frequency [Hz]

f_0 .... Resonance frequency [Hz]

f_H .... Upper -3 dB frequency [Hz]

f_L .... Lower -3 dB frequency [Hz]

f_r .... Resonance frequency [Hz]

G .... Conductance [S]

g_{LDV} .... LDV voltage multiplier [1]

h_{AlN} .... Piezoelectric layer thickness [m]

h_{Au} .... Top electrode thickness [m]

h_{Si} .... Cantilever thickness [m]

I_C .... Cantilever supply current [A]

J .... Current density [A/m^2]

k .... Boltzmann constant [J/K]

k_{fb} .... Proportional factor [1]

k_U .... Amplification factor TIA [1]

l .... Sample length [m]

L .... Inductance [H]

l_{AlN} .... Piezoelectric layer length [m]

L_{pm} .... Inductor mismatch [H]

l_{Si} .... Cantilever length [m]

n .... Integer multiple [1]

N_I .... Quantity of residues per interval [1]

P .... Radiated power [W]

P_{AlN} .... AlN deposition power [W]

P_{ISE} .... ISE power [W]

q .... Elementary charge [C]

Q .... Quality factor [1]

Q_C .... Q-factor cantilever [1]

Q_{Cair} .... Q-factor cantilever air [1]

Q_{clamp} .... Clamping losses [1]

Q_{Cvac} .... Q-factor cantilever vacuum [1]

Q_{LDV} .... LDV quality factor [1]

Q_{LDVair} .... Q-factor LDV air [1]

$Q_{surface}$ .... Surface losses [1]

Q_{TED} .... Thermoelastic damping [1]

R .... Resistor [Ω]

R_{IU} .... Feedback resistor [Ω]

R_P .... Parallel resistance [Ω]

R_{pm} .... Resistor mismatch [Ω]

s .... Elastic compliance [1/Pa]

S .... Mechanical strain [1]

t .... Time [s]

T .... Temperature [K]

T .... Mechanical stress [Pa]

t_{AlN} .... AlN deposition time [s]

t_C ....Response time cantilever [s]

T_C .... Environment temperature [K]

t_{Cair} .... Response time cantilever air [s]

t_{Cvac} ....Response time cantilever vacuum [s]

t_{ISE} ....ISE deposition duration [s]

t_{LDV} .... Response time LDV [s]

t_{LDVair} ....Response time LDV air [s]

t_{LDVvac} .... Response time LDV vacuum [s]

T_m ....Peak temperature [° C]

T_o ....Equilibrium temperature [K]

U_0 .... Cantilever supply voltage [V]

U_0 ....Oscillation amplitude [V]

U_{AC} .... Oscillation voltage [V]

U_C ....Amplified cantilever voltage [V]

U_{C_R} .... Real voltage of cantilever [V]

U_{C_Rair} .... Real voltage of cantilever in air [V]

U_{C_Rvac} .... Real voltage of cantilever vacuum [V]

U_{C_Xair} ....Imag. voltage of cantilever in air [V]

U_{C_Xvac} . Imag. voltage of cantilever vacuum [V]

U_{Cair} ....Voltage cantilever in air [V]

U_{Cvac} .... Voltage cantilever vacuum [V]

U_E .... Envelope voltage [V]

U_{fb} ....Feedback voltage [V]

U_{in} .... Linearity voltage [V]

U_{LDV} ....Cantilever velocity voltage [V]

U_{LDV_Rair} ....Voltage real LDV air [V]

U_{LDV_Rvac} .... Voltage real LDV vacuum [V]

U_{LDV_Xair} ....Voltage imag. LDV air [V]

U_{LDV_Xvac} ....Voltage imag.l LDV vacuum [V]

U_{LDVair} .... Voltage LDV in air [V]

U_{LDVvac} ....Voltage LDV vacuum [V]

U_S .... Square wave voltage [V]

U_{vLDV} .... Cantilever velocity spectrum [mm/s]

w_{Si} .... Beam width [m]

Z_{AlN} ....Impedance AlN [Ω]

Z_{RLC} ....RLC impedance spectrum [Ω]

Z_{TIA} .... Impdance TIA [Ω]

$α$ .... Thermal expansion coefficient [m/K]

$α_{AlN}$ ... Thermal expansion coefficient AlN [m/K]

$α_{Si}$ .... Thermal expansion coefficient Si [m/K]

$γ$ .... Damping coefficient [1/s]

$ΔQ_{error}$ ....Q-factor cantilever LDV error [%]

$ΔT$ .... Temperature difference [K]

$ε$ ....Permittivity [Am/(Vs)]

$ε_0$ ....Electric constant [As/Vm]

$ε_C$ .... Young's modulus [Pa]

$ε_r$ .... Relative permittivity [1]

$ζ$ ....Damping ratio [1]

$ϑ$ .... Angle of incidence [°]

$κ_{th}$ .... Thermal conductivity [W/(m·K)]

$λ$ .... Wavelength [m]

$λ_{Al}$ .... Thermal conductivity Al [W/(mK)]

$λ_{Mo}$ .... Thermal conductivity Mo [W/(mK)]

$ρ_C$ .... Density [kg/m²]

$σ$ ....Stefan-Boltzmann constant [W/(m²·s)]

$σ$ ....Film stress [Pa]

$τ$ ....Response time [s]

$φ$ ....Phase shift [°]

$ϕ_B$ ....Barrier height [eV]

$ϕ_{deflection}$ ....Deflection phase [°]

$φ_{LDVair}$ .... Phase of velocity air [°]

$φ_{LDVvac}$ .... Phase of velocity air [°]

$ϕ_{start}$ .... Start phase [°]

$ω$ .... Angular frequency [1/s]

$ω_0$ .... Resonance angular frequency [1/s]

10 List of Figures

11 List of tables

12 References

[1]   J. Sanderson, *Understanding Light Microscopy*. Wiley, 2019.

[2]   R. Heiderhoff and L. J. Balk, *Scanning Probe Microscopy – History, Background, and State of the Art*. Wiley, 2012.

[3]   M. Knoll and E. Ruska, "Das Elektronenmikroskop", *Zeitschrift für Physik,* vol. 78, pp. 318-339, 1932.

[4]   E. Ruska, "über Fortschritte im Bau und in der Leistung des magnetischen Elektronenmikroskops", *Zeitschrift für Physik,* vol. 87, pp. 580-602, 1934.

[5]   L. Marton, "Electron Microscopy of Biological Objects", *Physical Review,* vol. 46, pp. 527-528, 1934.

[6]   J. W. Menter, "The direct study by electron microscopy of crystal lattices and their imperfections", *Philosophical Magazine,* vol. 86, pp. 4529-4552, 2006.

[7]   M. Haider, S. Uhlemann, E. Schwan, H. Rose, B. Kabius, and K. Urban, "Electron microscopy image enhanced", *Nature,* vol. 392, pp. 768-769, 1998.

[8]   G. Binnig, C. F. Quate, and C. Gerber, "Atomic Force Microscope", *Physical Review Letters,* vol. 56, pp. 930-933, 1986.

[9]   Y. Martin, C. C. Williams, and H. K. Wickramasinghe, "Atomic force microscope–force mapping and profiling on a sub 100-Å scale", *Journal of Applied Physics,* vol. 61, pp. 4723-4729, 1987.

[10]   R. García Arrojo, *Amplitude Modulation Atomic Force Microscopy*. Wiley, 2010.

[11]   G. Meyer and N. M. Amer, "Novel optical approach to atomic force microscopy", *Applied Physics Letters,* vol. 53, pp. 1045-1047, 1988.

[12]   Y. L. Lyubchenko and L. S. Shlyakhtenko, "Visualization of supercoiled DNA with atomic force microscopy in situ", *Proceedings of the National Academy of Sciences,* vol. 94, pp. 496-501, 1997.

[13]   M. Fritz, M. Radmacher, J. P. Cleveland, M. W. Allersma, R. J. Stewart, R. Gieselmann*, et al.*, "Imaging Globular and Filamentous Proteins in Physiological Buffer Solutions with Tapping Mode Atomic Force Microscopy", *Langmuir,* vol. 11, pp. 3529-3535, 1995.

[14]   S. N. Magonov and D. H. Reneker, "Characterization of poymer surfaces with atomic force microscopy", *Annual Review of Materials Science,* vol. 27, pp. 175-222, 1997.

[15]   P. Leclère, R. Lazzaroni, J. L. Brédas, J. M. Yu, P. Dubois, and R. Jérôme, "Microdomain Morphology Analysis of Block Copolymers by Atomic Force Microscopy with Phase Detection Imaging", *Langmuir,* vol. 12, pp. 4317-4320, 1996.

[16]   K. Babcock and C. Prater, "Phase Imaging: Beyond Topography", *Digital Instruments, Inc.,* 1995.

[17]   D. A. Walters, J. P. Cleveland, N. H. Thomson, P. K. Hansma, M. A. Wendman, G. Gurley*, et al.*, "Short cantilevers for atomic force microscopy", *Review of Scientific Instruments,* vol. 67, pp. 3583-3590, 1996.

[18]   F. Pérez-Murano, G. Abadal, N. Barniol, X. Aymerich, J. Servat, P. Gorostiza*, et al.*, "Nanometer-scale oxidation of Si(100) surfaces by tapping mode atomic force microscopy", *Journal of Applied Physics,* vol. 78, pp. 6797-6801, 1995.

[19]   R. García, M. Calleja, and H. Rohrer, "Patterning of silicon surfaces with noncontact atomic force microscopy: Field-induced formation of nanometer-size water bridges", *Journal of Applied Physics,* vol. 86, pp. 1898-1903, 1999.

[20]   P. Samorì, *Scanning Probe Microscopies Beyond Imaging: Manipulation of Molecules and Nanostructures*. Wiley, 2006.

[21]   R. García and A. San Paulo, "Dynamics of a vibrating tip near or in intermittent contact with a surface", *Physical Review B,* vol. 61, pp. R13381-R13384, 2000.

[22]   T. R. Rodríguez and R. García, "Tip motion in amplitude modulation (tapping-mode) atomic-force microscopy: Comparison between continuous and point-mass models", *Applied Physics Letters,* vol. 80, pp. 1646-1648, 2002.

[23]   M. Stark, R. W. Stark, W. M. Heckl, and R. Guckenberger, "Inverting dynamic force microscopy: From signals to time-resolved interaction forces", *Proceedings of the National Academy of Sciences,* vol. 99, pp. 8473-8478, 2002.

[24]   T. Ando, N. Kodera, Y. Naito, T. Kinoshita, K. y. Furuta, and Y. Y. Toyoshima, "A High-speed Atomic Force Microscope for Studying Biological Macromolecules in Action", *ChemPhysChem,* vol. 4, pp. 1196-1202, 2003.

[25]   R. Proksch, "Multifrequency, repulsive-mode amplitude-modulated atomic force microscopy", *Applied Physics Letters,* vol. 89, p. 113121, 2006.

[26]   N. F. Martínez, J. R. Lozano, E. T. Herruzo, F. Garcia, C. Richter, T. Sulzbach*, et al.*, "Bimodal atomic force microscopy imaging of isolated antibodies in air and liquids", *Nanotechnology,* vol. 19, p. 384011, 2008.

[27]   O. Sahin, S. Magonov, C. su, C. Quate, and O. Solgaard, "An atomic Force Microscope Tip Designed to Measure Time-varying Nanomechanical Forces", *Nature Nanotechnology,* vol. 2, pp. 507-14, 2007.

[28]   S. Morita, F. J. Gießibl, and R. Wiesendanger, *Noncontact Atomic Force Microscopy: Volume 2*. Springer, 2009.

[29]   S. Basak and A. Raman, "Dynamics of tapping mode atomic force microscopy in liquids: Theory and experiments", *Applied Physics Letters,* vol. 91, p. 064107, 2007.

[30]   J. Lozano and R. Garcia, "Theory of Multifrequency Atomic Force Microscopy", *American Physical Society,* vol. 100, p. 076102, 2008.

[31]   P. Eaton and P. West, *Atomic Force Microscopy*. Oxford University Press, 2010.

[32]   M. W. Fairbairn, S. O. R. Moheimani, and A. J. Fleming, "Q Control of an Atomic Force Microscope Microcantilever: A Sensorless Approach", *Journal of Microelectromechanical Systems,* vol. 20, pp. 1372-1381, 2011.

[33]   H. C. Qiu, D. B. Xiao, D. Feili, X. Z. Wu, and H. Seidel, "Hydrodynamic analysis of piezoelectric microcantilevers vibrating in viscous compressible gases", *Sensors and Actuators A: Physical,* vol. 238, pp. 299-306, 2016.

[34]   T. R. Rodriguez and R. Garcia, "Theory of Q control in atomic force microscopy", *Applied Physics Letters,* vol. 82, pp. 4821-4823, 2003.

[35]   T. Sulchek, R. Hsieh, J. D. Adams, G. G. Yaralioglu, S. C. Minne, C. F. Quate*, et al.*, "High-speed tapping mode imaging with active Q control for atomic force microscopy", *Applied Physics Letters,* vol. 76, pp. 1473-1475, 2000.

[36]   K. M. Goeders, J. S. Colton, and L. A. Bottomley, "Microcantilevers: sensing chemical interactions via mechanical motion", *Chemical Reviews,* vol. 108, pp. 522-542, 2008.

[37]   P. West, *Atomic force microscopy*, 2006.

[38]   L. Chen, X. Yu, and D. Wang, "Cantilever dynamics and quality factor control in AC mode AFM height measurements", *Ultramicroscopy,* vol. 107, pp. 275-280, 2007.

[39]　M. W. Fairbairn, P. Muller, and S. O. R. Moheimani, "Sensorless Implementation of a PPF Controller for Active Q Control of an AFM Microcantilever", *IEEE Transactions on Control Systems Technology,* vol. 22, pp. 2118-2126, 2014.

[40]　M. B. Coskun, H. Alemansour, A. G. Fowler, M. Maroufi, and S. O. R. Moheimani, "Q Control of an Active AFM Cantilever With Differential Sensing Configuration", *IEEE Transactions on Control Systems Technology,* pp. 1-8, 2018.

[41]　M. Rakotondrabe, I. A. Ivan, S. Khadraoui, P. Lutz, and N. Chaillet, "Simultaneous Displacement/Force Self-Sensing in Piezoelectric Actuators and Applications to Robust Control", *IEEE/ASME Transactions on Mechatronics,* vol. 20, pp. 519-531, 2015.

[42]　J. Jahng, M. Lee, H. Noh, Y. Seo, and W. Jhe, "Active Q control in tuning-fork-based atomic force microscopy", *Applied Physics Letters,* vol. 91, p. 023103, 2007.

[43]　M. Kucera, T. Manzaneque, J. L. Sanchez-Rojas, A. Bittner, and U. Schmid, "Q-factor enhancement for self-actuated self-sensing piezoelectric MEMS resonators applying a lock-in driven feedback loop", *Journal of Micromechanics and Microengineering,* vol. 23, p. 085009, 2013.

[44]　T. Manzaneque, J. Hernando-García, A. Ababneh, P. Schwarz, H. Seidel, U. Schmid*, et al.*, "Quality-factor amplification in piezoelectric MEMS resonators applying an all-electrical feedback loop", *Journal of Micromechanics and Microengineering,* vol. 21, p. 025007, 2011.

[45]　A. U. Gerald, "Micro- and nanobiosensors—state of the art and trends", *Measurement Science and Technology,* vol. 20, p. 012001, 2009.

[46]　E. R. Dionne, V. Toader, and A. Badia, "Microcantilevers bend to the pressure of clustered redox centers", *Langmuir,* vol. 30, pp. 742-52, 2014.

[47]　S. Tadigadapa and K. Mateti, "Piezoelectric MEMS sensors: state-of-the-art and perspectives", *Measurement Science and Technology,* vol. 20, p. 092001, 2009.

[48]　Y. Kaiho, H. Takahashi, Y. Tomimatsu, T. Kobayashi, K. Matsumoto, I. Shimoyama*, et al.*, "An AlN cantilever for a wake-up switch triggered by air pressure change", *Journal of Physics: Conference Series,* vol. 476, p. 012122, 2013.

[49]　H. Campanella, C. J. Camargo, J. Esteve, and J. M. Tsai, "Sensitivity of thin-film bulk acoustic resonators (FBAR) to localized mechanical forces", *Journal of Micromechanics and Microengineering,* vol. 23, p. 065024, 2013.

[50]　M. Kucera, E. Wistrela, G. Pfusterschmied, V. Ruiz-Diez, T. Manzaneque, J. Hernando-Garcia*, et al.*, "Design-dependent performance of self-actuated and self-sensing piezoelectric-AlN cantilevers in liquid media oscillating in the fundamental in-plane bending mode", *Sensors and Actuators B: Chemical,* vol. 200, pp. 235-244, 2014.

[51]　G. Wang, L.-X. Xu, A. Ababneh, P. Schwarz, D. Feili, and H. Seidel, "AlN micromechanical radial-contour disc resonator", *Journal of Micromechanics and Microengineering,* vol. 23, p. 095002, 2013.

[52]　M. D. Williams, B. A. Griffin, T. N. Reagan, J. R. Underbrink, and M. Sheplak, "An AlN MEMS Piezoelectric Microphone for Aeroacoustic Applications", *Journal of Microelectromechanical Systems,* vol. 21, pp. 270-283, 2012.

[53]　S. Gunthner, M. Egretzberger, A. Kugi, K. Kapser, B. Hartmann, U. Schmid*, et al.*, "Compensation of parasitic effects for a silicon tuning fork gyroscope", *IEEE Sensors Journal,* vol. 6, pp. 596-604, 2006.

[54]　M. Clement, S. Gonzalez-Castilla, J. Olivares, J. Malo, J. I. Izpura, E. Iborra*, et al.*, "Frequency Characterization of AlN Piezoelectric Resonators", *2007 IEEE International Frequency Control Symposium Joint with the 21st European Frequency and Time Forum,* pp. 374-377, 2007.

[55] H. P. Loebl, C. Metzmacher, R. F. Milsom, P. Lok, F. van Straten, and A. Tuinhout, "RF Bulk Acoustic Wave Resonators and Filters", *Journal of Electroceramics,* vol. 12, pp. 109-118, 2004.

[56] O. Ambacher, "Growth and applications of Group III-nitrides", *Journal of Physics D: Applied Physics,* vol. 31, pp. 2653–2710, 1998.

[57] C. C. Chu, S. Dey, T. Y. Liu, C. C. Chen, and S. S. Li, "Thermal-Piezoresistive SOI-MEMS Oscillators Based on a Fully Differential Mechanically Coupled Resonator Array for Mass Sensing Applications", *Journal of Microelectromechanical Systems,* vol. 27, pp. 59-72, 2018.

[58] H. S. Wasisto, S. Merzsch, E. Uhde, A. Waag, and E. Peiner, "Handheld personal airborne nanoparticle detector based on microelectromechanical silicon resonant cantilever", *Microelectronic Engineering,* vol. 145, pp. 96-103, 2015.

[59] T. Michels and I. W. Rangelow, "Review of scanning probe micromachining and its applications within nanoscience", *Microelectronic Engineering,* vol. 126, pp. 191-203, 2014.

[60] K. Nakamura, *Ultrasonic Transducers: Materials And Design For Sensors, Actuators And Medical Applications*. Woodhead Publishing, 2012.

[61] R. van Schaijk, R. Elfrink, T. M. Kamel, and M. Goedbloed, "Piezoelectric AlN energy harvesters for wireless autonomous transducer solutions", *Sensors, 2008 IEEE,* pp. 45-48, 2008.

[62] R. Elfrink, T. M. Kamel, M. Goedbloed, S. Matova, D. Hohlfeld, Y. van Andel*, et al.*, "Vibration energy harvesting with aluminum nitride-based piezoelectric devices", *Journal of Micromechanics and Microengineering,* vol. 19, p. 094005, 2009.

[63] A. Ababneh, U. Schmid, J. Hernando, J. L. Sánchez-Rojas, and H. Seidel, "The influence of sputter deposition parameters on piezoelectric and mechanical properties of AlN thin films", *Materials Science and Engineering: B,* vol. 172, pp. 253-258, 2010.

[64] A. Artieda, C. Sandu, and P. Muralt, "Highly piezoelectric AlN thin films grown on amorphous, insulating substrates", *Journal of Vacuum Science & Technology A,* vol. 28, pp. 390-393, 2010.

[65] A. Pérez-Campos, G. F. Iriarte, J. Hernando-Garcia, and F. Calle, "Post-CMOS compatible high-throughput fabrication of AlN-based piezoelectric microcantilevers", *Journal of Micromechanics and Microengineering,* vol. 25, p. 025003, 2015.

[66] M. Gillinger, M. Schneider, A. Bittner, P. Nicolay, and U. Schmid, "Impact of annealing temperature on the mechanical and electrical properties of sputtered aluminum nitride thin films", *Journal of Applied Physics,* vol. 117, p. 065303, 2015.

[67] G. Pfusterschmied, M. Kucera, W. Steindl, T. Manzaneque, V. Ruiz Díez, A. Bittner*, et al.*, "Roof tile-shaped modes in quasi free–free supported piezoelectric microplate resonators in high viscous fluids", *Sensors and Actuators B: Chemical,* vol. 237, pp. 999-1006, 2016.

[68] M. Kucera, F. Hofbauer, E. Wistrela, T. Manzaneque, V. Ruiz-Díez, J. L. Sánchez-Rojas*, et al.*, "Lock-in amplifier powered analogue Q-control circuit for self-actuated self-sensing piezoelectric MEMS resonators", *Microsystem Technologies,* vol. 20, pp. 615-625, 2014.

[69] S. Hemon, A. Akjouj, A. Soltani, Y. Pennec, Y. El Hassouani, A. Talbi*, et al.*, "Hypersonic band gap in an AlN-TiN bilayer phononic crystal slab", *Applied Physics Letters,* vol. 104, p. 063101, 2014.

[70] D. Chen, J. Wang, D. Li, L. Zhang, and X. Wang, "The c-axis oriented AlN solidly mounted resonator operated in thickness shear mode using lateral electric field excitation", *Applied Physics A,* vol. 100, pp. 239-244, 2010.

[71] S. T. S. Holmström, U. Baran, and H. Urey, "MEMS Laser Scanners: A Review", *Journal of Microelectromechanical Systems,* vol. 23, pp. 259-275, 2014.

[72] web: (2023.03.25). "*Low Noise Bottom Port Analog Single-Ended Piezoelectric MEMS Microphone, VM1000, R0.0.1*". Available: https://vespermems.com/products/vm1000/.

[73] S. R. Anton and H. A. Sodano, "A review of power harvesting using piezoelectric materials (2003–2006)", *Smart Materials and Structures,* vol. 16, pp. R1-R21, 2007.

[74] P. M. Mayrhofer, C. Rehlendt, M. Fischeneder, M. Kucera, E. Wistrela, A. Bittner*, et al.*, "ScAlN MEMS Cantilevers for Vibrational Energy Harvesting Purposes", *Journal of Microelectromechanical Systems,* vol. 26, pp. 102-112, 2017.

[75] J. D. Adams, L. Manning, B. Rogers, M. Jones, and S. C. Minne, "Self-sensing tapping mode atomic force microscopy", *Sensors and Actuators A: Physical,* vol. 121, pp. 262-266, 2005.

[76] J. D. Adams, A. Nievergelt, B. W. Erickson, C. Yang, M. Dukic, and G. E. Fantner, "High-speed imaging upgrade for a standard sample scanning atomic force microscope using small cantilevers", *Review of Scientific Instruments,* vol. 85, p. 093702, 2014.

[77] M. Mahdavi, N. Nikooienejad, and S. O. R. Moheimani, "AFM Microcantilever With a Collocated AlN Sensor-Actuator Pair: Enabling Efficient Q-Control for Dynamic Imaging", *Journal of Microelectromechanical Systems,* vol. 29, pp. 661-668, 2020.

[78] M. Mahdavi, M. B. Coskun, and S. O. R. Moheimani, "High Dynamic Range AFM Cantilever With a Collocated Piezoelectric Actuator-Sensor Pair", *Journal of Microelectromechanical Systems,* vol. 29, pp. 260-267, 2020.

[79] M. B. Coskun, A. G. Fowler, M. Maroufi, and S. O. R. Moheimani, "On-Chip Feedthrough Cancellation Methods for Microfabricated AFM Cantilevers With Integrated Piezoelectric Transducers", *Journal of Microelectromechanical Systems,* vol. 26, pp. 1287-1297, 2017.

[80] M. G. Ruppert, A. G. Fowler, M. Maroufi, and S. O. R. Moheimani, "On-Chip Dynamic Mode Atomic Force Microscopy: A Silicon-on-Insulator MEMS Approach", *Journal of Microelectromechanical Systems,* vol. 26, pp. 215-225, 2017.

[81] M. G. Ruppert and Y. K. Yong, "Note: Guaranteed collocated multimode control of an atomic force microscope cantilever using on-chip piezoelectric actuation and sensing", *Review of Scientific Instruments,* vol. 88, p. 086109, 2017.

[82] K. Lau, D. E. Quevedo, B. J. G. Vautier, G. C. Goodwin, and S. O. R. Moheimani, "Design of modulated and demodulated controllers for flexible structures", *Control Engineering Practice,* vol. 15, pp. 377-388, 2007.

[83] K. S. Karvinen and S. O. R. Moheimani, "Modulated–demodulated control: Q control of an AFM microcantilever", *Mechatronics,* vol. 24, pp. 661-671, 2014.

[84] N. Sinha, G. E. Wabiszewski, R. Mahameed, V. V. Felmetsger, S. M. Tanner, R. W. Carpick*, et al.*, "Ultra thin AlN piezoelectric nano-actuators", *TRANSDUCERS 2009 - 2009 International Solid-State Sensors, Actuators and Microsystems Conference,* pp. 469-472, 2009.

[85] N. Heidrich, D. Iankov, J. Hees, W. Pletschen, R. E. Sah, L. Kirste*, et al.*, "Enhanced mechanical performance of AlN/nanodiamond micro-resonators", *Journal of Micromechanics and Microengineering,* vol. 23, p. 125017, 2013.

[86] H. Huan, C. Hanna, S. Suhas, F. V. Alexander, and P. K. William, "Silicon nano-mechanical resonators fabricated by using tip-based nanofabrication", *Nanotechnology,* vol. 25, p. 275301, 2014.

[87] S. Barth, H. Bartzsch, D. Gloess, P. Frach, T. Herzog, S. Walter*, et al.*, "Sputter deposition of stress-controlled piezoelectric AlN and AlScN films for ultrasonic and energy harvesting applications", *IEEE Transactions on Ultrasonics, Ferroelectrics, and Frequency Control,* vol. 61, pp. 1329-1334, 2014.

[88] J. Valasek, "Piezo-Electric and Allied Phenomena in Rochelle Salt", *Physical Review,* vol. 17, pp. 475-481, 1921.

[89] J. Tichy, J. Erhart, E. Kittinger, and J. Prívratská, *Fundamentals of Piezoelectric Sensorics: Mechanical, Dielectric, and Thermodynamical Properties of Piezoelectric Materials*. Springer, 2010.

[90] C. R. Bowen, H. A. Kim, P. M. Weaver, and S. Dunn, "Piezoelectric and ferroelectric materials and structures for energy harvesting applications", *Energy & Environmental Science,* vol. 7, pp. 25-44, 2014.

[91] S. Li, Z. Zhao, J. Zhao, Z. Zhang, X. Li, and J. Zhang, "Recent Advances of Ferro-, Piezo-, and Pyroelectric Nanomaterials for Catalytic Applications", *ACS Applied Nano Materials,* vol. 3, pp. 1063-1079, 2020.

[92] S. Baoyuan, W. Jiantong, Z. Jun, and Q. Min, "A new model describing physical effects in crystals: the diagrammatic and analytic methods for macro-phenomenological theory", *Journal of Materials Processing Technology,* vol. 139, pp. 444-447, 2003.

[93] J. Erhart, P. Půlpán, and M. Pustka, *Piezoelectric Ceramic Resonators*. Springer, 2017.

[94] S. Rupitsch, *Piezoelectric Sensors and Actuators: Fundamentals and Applications*. Springer, 2019.

[95] G. Fasching, *Werkstoffe für die Elektrotechnik: Mikrophysik, Struktur, Eigenschaften*. Springer, 2005.

[96] S. Iyer, M. Alkhader, and T. A. Venkatesh, "On the relationships between cellular structure, deformation modes and electromechanical properties of piezoelectric cellular solids", *International Journal of Solids and Structures,* vol. 80, pp. 73-83, 2016.

[97] "Standards on Piezoelectric Crystals", *Proceedings of the IRE,* vol. 37, pp. 1378-1395, 1949.

[98] W. Heywang, *Piezoelectricity: Evolution and Future of a Technology*. Springer, 2008.

[99] IEEE, IEEE Standard on Piezoelectricity, ANSI/IEEE Std 176-1987, 1988.

[100] T. Ikeda, *Fundamentals of Piezoelectricity*. Oxford University Press, 1990.

[101] J. Piprek, *Nitride Semiconductor Devices: Principles and Simulation*. Wiley, 2007.

[102] P. Muralt, "Piezoelectric thin films for MEMS", *Integrated Ferroelectrics,* vol. 17, pp. 297-307, 1997.

[103] M. J. Madou, *Fundamentals of Microfabrication: The Science of Miniaturization*. CRC Press, 2002.

[104] A. Boisen, S. Dohn, S. S. Keller, S. Schmid, and M. Tenje, "Cantilever-like micromechanical sensors", *Reports on Progress in Physics,* vol. 74, p. 036101, 2011.

[105] B. Ilic, D. Czaplewski, M. Zalalutdinov, H. G. Craighead, P. Neuzil, C. Campagnolo*, et al.*, "Single cell detection with micromechanical oscillators", *Journal of Vacuum Science & Technology B: Microelectronics and Nanometer Structures Processing, Measurement, and Phenomena,* vol. 19, pp. 2825-2828, 2001.

[106] J. W. Ndieyira, M. Watari, A. D. Barrera, D. Zhou, M. Vögtli, M. Batchelor*, et al.*, "Nanomechanical detection of antibiotic–mucopeptide binding in a model for superbug drug resistance", *Nature Nanotechnology,* vol. 3, pp. 691-696, 2008.

[107] M.-A. Dubois and P. Muralt, "Properties of aluminum nitride thin films for piezoelectric transducers and microwave filter applications", *Applied Physics Letters,* vol. 74, pp. 3032-3034, 1999.

[108] M. N. Yoder, "Wide bandgap semiconductor materials and devices", *IEEE Transactions on Electron Devices,* vol. 43, pp. 1633-1636, 1996.

[109] Z. Tsybrii, F. Sizov, M. Vuichyk, I. Korotash, and E. Rudenko, "AlN and MgO thin-layer coatings on the bendable polymeric substrates as selective filters for IR and THz spectral ranges", *Infrared Physics & Technology,* vol. 107, p. 103323, 2020.

[110] M. Schneider, T. Strunz, A. Bittner, and U. Schmid, "Impact of Sputter Deposition Parameters on the Leakage Current Behavior of Aluminum Nitride Thin Films", *Advances in Science and Technology,* vol. 77, pp. 29-34, 2012.

[111] web: (2017.10.02). "*Crystal structure of ZnS (wurtzite) with coordination polyhedra*" [Image]. Available: https://commons.wikimedia.org/wiki/File:Wurtzite_polyhedra.png.

[112] P. M. Mayrhofer, E. Wistrela, M. Schneider, A. Bittner, and U. Schmid, "Precise Determination of d33 and d31 from Piezoelectric Deflection Measurements and 2D FEM Simulations Applied to ScxAl1-xN", *Procedia Engineering,* vol. 168, pp. 876-879, 2016.

[113] J. García, J. L. Sanchez-Rojas, A. Ababneh, U. Schmid, S. González, and E. Iborra, "Piezoelectric characterization of ain thin films on silicon substrates", *XXII Eurosensors 2008,* 2008.

[114] S. Kasap, *Springer Handbook of Electronic and Photonic Materials*. Springer, 2006.

[115] K. Seshan, *Handbook of Thin Film Deposition*. William Andrew, 2012.

[116] K. Wasa, *Handbook of Sputter Deposition Technology: Fundamentals and Applications for Functional Thin Films, Nano-Materials and MEMS*. William Andrew, 2012.

[117] U. Figueroa, O. Salas, and J. Oseguera, "Production of AlN films: ion nitriding versus PVD coating", *Thin Solid Films,* vol. 469-470, pp. 295-303, 2004.

[118] M. Schneider, A. Bittner, A. Klein, and U. Schmid, "Impact of film thickness and temperature on the dielectric breakdown behavior of sputtered aluminum nitride thin films", *Microelectronic Engineering,* vol. 140, pp. 47-51, 2015.

[119] M. Schneider, A. Bittner, P. Schmid, and U. Schmid, "Impact of C-axis Orientation of Aluminium Nitride Thin Films on the Long-term Stability and Mechanical Properties of Resonantly Excited MEMS Cantilevers", *Procedia Engineering,* vol. 87, pp. 1493-1496, 2014.

[120] M. Schneider, A. Bittner, F. Patocka, M. Stöger-Pollach, E. Halwax, and U. Schmid, "Impact of the surface-near silicon substrate properties on the microstructure of sputter-deposited AlN thin films", *Applied Physics Letters,* vol. 101, p. 221602, 2012.

[121] diss: M. Kucera, "Performance of cantilever-based piezoelectric MEMS resonators in liquid environment", Performance of cantilever-based piezoelectric MEMS resonators in liquid environment, Wien, Techn. Univ., 2014.

[122] diss: M. Schneider, "Einfluss der Schichtdicke und der Substratvorbehandlung auf die elektro-mechanischen Eigenschaften von gesputterten Aluminiumnitrid-Dünnfilmen", Influence of film thickness and substrate pre-treatment on the electro-mechanical properties of sputtered aluminum nitride thin films, Wien, Techn. Univ, 2014.

[123] S. Franssila, *Introduction to Microfabrication*. Wiley, 2010.

[124] M. Kucera, T. Manzaneque, J. L. Sanchez-Rojas, A. Bittner, and U. Schmid, "Lock-in driven quality factor enhancement with parasitic effect compensation of a self-actuated piezoelectric MEMS cantilever", *IEEE International Ultrasonics Symposium,* pp. 2195-2198, 2012.

[125] "Dimension Edge with ScanAsyst", *Bruker Nano Surfaces Division,* 2013.

[126] "NCHV-A Cantilever", *Bruker Nano Surfaces Division,* 2020.

[127]   D. K. Schroder, *Semiconductor Material and Device Characterization*. Wiley, 2006.

[128]   "SU8000 Series Ultra-high Resolution Scanning Electron Microscope", *Hitachi High-Technologies Corporation,* 2011.

[129]   O. H. Seeck and B. Murphy, *X-Ray Diffraction: Modern Experimental Techniques*. Pan Stanford, 2015.

[130]   "Pyrospot DGE 10N/DGE 10NV", *DIAS Infrared Systems GmbH,* 2018.

[131]   M. Schneider, A. Bittner, and U. Schmid, "Temperature dependant dielectric breakdown of sputter-deposited AlN thin films using a time-zero approach", *Microsystem Technologies,* vol. 20, pp. 751-757, 2013.

[132]   S. M. Sze and K. N. Kwok, *Physics of semiconductor devices*. Wiley, 2006.

[133]   F. Engelmark, J. Westlinder, G. F. Iriarte, I. V. Katardjiev, and J. Olsson, "Electrical characterization of AlN MIS and MIM structures", *IEEE Transactions on Electron Devices,* vol. 50, pp. 1214-1219, 2003.

[134]   N. Ben Hassine, D. Mercier, P. Renaux, G. Parat, S. Basrour, P. Waltz*, et al.*, "Dielectrical properties of metal-insulator-metal aluminum nitride structures: Measurement and modeling", *Journal of Applied Physics,* vol. 105, p. 044111, 2009.

[135]   M. Stewart and M. G. Cain, *Direct Piezoelectric Measurement: The Berlincourt Method*. Springer, 2014.

[136]   A. Ababneh, H. Kreher, and U. Schmid, "Etching behaviour of sputter-deposited aluminium nitride thin films in H3PO4 and KOH solutions", *Microsystem Technologies,* vol. 14, pp. 567-573, 2008.

[137]   E. Wistrela, M. Schneider, A. Bittner, and U. Schmid, "Impact of the substrate dependent polarity distribution in c-axis oriented AlN thin films on the etching behaviour and the piezoelectric properties", *Microsystem Technologies,* vol. 22, pp. 1691-1700, 2015.

[138]   H. Lutz, *Taschenbuch der Regelungstechnik*. Verlag Europa-Lehrmittel, 2002.

[139]   V. Plenk, *Grundlagen der Automatisierungstechnik kompakt*. Springer, 2019.

[140]   M. Kucera, F. Hofbauer, T. Manzaneque, V. Ruiz, J. L. Sánchez-Rojas, A. Bittner*, et al.*, "Quality factor enhancement for resonant MEMS applying an analogue feedback circuit driven by a lock-in amplifier", *SPIE Proceedings,* vol. 8763, pp. 87630W-1, 2013.

[141]   K. Naeli and O. Brand, "Dimensional considerations in achieving large quality factors for resonant silicon cantilevers in air", *Journal of Applied Physics,* vol. 105, p. 014908, 2009.

[142]   J. A. Judge, D. M. Photiadis, J. F. Vignola, B. H. Houston, and J. Jarzynski, "Attachment loss of micromechanical and nanomechanical resonators in the limits of thick and thin support structures", *Journal of Applied Physics,* vol. 101, p. 013521, 2007.

[143]   Z. Hao, A. Erbil, and F. Ayazi, "An analytical model for support loss in micromachined beam resonators with in-plane flexural vibrations", *Sensors and Actuators A: Physical,* vol. 109, pp. 156-164, 2003.

[144]   M. Fischeneder, A. Bittner, M. Schneider, and U. Schmid, "Enhanced process stability for the low temperature sputter deposition of aluminium nitride thin films", *Materials Research Express,* vol. 5, p. 066412, 2018.

[145]   M. Fischeneder, E. Wistrela, A. Bittner, M. Schneider, and U. Schmid, "Tailored wafer holder for a reliable deposition of sputtered aluminium nitride thin films at low temperatures", *Materials Science in Semiconductor Processing,* vol. 71, pp. 283-289, 2017.

[146]   A. Smithells and W. F. Gale, *Smithells Metals Reference Book*. Elsevier, 2004.

[147] W. M. Yim and R. J. Paff, "Thermal expansion of AlN, sapphire, and silicon", *Journal of Applied Physics,* vol. 45, pp. 1456-1457, 1974.

[148] H. Mehner, S. Leopold, and M. Hoffmann, "Variation of the intrinsic stress gradient in thin aluminum nitride films", *Journal of Micromechanics and Microengineering,* vol. 23, p. 095030, 2013.

[149] F. Martin, P. Muralt, M.-A. Dubois, and A. Pezous, "Thickness dependence of the properties of highly c-axis textured AlN thin films", *Journal of Vacuum Science & Technology A,* vol. 22, pp. 361-365, 2004.

[150] F. Medjani, R. Sanjinés, G. Allidi, and A. Karimi, "Effect of substrate temperature and bias voltage on the crystallite orientation in RF magnetron sputtered AlN thin films", *Thin Solid Films,* vol. 515, pp. 260-265, 2006.

[151] J. P. Kar, G. Bose, and S. Tuli, "Correlation of electrical and morphological properties of sputtered aluminum nitride films with deposition temperature", *Current Applied Physics,* vol. 6, pp. 873-876, 2006.

[152] M. Schneider, A. Bittner, and U. Schmid, "Impact of film thickness on the temperature-activated leakage current behavior of sputtered aluminum nitride thin films", *Sensors and Actuators A: Physical,* vol. 224, pp. 177-184, 2015.

[153] A. Ababneh, A. N. Al-Omari, A. M. K. Dagamseh, H. C. Qiu, D. Feili, V. Ruiz-Díez*, et al.*, "Electrical characterization of micromachined AlN resonators at various back pressures", *Microsystem Technologies,* vol. 20, pp. 663-670, 2014.

[154] M. Fischeneder, M. Oposich, M. Schneider, and U. Schmid, "Tuneable Q-Factor of MEMS Cantilevers with Integrated Piezoelectric Thin Films", *Proceedings,* vol. 1, p. 380, 2017.